A Wideband
Aperture Coupled Microstrip Array
for an
Automotive Radar Sensor

by

Duane N. Mateychuk

A thesis
presented to the
University of Manitoba
in partial fulfillment of the
requirements for the degree of
Master of Science
in
Electrical Engineering

Winnipeg, Manitoba, 1997

THE UNIVERSITY OF MANITOBA

FACULTY OF GRADUATE STUDIES

*****

COPYRIGHT PERMISSION PAGE

A WIDEBAND APERTURE COUPLED MICROSTRIP ARRAY FOR AN AUTOMOTIVE RADAR SENSOR

BY

DUANE N. MATEYCHUK

A Thesis/Practicum submitted to the Faculty of Graduate Studies of The University of Manitoba in partial fulfillment of the requirements of the degree of MASTER OF SCIENCE

Abstract

The development of automotive radar sensors is a hotly contested area of research that has tremendous sales volume potential for the manufacturers able to meet the low pricing guidelines set for these products. Traditional PTFE laminate materials have excellent electrical properties of low dielectric loss tangents, but the material and fabricating costs for these circuits are relatively expensive, and were not deemed acceptable for a viable automotive radar program. The recent introduction of inexpensive, commercial grade laminates is extremely attractive for these applications.

In this thesis the design of a commercial grade laminate, aperture fed microstrip patch antenna, with coplanar parasitic elements, is pursued. This antenna element will then be used in the design and development of an experimental prototype microstrip array for use in an automotive back-up-aid radar sensor.

The numerical analysis tools required for quick, efficient, and moderately accurate design of this microstrip antenna configuration were not available at the time and it was the intention of this research to create such a tool. During this research, a number of commercial analysis tools became available which were more than adequate for the current research. Two commercial method-of-moment analysis software packages were acquired.

Using the knowledge gained from the theoretical and numerical analysis of this antenna element, a prototype antenna was designed, fabricated, tested, and analyzed with respect to relevant performance criteria. A 16-element array using this new antenna element is then developed from concept to a complete analysis of the performance obtained from a fabricated antenna array.

In this thesis it is demonstrated that with the proper design, of microstrip circuits produced on commercial grade laminates, satisfactory performance at microwave

frequencies is achievable. The results obtained here are expected to lead to the design of other products on these inexpensive laminates.

Acknowledgements

I would like to thank Dr. L. Shafai for his support, patience, advice, and guidance. His patience is greatly appreciated as my professional career has prolonged the completion of this research.

I would like to thank the Communications Research Centre (CRC) in Ottawa where much was learned from the antennas and integrated electronics group which consisted of Apisak Ittipiboon, Dave Roscoe, Neil Simons, and Aldo Petosa. I would also like to thank Rene Douville and Michel Cuhaci at CRC for allowing me the opportunity to perform some experimental research at their facilities.

I would like to also thank my current employer HE Microwave who supported this research, and the BUA Team who has been patient with me while I completed the writing of this thesis document.

I would especially like to thank my wife Coleen who has provided motivation and emotional support for this research when things were moving rather slowly. I appreciate her understanding at the many late hours in the lab and computer allowing me to put closure on this research.

Table of Contents

List of Figures

List of Tables

CHAPTER 1: Introduction

1.1 Modern Microwave Engineering

1.1.1 General

Prior to the 1940's and World War II microwave systems were usually combinations of waveguide and coaxial transmission lines. In this era of microwave engineering waveguide circuits usually dominated most of these system designs as complex microwave circuits were not easily achieved using coax. Due to the heavy reliance on waveguide as the transmission media, these microwave systems were generally extremely large, heavy, very expensive and quite difficult to build. Since WW II microwave technology has matured to the point that it is now feasible to create microwave integrated circuits (MIC's) that are smaller, lighter in weight, faster, cheaper to fabricate and quite a bit more complex than their ancestors. Following the lead in the digital IC world, there has been a push for higher frequency applications using even smaller and faster circuits.

1.1.2 Higher Operating Frequencies

Microwave systems have been developed for many years for use in, communications, radar, navigation, surveillance, and weapons guidance systems. These systems are largely military in nature and are strongly supported by the defence community. The current spectrum of frequencies upto the lower millimeter region has been allocated for specific usage. Due to the congestion within these allocated bands microwave engineers have been forced to resort to frequency reuse or design systems that operate at higher less congested or unallocated frequency bands.

Operation of microwave systems at higher frequencies is an attractive area of research currently being pursued by many in the microwave field. Higher operating fre-

quencies correspond to shorter electrical wavelengths which leads to components substantially smaller in physical size. Component size reduction is extremely important as research programs strive to meet goals for system weight reduction which is critical when designing many mobile earth, aircraft or space borne terminals. A major concern is that the propagating signal attenuation increases substantially at higher frequencies [52] which needs to be offset by higher transmit power levels to achieve the same signal to noise ratio and maintain signal clarity.

Table 1.1: Microwave Frequency Bands

US Military Band Designation	Frequency Band
L	1-2 GHz
S	2-4 GHz
C	4-8 GHz
X	8-12 GHz
Ku	12-18 GHz
K	18-27 GHz
Ka	27-40 GHz
V	40-75
W	75-110

1.1.3 Microstrip Circuits

Microstrip concepts were first proposed in the 1950's [33,41] but their use did not gain momentum until the late 1960's and 1970's, mainly due to the lack of suitable low loss, dielectric substrates. Microstrip circuits consist of a single substrate with a ground plane on its bottom surface and a narrow strip of conducting transmission line on its top surface. Microstrip is basically printed circuits for microwaves and is usually fabri-

cated like printed circuit boards, but requires higher-resolution photolithographic processes because of the dimensional accuracy required. Circuits using microstrip have been economically implemented in many low-to-medium power systems including radar, electronic counter-measures, communication links, and in portions of satellite communication systems. Microstrip transmission lines are widely used in Miniature Hybrid MIC's (MHMIC's).

Microstrip limitations are few, the fundamental one being low power handling capability which may be overcome with the realization of good matching circuitry. There are four separate mechanisms that can be identified for the power losses and parasitic effects associated with microstrip lines; conductor losses, dissipation in the dielectric substrate, radiation losses, and surface wave propagation. Conductor and dielectric losses are lumped together and calculated as part of an attenuation coefficient for the line. Discontinuities such as abrupt open-circuit lines, steps, and bends will radiate to a certain extent and efforts must be made to reduce radiation and its undesirable side effects in circuits such as filters and amplifiers. Most of the propagating electromagnetic wave is confined to the region between the ground plane and the strip conductor but surface waves do account for some of the lost transmission power. Surface waves are waves trapped just beneath the surface of the dielectric substrate and propagate away from discontinuities in the form of higher order TM and TE radial modes.

1.1.4 Microwave Integrated Circuits

In the microwave community the idea evolved that all microwave functions of analog and digital applications could be incorporated on a single chip. Based on advances made in printed circuit board technology, and the development of electronic integrated circuits (IC's) which became very popular in the 1970's, the development of IC's has matured to such a level that many inexpensive products now use these IC chips in

a substantial portion of their circuitry. Only recently has extensive work been directed towards the development of Microwave Integrated Circuits (MIC's).

The goal of recent years has been to develop MIC's that incorporate phased antenna arrays with transmitters, receivers and the complete array feed network all within the MIC. A MIC is in general a combination of active and passive circuit elements that are manufactured by successive diffusion processes on a semiconductor substrate. Monolithic MIC's (MMICs) have all active and passive components created on the same substrate. Miniature Hybrid MIC's (MHMIC's) have passive transmission lines fabricated on a substrate and discrete components such as resistors, capacitors, inductors, transistors, or diodes attached to the substrate and electrically connected with bond wires or by solder reflow. The advantage of MMIC's over MHMIC's is the fact that there are no parasitic effects due to the bond wires or solder joints connecting the discrete component electrically into the circuit which may be a problem at millimetre wave frequencies.

Current monolithic circuit technology has low yield rates, and currently produces circuits that have relatively poor performance, therefore MMIC use has been limited. Continued development of MMIC process technology will eventually lead to lower costs, higher yields and better performance, reproducibility and reliability. The emergence of Gallium Arsenide (GaAs) as the technology of choice for the development of MMIC's has been related to this semi-insulating substrates' almost ideal dielectric properties for microstrip transmission lines, and the development of the GaAs Field-Effect-Transistor (FET).

Miniature Hybrid MIC's are a more cost effective means to realize circuits with higher yield rates making it the preferred technology for most applications. In many applications in the 1 to 18 GHz frequency range, MHMIC's are used almost exclusively. These circuits are fabricated on high quality ceramic, glass or ferrite substrates, although standard microwave laminate materials have seen increased use. Passive circuit elements are deposited on the substrate and active devices are mounted on the substrate and con-

nected to the passive circuit. Active devices may be utilized in chip form, on chip carriers, or in small plastic packages.

1.2 Microstrip Antennas

1.2.1 General

Microstrip antennas technology originated from the idea of utilizing the undesirable radiation noted in microstrip circuits in a positive way as an antenna element which is created as part of the microstrip circuitry. These antennas are low profile due to their planar configuration and are easily made conformal and have been used on aircraft, missiles [40], and satellites. In military application where radar detection is of concern this antenna possesses a low scattering radar cross section to minimize detection.

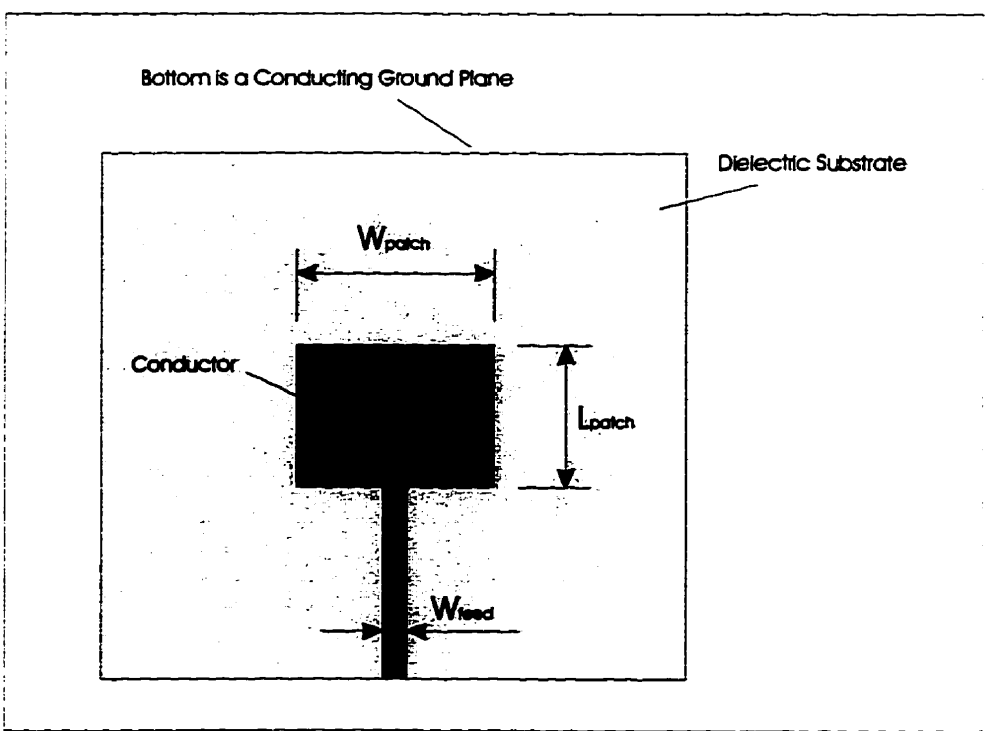

Figure 1.1 Traditional microstrip fed patch antenna

1.2.2 Feed Techniques

The design of microstrip antennas is closely related to the feeding techniques to be employed. There are some problems encountered with classical feed methods such as microstrip line or probe feeds. The performance of microstrip feed antennas is degraded by the size of the feed which may be comparable to patch itself. When faced with size constraints microstrip feedline array applications leave little room for the feed network and circuitry on the same substrate. Probe fed antennas do not face size constraint difficulties but have questionable solder joint repeatability. Proximity coupling suffers from the same feed radiation and space usage problems as microstrip feed antennas.

Aperture coupling is a multilayer feed mechanism that isolates the radiation from the antenna elements from the feed circuitry radiation. An aperture located in a ground plane common to two dielectric laminates is used to couple energy from one layer, through the aperture, to the other layer. This is the feed mechanism pursued in all radiating element designs in this thesis.

1.2.3 Aperture Feeds

Aperture fed microstrip antennas was first proposed by Pozar [1] as a means of feeding without a direct connection required. As briefly mentioned above, aperture feeding allows the use of different substrates for the radiating patch and active circuitry. The substrates can be chosen to be the materials most desirable for optimum patch radiation and minimum feed network radiation. Separate layers for the feed and radiators also doubles the available surface area and allows for easy integration of active or passive microwave circuit blocks within the feed network. The ground plane separates the radiating patch from the feed circuitry thus eliminating most extraneous feed radiation that degrades the broadside radiation pattern. Minimal back radiation occurs as small non-resonant apertures are usually utilized.

Previous experimental work [1,4,15,16,23,36] has shown that the aperture feed efficiently and effectively excites the radiator with a good radiation pattern realized. The bandwidth of the overall structure was stated to be essentially that of the element and is not appreciably effected by the feed coupling mechanism [28]. An area of concern is that the fabrication requires the aperture to be properly aligned with the radiating element above and the feedline below, with misalignment affecting the coupling level. The degree of coupling is implied by the size of the impedance loop on a Smith chart [32], which becomes more coupled when the coupling loop increases in size. The size of the loop is of primary concern when the bandwidth characteristic of the antenna is critical [36]. It is known from experimental results that as the ratio of the radiating patch width to the slot length is increased the coupling to the patch is decreased. The slot length affects the resonant frequency as much as a variation of patch dimension would. For a specific coupling level the length of the slot and its associated back radiation can be reduced by reducing the thickness of the bottom substrate. When the patches are loosely coupled they are more sensitive to fabrication tolerances.

1.2.4 Performance Enhancements

Microstrip antennas have some critical shortcomings, of major concern is that a single patch has a relatively narrow bandwidth of approximately 1-5%, which is too narrow for many applications. When using microstrip antennas in a MIC or MMIC design the restriction on operating bandwidth is usually due to the antenna as most circuits are able to operate over substantially wider bandwidths. The narrow bandwidth inherent to this antenna is due to the fact that the region under the patch is basically a high Q, resonant cavity. As microstrip patch antennas are strongly resonant devices, the variation of impedance rather than radiation pattern degradation determines the bandwidth. There are numerous ways to increase antenna bandwidth [17,38,39] such as employing thicker substrates,

stacking several substrates, or adding electromagnetically coupled parasitic elements. The bandwidth may also be increased by introducing multiple resonance in the input impedance characteristics.

As mentioned previously when microstrip feedlines are used there is poor radiation isolation between the feed and radiating elements. Theoretical and experimental results [14,26,54] show that at high frequencies feedline radiation may be substantially larger than the conductor and dielectric losses and corrupt the patch radiation pattern significantly. This feedline radiation causes lower antenna gains to be obtained. To maximize patch radiation these microstrip antennas require a thick, low permittivity substrate and to minimize feed losses, a high permittivity, thin substrate is required.

The element design pursued here uses parasitic loading of a main radiator with an aperture feed. The desired antenna should have a relatively wide bandwidth with a clean radiation pattern.

1.2.5 Microstrip Arrays

Single element microstrip antennas typically have low gain, low radiation efficiency, and wider than desired beamwidthes [37]. Most applications require higher antenna performance and must resort to an array of elements.

Microstrip array designs are based on element type, feed methods, and substrate configurations to be employed. In applications where antenna movement, multipath, or changing environments degrade antenna performance, adaptive microstrip beam steering arrays may be used. In large arrays, using a large number of array elements, feed losses may be excessive. There exists a practical limitation on array gain of approximately 20dB [41]. The goal of antenna array design is to find the easiest way to create multi-element units which meet or exceed design specifications with the minimum fabrication labour.

The design of high resolution phased arrays with active beam scanning circuitry is possible. These phased arrays are capable of rapid and continuous electrical scanning of beams while remaining mechanically stable. Both fixed and scanned beams may simultaneously be generated as multifunction operation is possible. A particular aperture distribution may more readily be obtained with an array than with either a lens or by using reflectors since the amplitude and phase of each element can be individually controlled. These arrays may exhibit a slow degradation of performance rather than a catastrophic failure with careful design and array component redundancy. Arrays may be modified simply by adding extra elements, replacing passive elements with active elements, etc. When narrow beamwidthes with a large number of elements are required, the cost and complexity of the antenna increases substantially. In these large arrays, failure of a small portion of the array elements, or their feed circuitry, may cause a significant degradation in the antenna performance.

1.3 Thesis Objective

The objective of this thesis research is to theoretically, and experimentally, investigate the potential use of commercial grade microwave laminates, for the development of an array of aperture fed, microstrip patch antennas with coplanar parasitic elements, for use in an automobile back-up-aid radar sensor.

1.4 Multi-Layer Microstrip Antenna Configuration Considerations

1.4.1 Antenna Geometry and Specifications

The antenna design investigated in this research is based on an antenna proposed by Schaubert and Farrar [5]. This design was able to increase the microstrip patch impedance bandwidth by creating a double tuned resonance, with the addition of parasitic resonators on the same surface as the primary patch radiator. These conductor strips are electromagnetically coupled to the non-radiating edges of the main patch. The design proposed here uses a similar patch and strip configuration, but it uses an aperture feed. Once the performance of an element is verified, an array of these elements will be created. The resulting antenna is to be used for an automotive collision avoidance product with the potential for production of several million units annually. The anticipated volume for this product requires a design that puts substantial emphasis on manufacturability without sacrificing performance.

1.4.2 Aperture Coupling Feed

The aperture coupling feed mechanism is chosen for this antenna because of its many advantages over the alternative feed mechanisms, and its easy implementation in MHMIC designs. To achieve a production ready design, an H-shaped aperture is to be used instead of the commonly used simple rectangular slot. This slot shape provides a higher degree of coupling for a given length [34,35] and provides a wider region with near maximum coupling between the aperture and the feedline [42]. The final element design is to be created with a relatively strong coupling level between the patch and aperture to absorb possible manufacturing imperfections.

An aperture coupling feed suffers from one minor manufacturing flaw and that is that care must be taken to properly align the two substrates and then bond them together without adversely effecting performance.

1.4.3 Rectangular Microstrip Elements

This antenna will be designed with rectangular elements as the antenna specification requires linear polarization. The main radiating element will be a rectangular patch that is considerably wider than its resonant length. The width of the patch will be selected to produce an undersirable cross resonance out of our desired operating bandwidth. The parasitic strips added will be coupled to the non-radiating edges of the patch, with the goal of improving the impedance bandwidth to exceed 10%. The level of coupling between the non-resonant edges and the parasitic strips will be varied by changing the spacing between them to obtain the desired bandwidth.

1.5 Thesis Goals

Given the thesis objective stated earlier, the goals of this research are separated into two broad sections of experimental and analytical work which are outlined in the following two sections.

1.5.1 Experimental

The experimental work is directed towards the creation of a microstrip array on a commercial grade microwave laminate that meets or exceeds the required specifications. The experimental work is divided into two parts. The first part is the design of a wideband aperture fed patch antenna element, and verification, that when fabricated this element performs as required. The second part is the design, fabrication, measurement and testing of the full microstrip antenna array.

The element design was originally attempted with the theoretical approximation methods outlined in the theory presented in chapter 2. When two more accurate commercial microstrip analysis software packages became available, they were acquired, and used to analyze the antenna element design created. When good antenna element performance is obtained numerically, the design will be fabricated to verify its performance.

The array design will be performed in a three step process. First the radiating element feed will be slightly modified as required to create a compact array feed network. The introduced modifications will be tested numerically on the analysis packages acquired. The first step in the design process is to determine the array spacing and amplitude distribution required using the numerical approximation developed in the radiation pattern prediction in chapter 3 of this research. This spacing and amplitude distribution will be verified using simulations on the commercial fullwave analysis software packages acquired. These simulations will be performed separately on the azimuth and elevation linear arrays. These results should verify that the required spacing and amplitude distribution is being used. The simulated results will also be able to provide some information on the degree of mutual coupling between elements along these linear array planes. The third part of the array design will be the creation of a computer model of the full antenna array. The analytic array design will be fabricated and measured to verify that the performance meets prescribed specifications.

1.5.2 Analytical

Before one can effectively design an antenna element, one must be able to properly characterize its circuit and radiation properties. An attempt will be made to develop an equivalent circuit model for an aperture fed patch antenna with coplanar parasitics. The circuit analysis procedures pursued will only able to determine the antenna circuits properties, another analysis will be required to determine the radiation properties.

The first equivalent circuit model attempted is based on the transmission line model. The transmission line model used showed a lot of initial potentiala as the problem is simplified into a circuit of discrete circuit elements determined with closed form expressions. This model provides a substantial amount of insight into the operation of a microstrip antenna, but the current model used to represent the aperture fed mechanism is

not accurate enough to be confidently used as a primary design tool. With refinement of the current component models, and development of a more rigorous representation of the aperture coupling mechanism, this model could become an efficient analysis tool for initial design work.

A second equivalent model was attempted, based on the mode matching cavity expansion. This model uses a rigorous analysis of a simplified problem. The derivation uses a modal expansion of the fields in the patch cavity, and feedline, and combines these independent solutions with the application of the reciprocity theorem and the concept of reaction. This model provides a significant amount of detail on the modal behaviour of the structure and has been shown to obtain acceptable results for simple rectangular aperture fed patch antennas. The current published literature does not present the development of a model for the more complicated H-shaped slot. The initial assumption that allows the patch cavity to be considered as a cavity also prevents this model from including the effects of coplanar parasitic elements. When accurate models to represent the two aformentioned circuit components become available, this analysis would provide an invaluable design tool, providing results that should be more accurate than the transmission line model, due to its rigorous analysis origins.

The two analysis methods attempted were unable to represent the entire antenna element. Accurate analysis of the structure is performed using proven, commercially available, accurate, fullwave method of moments analysis software packages. There were a number of commercial software packages available but only two were able to handle the multilayer, aperture feed configuration required, these packages are Ensemble and IE3D. Both of these software tools were acquired to assist in the development of the design pursued in this thesis.

The analysis of the antenna radiation pattern, or directivity, is of great importance to an antenna engineer for the development of a single antenna element or for an array of elements. An attempt is made to develop a radiation model for a single antenna

element. To determine the radiation from the full array, a model using array theory will be included as part of the radiation pattern analysis.

1.6 Thesis Outline

The motivation and background for this research have been provided. Now the rest of this document presents the development of this antenna element in what is believed to be a logical manner.

Chapter 2 provides an overview of the numerical methods used to analyse microstrip antennas. These analysis methods are not original work, but are covered in some detail to provide theoretical content. This section is rather lengthy as both the transmission line model, as presented in [17,45], and the mode matching cavity model, as presented in [15,16,24], are detailed. Most of the parameters required for the dynamic planar waveguide model of the microstrip transmission lines are covered in the transmission line model.

Chapter 3 develops closed form numerical approximations for the radiation pattern of a single patch. Array theory is also presented with most derivations coming from [6]. A sub-section on Taylor Line source distributions is also presented as this was the array amplitude distribution used in the array design for side lobe suppression.

The thesis design work is presented in chapter 4. The chapter starts with some fabrication concerns and some general comments on corporate feed networks. Following this are the element design specifications and the procedure followed to obtain the desired element performance. Next is the array design section with the required performance specifications. Following this is the array element spacing and amplitude distribution required to obtain the desired radiation pattern. A brief description of the corporate feed network design used is included. This chapter ends with the design of a radome used to protect this antenna when it is in use as part of an automotive radar sensor.

Chapter 5 presents the measured results of the fabricated antenna elements and extracts some useful characteristics to determine the antenna's performance. After the antenna element's performance is verified the measured results for the antenna array are scrutinized. The results for a radome covered antenna are presented in the last portion of this chapter.

Chapter 6 provides a summary of the work completed and its significance for the microstrip antenna field. Some comments on future work and possible design improvements are included at the end of this chapter.

CHAPTER 2: Microstrip Antenna Theory and Circuit Models

2.1 General

The objective of the analysis portion of this thesis is to develop relatively simple numerical design tools, to model the antenna and gain some insight into its overall operation. The design pursued in this work is a complex structure that does not lend itself very well to analysis using approximate methods. A simple model is still attempted, with the hope of finding general trends of the antenna performance, and then to modify the appropriate parameters for improvement. Simple numerical models are used throughout microwave engineering. These tools are used to create a first cut at a design that is either refined experimentally or by using much more accurate, and time consuming, fullwave analysis models.

2.1.1 Antenna Analysis Methods

To analyze an aperture fed microstrip antenna a number of analysis methods are available. These methods may be divided into two groups [46]: reduced or simplified analysis, and fullwave analysis. The method that is used depends on the antenna characteristic to be modelled, the accuracy required, and the geometry of the problem to be solved.

Reduced analyses are models that introduce one or more significant approximations to simplify the problem. Included in this list are cavity models that use a magnetic wall boundary around the periphery of the patch, and transmission line models which represent the patch as a transmission line with lumped impedance loads at the radiating edges. These methods were the first to be used for analysis of microstrip antennas, and have been successfully used on many practical designs to provide a good intuitive explanation of the operation. These methods produce only marginal results when applied to problems with thick substrates where a considerable number of surface waves are

present, situations where accurate determination of mutual coupling is required, problems where the effects of feed circuit radiation is required, and for analysis of multilayer antenna configurations.

Fullwave analysis methods accurately account for the dielectric substrate. Models included in this group are the moment method, which uses an accurate Green's function to represent the dielectric layer, the finite difference time domain (FDTD), and the finite element method (FEM). Solutions obtained from fullwave analysis methods can be used to provide all relevant electrical characteristics. These methods are preferred when modelling multilayer configurations, arrays with element mutual coupling effects, and when accurate information is required on feed network mutual coupling and radiation. The main disadvantage of these methods is their high computational cost and low level of user confidence without experimental verification [4].

2.1.2 Fullwave Numerical Analysis of Microstrip

The moment method (MoM) is the most frequently used analysis for microstrip antennas. The solution usually begins with the determination of a Green's function that satisfies the boundary conditions for a unit current located in the plane of the conductors. The Green's function obtained usually assumes infinite dielectric layers and is frequently determined as the solution of the problem transformed into the spectral domain. The spectral domain Green's function is then transformed back into the spatial domain which is usually a formidable task itself. The determination of the Green's function in the spatial domain is actually only part of the preprocessing required to setup the problem for application of the MoM. With the integral equation problem completely defined, the MoM is applied to create a set of linear equations and then solved using matrix methods. A more detailed description of the application of the MoM is included later in a MoM section. The time required for solution increases dramatically with problem size and the solution pro-

cess is repeated for each frequency of interest.

Both FDTD and FEM analyses are more flexible than the MoM but are also numerically less efficient when applied to microstrip problems. The solutions to these methods involves modelling of all dielectric and metal volumes within the problem, and also requires some representation of the truncating border. These methods are frequently used for solutions to problems with arbritrarily conductor or dielectric geoemtries and may be used to solve problems with inhomogeneous dielectrics. The disadvantage of these methods is the significant computation time required in comparison to even the MoM, due to the 3D problem space that must be solved.

In general, fullwave analysis models are computationally intensive and obtain quite accurate results, although these results provide little if any insight to the field structure or radiation mechanism without some prior intuitive knowledge of the fields expected by the user.

2.1.3 Analysis Methods Chosen

Two of the simplest models available are the approaches taken for the analysis of this complex antenna: the Transmission Line Model (TL-Model) and the Mode Matching Cavity Model.

The TL-Model is based on equivalent circuit representation for microstrip transmission lines using closed form approximate expressions [33,43,47]. These transmission line equivalents account for most of the antenna mechanisms and where there are no simple equivalents found, static or quasi-static models will be attempted. The TL-Model lacks the precision of fullwave analysis, yet is useful in that it breaks down a complex problem into lumped circuit components and provides a simple schematic that an antenna designer may use to see the dependencies of the various portions of the antenna on each other. The TL-Model does not provide a method of predicting the radiation patterns so a

separate radiating aperture equivalent model will be required for this purpose.

The mode matching cavity model as developed by [15,16,24] will also be pursued as it does a better job of describing the transfer of energy from the microstrip feedline to the radiating patch. The fields in each region are determined in terms of the various modes that exist in that region independently. These independent mode solutions are then coupled together using reciprocity, to determine the unknowns amplitude, and phase coefficients, for the field components at a common surface between two regions. This analysis assumes the patch to be a cavity with perfect magnetic walls around its periphery, and perfect electric top and bottom walls. These assumption make for a relatively simple solution for the patch modes that exist, but prevent the modelling of any sort of parasitic element coupling. The feedline line is modelled as a dynamic planar waveguide with perfect conducting top and bottom walls, and magnetic walls on its sides. The mode matching cavity model also lacks an accurate way to predict the radiation pattern. This analysis method was not programmed as the effort required was not justified when commercial MoM packages with more accurate results became available.

Commercially available MoM packages (Ensemble and IE3D) will be used to create the initial element design and to optimize it. This process required a lot of time and many iterations, but an extremely well designed antenna element was obtained numerically. Simulations from Ensemble will be used to create antenna elements for experimental verification.

2.2 Proposed Antenna Configuration

2.2.1 Physical Configuration

The geometry for the aperture fed antenna design investigated is shown in the following diagram.

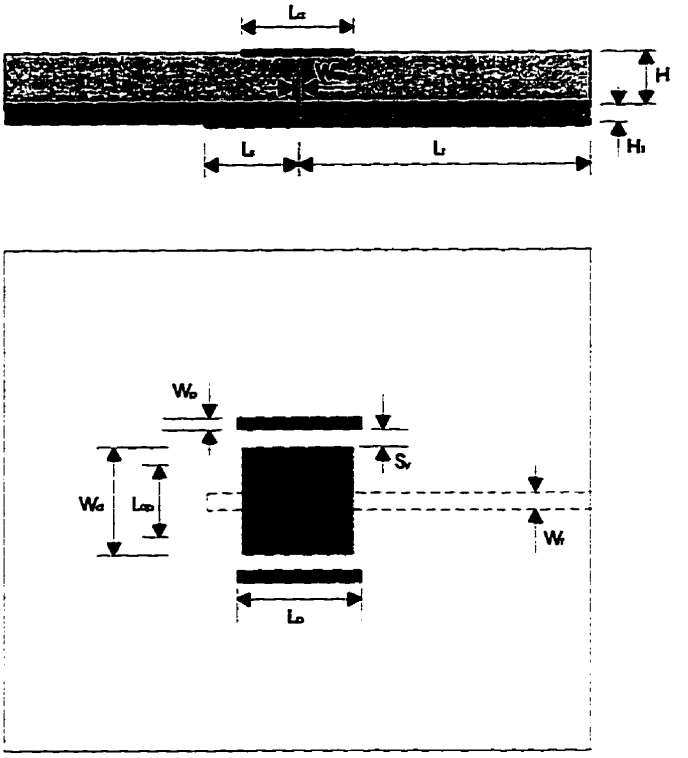

Figure 2.1 Analyzed antenna configuration

The microstrip feedline located below the ground plane excites a perpendicular slot etched in the ground plane, and extends beyond the slot, terminating in an open circuit stub. In this arrangement the fields on the microstripline excite an electric field across the narrow width of the slot which has a maximum at the slot center. This slot field is coupled to a patch located above it on a dielectric substrate. The patch is centered directly over the slot, in such a way as to produce left-right and top-bottom symmetry with respect to the slot. With proper design, there is a strong coupling between the patch and slot. This coupling level may be controlled with slot size, and proper selection of the patch substrate thickness. The parasitic elements included are for enhanced operating bandwidth and act as a

capacitive load on the main patch. They have a resonance that is slightly offset from the main resonance thus creating a double-resonant structure.

2.2.2 Design Parameters of Interest

The antenna geometry of Figure 2.1 shows the 2-layers of this design and all the parameters available for adjustment. The parameters of interest in this antenna design are the thickness of the substrate materials necessary to obtain good performance in the feed circuit, and from the radiating elements. Another parametern studied, is the aperture size required to obtain a well-matched, wideband, operating impedance while trying to minimize back radiation from this aperture. The aperture size must be adjusted whenever the laminate thickness is changed. The center frequency is controlled using the dimensions of the radiating patch and parasitic elements, and also the spacing between these radiating elements. The stub length and a matching circuit will be used to match the antenna to a 50 ohm system impedance.

2.3 Microstrip Patch Transmission Line Model

2.3.1 General

Microstrip antennas are radiating structures that were originally derived from microstrip transmission lines as a means of integrating antennas with feed circuitry on the same substrate. An obvious starting point for a simple analysis is thus the TL-Model that uses a planar waveguide transmission line model to capture the transmission line properties, and uses an open end effect to capture the effects of radiation from the patch.

When modelling microstrip antennas, accuracy of the results are of great importance but numerical efficiency is also required if they are to be well suited for use in computer-aided-design (CAD) programs that possibly require many iterations before

acceptable design results are obtained. The TL-Model uses an equivalent circuit of the antenna that provides some insight into how various parts of the antenna effect the impedance load that a microstrip antenna presents to a feeding circuit.

The original, simple TL-Models [40] were not very accurate due to inaccurate assumptions made at various levels of the development of the equivalent circuit. The accuracy has increased with a new improved TL-Model developed by H.Pues and Van de Capelle [43]. When used on simple microstrip structures the results obtained with this model were claimed to be comparable to those of more complicated full wave analysis methods.

The use of microstrip antennas in most practical applications usually requires multiple elements in an array configuration to achieve the required gain and beamwidth. The design of these arrays require feed structures that are impedance matched to the patch radiators and provide the proper amplitude and phase required at each radiator. Current CAD software is available that represents microstrip network components by equivalent transmission lines. The TL-Model should be easy to integrate into these circuit analysis tools to develop a CAD package for the analysis of a complete array.

2.3.2 The TL-Model Equivalent Circuit

The general configuration of a microstrip antenna consists of an upper conducting patch, a lower conducting ground plane and a substrate that separates the upper and lower conductors.

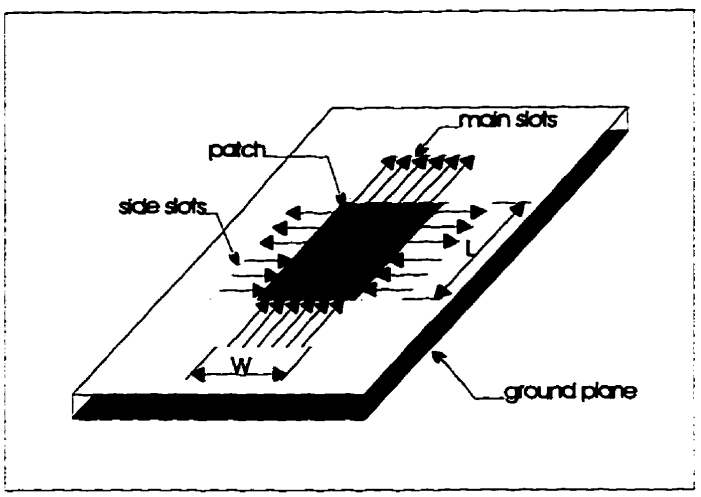

Figure 2.2 Microstrip patch and its associated electric fields

The first step in applying the TL-Model is to develop the equivalent circuit that will be used to determine what model parameters are required to adequately represent a microstrip antenna. The equivalent circuit of the improved TL-Model of Van de Capelle [43] is shown in Figure 2.3.

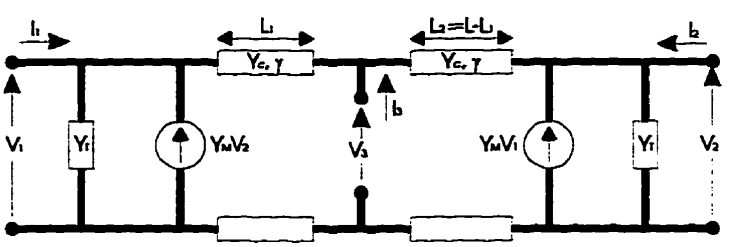

Figure 2.3 Improved transmission line model equivalent circuit

The admittance matrix for this center fed antenna 3-port circuit is [43].

$$[Y] = \begin{bmatrix} Y_s + Y_c\coth(\gamma L_1) & -Y_m & Y_c\,\mathrm{csch}(\gamma L_1) \\ -Y_m & Y_s + Y_c\coth(\gamma L_2) & Y_c\,\mathrm{csch}(\gamma L_2) \\ Y_c\,\mathrm{csch}(\gamma L_1) & Y_c\,\mathrm{csch}(\gamma L_2) & Y_c\coth(\gamma L_1) + Y_c\coth(\gamma L_2) \end{bmatrix} \tag{2.1}$$

where Y_c is the characteristic admittance of the microstrip line formed by the patch, γ_c is the complex propagation constant of this line, and L_1 and L_2 are the lengths from the resonant edges of the patch. If there is only one feed point, as with a coaxial fed patch, assuming $I_1 = I_2 = 0$, and using some trigonometric identities, the input admittance is given as [43]

$$Y_{in} = 2Y_c\left[\frac{Y_c^2 + Y_s^2 - Y_m^2 + 2Y_sY_c\coth(\gamma L) - 2Y_mY_c\,\mathrm{csch}(\gamma L)}{(Y_c^2 + Y_s^2 - Y_m^2)\coth(\gamma L) + (Y_c^2 - Y_s^2 + Y_m^2)\cosh(2\gamma\Delta) + 2Y_sY_c}\right] \tag{2.2}$$

$$\text{where } \Delta = \left|\frac{L}{2} - L_1\right| = \left|\frac{L}{2} - L_2\right| \tag{2.3}$$

In the case of a microstrip fed line $I_2 = I_3 = 0$, and the input admittance is obtained using [17],

$$Y_{in} = \left[\frac{Y_c^2 + Y_s^2 - Y_m^2 + 2Y_sY_c\coth(\gamma L) - 2Y_mY_c\,\mathrm{csch}(\gamma L)}{Y_s + Y_c\coth(\gamma L)}\right] \tag{2.4}$$

The accuracy of the TL-Model depends directly on the accuracy of the expressions used for the model parameters. The self-susceptance B_s is derived from the open-end effect concept, the self-conductance is based on the radiation conductance of an equivalent slot. The mutual admittance is also determined from the equivalent slot concept. The transmission line parameters are based on the static and dynamic waveguide models for microstrips.

2.3.3 Determination Of The TL-Model Parameters

The unknown parameters required from the equivalent circuit of the improved TL-Model are line parameters Y_c and γ_c, the self admittance of the slots Y_s, and the mutual admittance Y_m. The line parameters are expressed in terms of a dynamic planar waveguide model which modifies the open region problem to a closed region.

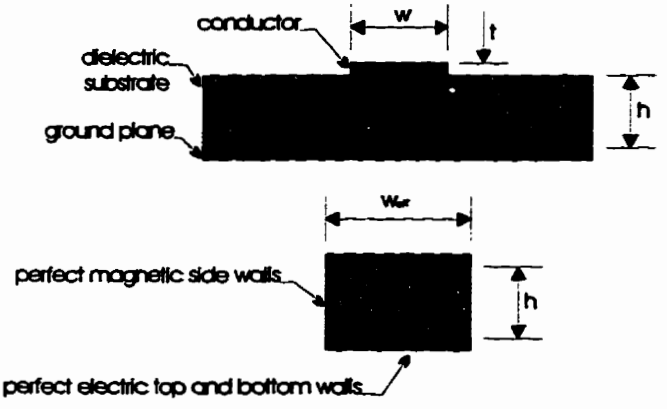

Figure 2.4 Microstrip dynamic planar waveguide model

The first parameter determined in the development of the complete dynamic planar waveguide model is the static effective permittivity $\varepsilon_{reff}(0)$ calculated from [17]:

$$\varepsilon_{reff}(0) = \frac{1}{2}[(\varepsilon_r + 1) + (\varepsilon_r - 1)G] \tag{2.5}$$

where $G = \left(1 + 10\frac{h}{w}\right)^{-AB} - \frac{\ln(4)}{\pi}\frac{t}{\sqrt{wh}}$

$$A = 1 + \frac{1}{18.7}\ln\left(1 + \left(\frac{w}{18.1h}\right)^3\right) + \frac{1}{49}\ln\left(\frac{\left(\frac{w}{h}\right)^4 + \left(\frac{w}{52h}\right)^2}{\left(\frac{w}{h}\right)^4 + 0.432}\right) \tag{2.6}$$

$$B = 0.564\exp\left(-\frac{0.2}{\varepsilon_r + 0.3}\right) \tag{2.7}$$

The next parameter determined is the static effective conductor width $W_{eff}(0)$, which is obtained using [17]:

$$W_{eff}(0) = \frac{2\pi h}{\ln\left(\frac{hF}{w'} + \sqrt{1+\left(\frac{2h}{w'}\right)^2}\right)} \tag{2.8}$$

$$\text{where,} \quad F = 6 + (2\pi - 6)\exp\left(\frac{-4\pi}{3}\left(\frac{h}{w'}\right)^{\frac{3}{4}}\right) \tag{2.9}$$

$$w' = w + \frac{t}{\pi}\left(1 + \ln\left(\frac{4}{\sqrt{\left(\frac{t}{h}\right)^2 + \left(\frac{\frac{1}{\pi}}{\frac{w}{t} + 1.1}\right)^2}}\right)\right) \tag{2.10}$$

Using the static effective width and permittivity, we then determine the static characteristic impedance $Z_c(0)$, which is obtained using [55],

$$Z_c(0) = \frac{Z_{co}}{\sqrt{\varepsilon_{reff}(0)}} \tag{2.11}$$

$$\text{where,} \quad Z_{co} = \frac{\eta_o}{2\pi}\ln\left(\frac{F_1 h}{w} + \sqrt{1+\left(\frac{2h}{w}\right)^2}\right) \tag{2.12}$$

$$F_1 = 6 + (2\pi - 6)\exp\left(-30.666\left(\frac{h}{w}\right)^{0.7528}\right) \tag{2.13}$$

The static planar waveguide model is then used as a basis from which the dynamic planar model is derived. The first dynamic parameter determined is the frequency dependent

effective permittivity $\varepsilon_{reff}(f)$, which is calculated using [56,33]:

$$\varepsilon_{reff}(f) = \varepsilon_r - \frac{\varepsilon_r - \varepsilon_{reff}(0)}{1+P} \tag{2.14}$$

where P is determined from the following series of equations:

$$P = P_1 P_2 [(0.1844 + P_3 P_4) 10fh]^{1.5763} \tag{2.15}$$

$$P_1 = 0.27488 + \left(\frac{w}{h}\right)\left(0.6315 + \left(\frac{0.525}{(1+0.157fh)^{20}}\right)\right) - 0.065683 \exp\left(-8.7513\left(\frac{w}{h}\right)\right) \tag{2.16}$$

$$P_2 = 0.33622(1 - \exp(-0.03442\varepsilon_r)) \tag{2.17}$$

$$P_3 = 0.0363 \exp\left[\left(-4.6\frac{w}{h}\right)\left(1 - \exp\left(-\frac{fh}{3.87}\right)^{4.97}\right)\right] \tag{2.18}$$

$$P_4 = 1 + 2.751\left[1 - \exp\left(-\left(\frac{\varepsilon_r}{15.916}\right)^8\right)\right] \tag{2.19}$$

NOTE: h in mm & f in GHz.

An accurate approximation of the frequency dependent characteristic impedance $Z_c(f)$ is obtained using a power-current definition developed by Jansen and Kirschning [56,33];

$$Z_c(f) = Z_c(0)\left(\frac{R_{13}}{R_{14}}\right)^{R_{17}} \tag{2.20}$$

$$\text{where, } R_1 = 0.03891\varepsilon_r^{1.4} \tag{2.21}$$

$$R_2 = 0.267\left(\frac{w}{h}\right)^{7.0} \tag{2.22}$$

$$R_3 = 4.766\exp\left[-3.228\left(\frac{w}{h}\right)^{0.641}\right] \tag{2.23}$$

$$R_4 = 0.016 + (0.0514\varepsilon_r)^{4.524} \tag{2.24}$$

$$R_5 = \left(\frac{fh}{28.843}\right)^{12.0} \tag{2.25}$$

$$R_6 = 22.20\left(\frac{w}{h}\right)^{1.92} \tag{2.26}$$

$$R_7 = 1.206 - [(0.3144 \cdot \exp(-R_1)) \cdot (1 \cdot \exp(-R_2))] \tag{2.27}$$

$$R_8 = 1 + 1.275 \cdot \left(1 - \exp\left(-0.004625R_3\varepsilon_r^{1.674}\left(\frac{fh}{18.365}\right)^{2.745}\right)\right) \tag{2.28}$$

$$R_9 = 5.086 \cdot R_4 \cdot \left(\frac{R_5}{0.3838 + 0.386R_4}\right)\left(\frac{\exp(-R_6)}{1 + 1.2992R_5}\right)\left(\frac{(\varepsilon_r - 1)^6}{1 + 10(\varepsilon_r - 1)^6}\right) \tag{2.29}$$

$$R_{10} = 0.00044\varepsilon_r^{2.136} + 0.0184 \tag{2.30}$$

$$R_{11} = \frac{\left(\frac{fh}{19.47}\right)^6}{1 + 0.0962\left(\frac{fh}{19.47}\right)^6} \tag{2.31}$$

$$R_{12} = \frac{1}{1 + 0.00245\left(\frac{w}{h}\right)^2} \tag{2.32}$$

$$R_{13} = 0.9408\varepsilon_{reff}(f)^{R_8} - 0.9603 \tag{2.33}$$

$$R_{14} = (0.9408 - R_9) + \varepsilon_{reff}(0)^{R_8} - 0.9603 \tag{2.34}$$

$$R_{15} = 0.707R_{10}\left(\frac{fh}{12.3}\right)^{1.097} \tag{2.35}$$

$$R_{16} = 1 + 0.0503\varepsilon_r^2 R_{11}\left(1 - \exp\left(\frac{-\left(\frac{w}{h}\right)}{15}\right)^6\right) \tag{2.36}$$

$$R_{17} = R_7\left(\left(1 - 1.1241\frac{R_{12}}{R_{16}}\right) \cdot \exp[-0.026(fh)^{1.15656} - R_{15}]\right) \tag{2.37}$$

The dynamic planar waveguide model effective conductor width $W_{eff}(f)$, is obtained using [33]:

$$W_{eff}(f) = \frac{\eta_o}{Z_c(f)\sqrt{\varepsilon_{reff}(f)}} \tag{2.38}$$

The last parameter from the planar waveguide model to be determined is the complex propagation constant. The free space wave number may be obtained using,

$$k_o = 2\pi f \cdot \sqrt{\varepsilon_o \cdot \mu_o} \tag{2.39}$$

This leads to the phase constant β which is the imaginary part of the complex propagation constant. The phase constant is obtain using,

$$\beta = k_o \cdot \sqrt{\varepsilon_{reff}(f)} \tag{2.40}$$

The real part of the complex propagation constant is the line attenuation which consists of

dielectric losses, conductor losses and ground plane losses:

$$\alpha = \alpha_{dielectric} + \alpha_{groundplane} + \alpha_{conductor} \tag{2.41}$$

The dielectric losses are [33]

$$\alpha_{dielectric} = \frac{\beta}{2} \cdot \frac{\varepsilon_r}{\varepsilon_{reff}(f)} \cdot \frac{\varepsilon_{reff}(f) - 1}{\varepsilon_r - 1} \cdot \tan(\delta) \tag{2.42}$$

The conductor losses are [33]

$$\alpha_{conductor} = \frac{\sqrt{\varepsilon_{reff}(0)}}{2\eta_o W_{eff}(0)} \cdot \left(\frac{\frac{w'}{h} + 0.667\frac{w'}{h}}{\frac{w'}{h} + 1.444} \right) \cdot R_{ss} D_{ss} F_s \tag{2.43}$$

$$\text{where, } D_{ss} = 1 + \frac{2}{\pi} \cdot \operatorname{atan}(1.4 \cdot \sqrt{R_{ss} d_s \sigma_s}) \tag{2.44}$$

$$R_{ss} = \sqrt{\frac{\pi f \mu_o}{\sigma_s}} \tag{2.45}$$

$$F_s = 1 + 2\frac{h}{w'} \cdot \left(1 - \frac{1}{\pi}\right) + \left(\frac{w' - w}{t}\right) \tag{2.46}$$

The ground plane losses are [33]

$$\alpha_{groundplane} = \frac{\sqrt{\varepsilon_{reff}(0)}}{2\eta_o W_{eff}(0)} \cdot \left(\frac{\frac{w'}{h} + 0.667\frac{w'}{h}}{\frac{w'}{h} + 1.444} \right) \cdot R_{sg} D_{sg} \tag{2.47}$$

$$\text{where } D_{sg} = 1 + \frac{2}{\pi} \cdot \operatorname{atan}(1.4 \cdot \sqrt{R_{sg} d_g \sigma_g}) \tag{2.48}$$

$$R_{sg} = \sqrt{\frac{\pi f \mu_o}{\sigma_g}} \tag{2.49}$$

where w' is the conductor thickness compensated conductor width as given before in the static model (2.10).

2.3.4 Derivation of The Radiating Slot Admittances

The accuracy of the transmission line model is highly dependent on the accuracy of the expressions for G_s and B_s which represent the radiating slots [33]. In the original TL-Model proposed by Munson [40], it was proposed that the open end terminations may be assumed to be finite length slots cut from an infinitely long, uniformly excited slot. The idea of representing the microstrip antenna open end terminations by equivalent finite length slots, in an infinite conducting plane, provided the simple model necessary to create a closed form representation for the radiating admittance. The original TL-Model uses only two slots as shown below:

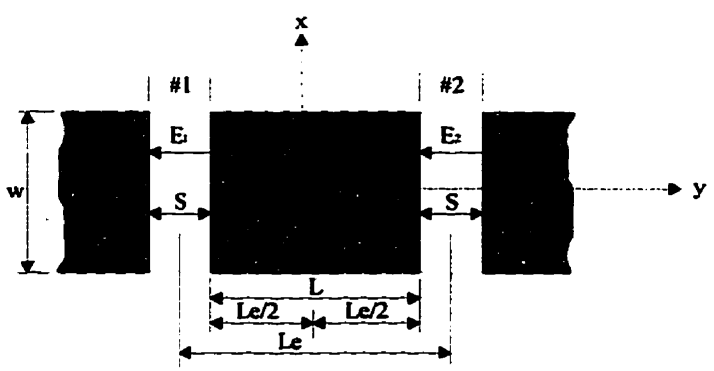

Figure 2.5 Two slot transmission line model

The derivation of the slot admittance Y_s starts with the tangential electric field in the slot apertures which is assumed to be uniform, and expressed as (this derivation follows [17] pp. 535-537):

$$\bar{E}_{ap}(y) = \begin{cases} \frac{V_1}{S} & \left(\frac{L_e - S}{2} \le y \le \frac{L_e + S}{2}\right) \\ \frac{V_2}{S} & \left(\frac{L_e - S}{2} \le -y \le \frac{L_e + S}{2}\right) \\ 0 & elsewhere \end{cases} \tag{2.50}$$

The Fourier transform, with respect to y, of this aperture field is given by [17,43],

$$\tilde{E}_{ap}(k_y) = \int_{-\infty}^{\infty} \bar{E}_{ap} \cdot e^{jk_y y} dy \tag{2.51}$$

As the field in the slot has only a y-component, the Fourier transform is

$$\tilde{E}_{ap}(k_y) = \frac{\sin\left(\frac{k_y S}{2}\right)}{\left(\frac{k_y S}{2}\right)} \cdot \left(V_1 \cdot e^{jk_y \frac{L_e}{2}} + V_2 \cdot e^{-jk_y \frac{L_e}{2}}\right) \tag{2.52}$$

The complex radiated power per unit slot length $(p + jq)$, in terms of the spectral domain variable k_y is [17,43]

$$p = \frac{k}{2\pi\eta} \int_{-k}^{k} \left|\tilde{E}_{ap}(k_y)\right|^2 \cdot \frac{dk_y}{\sqrt{k^2 - k_y^2}} \tag{2.53}$$

and

$$q = \frac{k}{2\pi\eta} \cdot \left[\int_{-\infty}^{k} \left(\left|\tilde{E}_{ap}(k_y)\right|^2 \cdot \frac{dk_y}{\sqrt{k^2 - k_y^2}} \right) + \int_{k}^{\infty} \left(\left|\tilde{E}_{ap}(k_y)\right|^2 \cdot \frac{dk_y}{\sqrt{k^2 - k_y^2}} \right) \right] \tag{2.54}$$

The equivalent network of the two slot configuration can be considered as a symmetrical two-port with self-admittance per unit length $y_s = g_s + jb_s$, and a mutual admittance per unit length $y_m = g_m + jb_m$. Using these quantities the complex radiated power per unit

length is given as [43]

$$p + jq = \frac{1}{2} \cdot y_s^*(|V_1|^2 + |V_2|^2) + y_m^* RE\{V_1 V_2\} \tag{2.55}$$

Taking $V_2 = 0$, (assuming excitation only at V_1), g_s and b_s may be determined [17,43]:

$$g_s = \frac{k}{\pi\eta} \cdot \int_0^k \left(\frac{\sin\left(\frac{k_y S}{2}\right)^2}{\left(\frac{k_y S}{2}\right)^2} \cdot \frac{dk_y}{\sqrt{k^2 - k_y^2}} \right) \tag{2.56}$$

$$b_s = \frac{k}{\pi\eta} \cdot \int_k^\infty \left(\frac{\sin\left(\frac{k_y S}{2}\right)^2}{\left(\frac{k_y S}{2}\right)^2} \cdot \frac{dk_y}{\sqrt{k_y^2 - k^2}} \right) \tag{2.57}$$

These single integrals may be written as double integrals of Bessel functions of the first kind J and second kind Y [17]:

$$g_s = \frac{k}{\eta s^2} \cdot J_o^{ii}(s) \tag{2.58}$$

$$b_s = \frac{k}{\eta s^2} \cdot Y_o^{ii}(s) \tag{2.59}$$

where $s = kS$ the normalized slot width, and the bessel functions used are defined [17] by

$$J_o^{ii}(s) = \int_0^s \int_0^u J_o(v)\,dv\,du \tag{2.60}$$

$$Y_o^{ii}(s) = \int_0^s \int_0^u Y_o(v)\,dv\,du \tag{2.61}$$

The series expansion of J_o and Y_o are [58]

$$J_o(x) = x^n \sum_{m=0}^{\infty} \left[\frac{(-1)^m x^{2m}}{2^{2m+2} m!(n+m)!} \right] \tag{2.62}$$

$$Y_o(x) = \frac{2}{n} \cdot \left[J_o(x) \cdot \left(\ln\left(\frac{x}{2}\right) + \gamma \right) + \sum_{m=1}^{\infty} \left[\frac{(-1)^{m-1} h_m \cdot x^{2m}}{2^{2m} m!} \right] \right] \tag{2.63}$$

$$\text{where, } h_m = \sum_{n=1}^{m} \frac{1}{n} \tag{2.64}$$

$$\gamma = \lim_{s \to \infty} \left(1 + \frac{1}{2} + \ldots + \frac{1}{s} - \ln(s) \right) \approx 0.57721566 \tag{2.65}$$

Integrating the series expansions [17,58] twice yields

$$J_o^{ii}(s) = \frac{s^2}{2} \cdot \left(1 - \frac{s^2}{24} + \frac{s^4}{960} + \ldots \right) \tag{2.66}$$

$$Y_o^{ii}(s) = \frac{s^2}{\pi} \cdot \left[\left(X - \frac{3}{2} \right) - \frac{s^2}{24} \left(X - \frac{19}{12} \right) + \frac{s^4}{960} \left(X - \frac{28}{15} \right) + \ldots \right] \tag{2.67}$$

$$\text{where, } X = \ln\left(\frac{x}{2}\right) + \gamma \tag{2.68}$$

Neglecting the higher order terms (with $s < 1$ an error less than 0.1% was claimed) [17,43]:

$$g_s \approx \frac{k}{2\eta}\left(1-\frac{s^2}{24}\right) \tag{2.69}$$

$$b_s \approx -\frac{k}{2\eta}\left[\left(\ln\left(\frac{s}{2}\right)+\gamma-\frac{3}{2}\right)\left(1-\frac{s^2}{24}\right)+\frac{s^2}{288}\right] \tag{2.70}$$

This defines the per unit length admittance $y_s = g_s + b_s$, to determine the parallel admittance Y_s, across the slot,

$$Y_s = y_s W \tag{2.71}$$

The improved TL-Model of Van de Capelle [17,43] uses amended formulas for the self-admittance. The self-susceptance B_s is determined using the transmission line formula,

$$B_s = Y_c \cdot \tan(\beta \Delta l) \tag{2.72}$$

where Y_c, β and Δl are the characteristic admittance, phase constant and open-end extension of a microstrip line with an aspect ratio $\frac{W}{h}$ of the conducting patch. The characteristic admittance and phase constant were given previously. The line extension was calculated using [47]

$$\Delta l = \frac{h\xi_1\xi_2\xi_5}{\xi_4} \tag{2.73}$$

where

$$\xi_1 = 0.434907\left[\frac{\varepsilon_{reff}(f)^{0.81}+0.26\left(\frac{w}{h}\right)^{0.8544}+0.236}{\varepsilon_{reff}(f)^{0.81}-0.189\left(\frac{w}{h}\right)^{0.8544}+0.87}\right] \tag{2.74}$$

$$\xi_2 = 1 + \frac{\left(\frac{w}{h}\right)^{0.371}}{2.358 \cdot \varepsilon_r + 1} \tag{2.75}$$

$$\xi_3 = 1 + \left(\frac{0.5274 \cdot \operatorname{atan}\left(0.084\left(\frac{w}{h}\right)^{\frac{1.9413}{\xi_2}}\right)}{\varepsilon_{reff}(f)^{0.9236}} \right) \tag{2.76}$$

$$\xi_4 = 1 + 0.0377 \operatorname{atan}\left(0.067\left(\frac{w}{h}\right)^{1.456}\right)(6 - 5\exp(0.036(1 - \varepsilon_r))) \tag{2.77}$$

$$\xi_5 = 1 - 0.218\exp\left(-7.5\left(\frac{w}{h}\right)\right) \tag{2.78}$$

The calculations for the self-conductance G_s follows the derivation used in the simple TL-Model. The electric field in the slot aperture is assumed to be a constant value [17],

$$\bar{E}_{ap} = \frac{V_s}{S}\hat{y} \qquad for\left(|y| \le \frac{S}{2}\right) \qquad and\left(|x| \le \frac{W_{eff}(f)}{2}\right) \tag{2.79}$$

where V_s is the slot excitation voltage and $S = \Delta l$ is the width of equivalent slot.

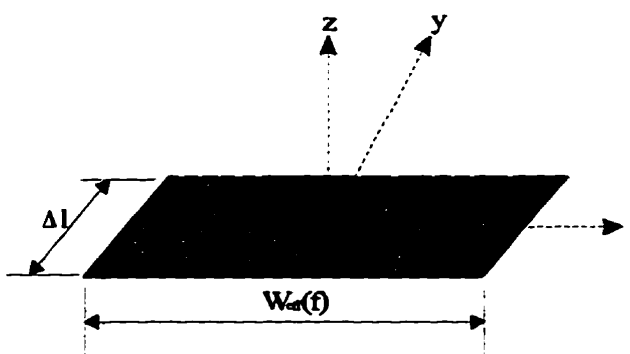

Figure 2.6 Equivalent slot radiator

The spatial Fourier transform of the aperture field is

$$\tilde{E}_{ap} = \int_{-\infty}^{\infty}\int_{-\infty}^{\infty}(\bar{E}_{ap}\cdot e^{jk_x x}\cdot e^{jk_y y})dxdy \tag{2.80}$$

The aperture field only has a y-directed component; thus the Fourier transform only contains a y-component [17].

$$\tilde{E}_y = V_s W_{eff}(f)\left[\frac{\sin\left(\frac{k_x W_{eff}(f)}{2}\right)}{\left(\frac{k_x W_{eff}(f)}{2}\right)}\right]\left[\frac{\sin\left(\frac{k_y S}{2}\right)}{\left(\frac{k_y S}{2}\right)}\right] \tag{2.81}$$

The total power radiated by this slot may be determined by integrating the complex Poynting vector over the aperture surface A,

$$P + jQ = \frac{1}{2}\iint_A \bar{E}_{ap}\times\bar{H}_{ap}^{*}dxdy \tag{2.82}$$

where H_{ap} is the magnetic field in the slot aperture [17].

$$(P+jQ) = \frac{1}{8\pi^2\eta k}\int_{-\infty}^{\infty}\int_{-\infty}^{\infty}(k_x^2|\tilde{E}_y|^2 + |k_y\tilde{E}_y|^2)\frac{dk_x dk_y}{k_z^*} \tag{2.83}$$

where

$$k_z = \begin{cases} \sqrt{k^2-(k_x^2+k_y^2)} & for \quad k^2 \geq k_x^2+k_y^2 \\ -j\sqrt{(k_x^2+k_y^2)-k^2} & for \quad k^2 < k_x^2+k_y^2 \end{cases} \tag{2.84}$$

The complex power may also be expressed in terms of network parameters:

$$(P+jQ) = \frac{1}{2}Y_s^*|V_s|^2 = \frac{1}{2}(G_s - jB_s)|V_s|^2 \tag{2.85}$$

Equating the two complex power equations, expressions may be obtained for G_s and B_s. The previous expression for B_s will be used so only details for G_s are required [17].

$$G_s = \frac{1}{\pi^2 \eta k |V_s|^2} \int_0^k \int_0^{\sqrt{k^2-k_x^2}} (k^2 - k_x^2)|\tilde{E}_y|^2 \frac{dk_y dk_x}{\sqrt{k^2-(k_x^2-k_y^2)}} \tag{2.86}$$

Expanding E_y,

$$G_s = \frac{4}{\pi^2 \eta k_0} \int_0^k \left(\frac{k^2-k_x^2}{k_x^2}\right) \sin\left(\frac{k_x W_{eff}(f)}{2}\right)^2 \int_0^{\sqrt{k^2-k_x^2}} \frac{\sin\left(k_y \frac{S}{2}\right)^2}{\left(k_y \frac{S}{2}\right)^2} \frac{dk_y dk_x}{\sqrt{k^2-(k_x^2-k_y^2)}} \tag{2.87}$$

The inner integral in square brackets may be written as a double integral of the Bessel function of the first kind of order zero [59]. Expanding this Bessel function as a series, then performing a double integration on each term,

$$\int_0^{\sqrt{k^2-k_x^2}} \frac{\sin\left(k_y \frac{S}{2}\right)^2}{\left(k_y \frac{S}{2}\right)^2} \frac{dk_y dk_x}{\sqrt{k^2-(k_x^2-k_y^2)}} = \frac{\pi}{2}\left[1 - \frac{1}{24}(S\sqrt{k^2-k_x^2})^2 + \frac{1}{960}(S\sqrt{k^2-k_x^2})^4\right] \tag{2.88}$$

Truncating the series after the first 2 terms and substituting back into the original equation and integrating the remaining integral [17],

$$G_s = \frac{1}{\pi\eta}\left[\left(wSi(w) + \frac{\sin(w)}{w} + \cos(w) - 2\right)\left(1 - \frac{s^2}{24}\right) + \frac{s^2}{12}\right]\left(\frac{1}{3} + \frac{\cos(w)}{w^2} - \frac{\sin(w)}{w^3}\right) \tag{2.89}$$

where $w = k \cdot W_{eff}(f)$ and $s = k \cdot S$ are normalized slot length and slot width. The

$Si(w)$ function is defined as

$$Si(w) = \int_0^w \frac{\sin(u)}{u} du \tag{2.90}$$

2.3.5 Derivation of Mutual Conductance Representation

The mutual conductance term G_m, is derived from the expression for mutual conductance between infinite slots. An auxiliary coupling term is defined in [17] as

$$F_g = \frac{g_m}{g_s} \tag{2.91}$$

where g_m and g_s are the per-unit-length self and mutual conductances of two TE-excited slots in a perfectly conducting infinite ground plane. An analytical expression for g_s was given as [17]

$$g_s \approx \frac{k}{2\eta}\left(1 - \frac{s^2}{24}\right) \tag{2.92}$$

The expression for g_m is obtained using the complex radiated power per unit slot length $p + jq$ expressed as a Fourier transformed aperture field in terms of the slot voltage V_1 and V_2. Using (2.53) and equating this to the real part of (2.55) an expression for g_m was given as [17]

$$g_m = \frac{k}{\pi\eta}\int_0^k \frac{\sin\left(\frac{k_y S}{2}\right)^2}{\left(\frac{k_y S}{2}\right)^2}\cos(k_y L_{eff})\frac{dk_y}{\sqrt{k^2 + k_y^2}} \tag{2.93}$$

where, $L_{eff} = L + \Delta l$ is the distance between the center of the slots, and $S = \Delta l$ is the width of the equivalent slots. Using a trigonometric identity, the $\sin(a)^2\cos(b)$ part of equation (2.93) is re-written,

$$\sin\left(\frac{k_y S}{2}\right)^2 \cos(k_y Leff) = \frac{1}{2}\sin\left(\frac{k_y(L_{eff}+\Delta l)}{2}\right) + \frac{1}{2}\sin\left(\frac{k_y(L_{eff}-\Delta l)}{2}\right) - \frac{1}{2}\sin\left(\frac{k_y L_{eff}}{2}\right) \tag{2.94}$$

Similar to the derivation of (2.58) from (2.56), following [17] a new expression for g_m is

$$g_m = \frac{k}{2\eta s^2}[J_o^{ii}(l+s) + J_o^{ii}(l-s) - 2J_o^{ii}(l)] \tag{2.95}$$

Expanding the function $J_o^{ii}(l \pm s)$ as a Taylor series around l leads to [17]

$$g_m = \frac{k}{\eta s^2}\sum_{n=1}^{\infty}\frac{s^{2n}}{(2n)!}J_o^{ii(2n)}(l) \tag{2.96}$$

where the superscript $(2n)$ is the 2n-th derivative. Truncating the series after the first two terms g_m is expressed as

$$g_m \approx \frac{k}{\eta}\left[\frac{1}{2!}J_o(l) + \frac{s^2}{4!}J_o^{(2n)}(l)\right] \tag{2.97}$$

Using the identity

$$J_o^{(2n)}(l) = \frac{1}{2}[J_2(l) - J_o(l)] \tag{2.98}$$

The final expression for g_m [17] is

$$g_m \approx \frac{k}{2\eta}\left[\left(1 - \frac{s^2}{24}\right)J_o(l) + \frac{s^2}{24}J_2(l)\right] \tag{2.99}$$

The auxiliary coupling function (2.91) is now expressed as

$$F_g \approx J_o(l) + \frac{s^2}{24 - s^2} J_2(l) \tag{2.100}$$

The mutual conductance G_m of the finite-length slots is then obtained from [17]

$$G_m = G_s F_g \tag{2.101}$$

Pues and Van de Capelle compare the radiation conductance of the four slot model to a far field radiation model. The four slot model used has two main slots of length W_{eff} and width dl and a distance between centers of L_{eff}, and two side slots of length L_{eff} and width dl and a distance W_{eff} between centers. The equivalent radiation conductance of the four slot model was approximated as

$$G_y^{TLModel} = 2(G_s + G_m) \tag{2.102}$$

Comparison of this equivalent conductance to the equivalent radiation conductance obtained using the radiation pattern was claimed to have good agreement [17]. The complete conductance model of the four slot TLM was determined to be acceptable using the current component representation equations.

2.3.6 Derivation of Mutual Susceptance Representation

The derivation of the mutual susceptance was similar to the mutual conductance derivation. The auxiliary coupling function for the susceptances is expressed as the ratio per unit length mutual and self susceptance of two infinite length TE-excited slots [17],

$$F_b = \frac{b_m}{b_s} \tag{2.103}$$

Equating the imaginary part of (2.55) to (2.54) using $V_1 = V_2$ the mutual susceptance term b_m is expressed as [17]

$$b_m = \frac{k}{\eta\pi}\int_k^{\infty}\frac{\sin(k_y S)^2}{(k_y S)^2}\cos(k_y L_{eff})\frac{dk_y}{\sqrt{k_y^2 - k^2}} \tag{2.104}$$

Similar to the g_m derivation b_m may be expressed as [17]

$$b_m = -\frac{k}{2\eta s^2}[Y_o^{ii}(l+s) + Y_o^{ii}(l-s) - 2Y_o^{ii}(l)] \tag{2.105}$$

Expanding the function $Y_o^{ii}(l \pm s)$ as a Taylor series around l leads to [17]

$$b_m = -\frac{k}{\eta s^2}\sum_{n=1}^{\infty}\frac{s^{2n}}{(2n)!}Y_o^{ii(2n)}(l) \tag{2.106}$$

Truncation this series after the first two terms leaves [17]

$$b_m \approx -\frac{k}{\eta}\left[\frac{1}{2!}Y_o(l) + \frac{s^2}{4!}Y_o^{(2n)}(l)\right] \tag{2.107}$$

Using the identity [17]

$$Y_o^{(2n)}(l) = \frac{1}{2}[Y_2(l) - Y_o(l)] \tag{2.108}$$

The final expression for b_m is [17]

$$b_m \approx -\frac{k}{2\eta}\left[\left(1 - \frac{s^2}{24}\right)Y_o(l) + \frac{s^2}{24}Y_2(l)\right] \tag{2.109}$$

A closed form expression for b_s was given in (2.70) that when combined with the above expression for b_m defines the auxiliary susceptance coupling function as [17]

$$F_b = \frac{b_m}{b_s} \cong \frac{\pi}{2} \cdot \frac{Y_o(l) + \frac{s^2}{24 - s^2} \cdot Y_2(l)}{\ln\left(\frac{s}{2}\right) + \gamma - \frac{3}{2} + \frac{\frac{s^2}{12}}{24 - s^2}} \tag{2.110}$$

The first approximation for the mutual susceptance is [17]

$$B_m = B_s F_b \tag{2.111}$$

A correction function K_b is added to compensate for the assumed aperture field distribution. This term is required as the susceptance of the radiating aperture is highly dependent on the aperture field distribution. An expression for this correction function is dependent on w and assumed to be [17]

$$K_b = 1 - \exp(-0.21w) \tag{2.112}$$

2.3.7 Application of The Improved TL-Model

The previous sections have developed, in closed form expressions, all the parameters required to model a patch antenna. To test the accuracy of the component representation of the TL-Model analysis, computer code was written (Appendix A) for a microstrip fed patch. Results from the TL-Model program were compared to the results from both the Ensemble and IE3D fullwave analysis packages (Appendix B). The comparison of the results obtained for this simple problem had the right general form but were considerably different than the results obtained from both MoM packages.

The next step was to try to represent the aperture fed patch. Following [13] the TL-Model is used to develop an equivalent circuit for the aperture fed patch.

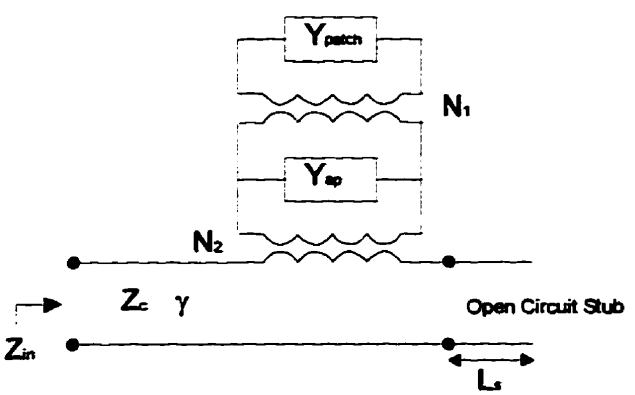

Figure 2.7 Aperture fed patch equivalent TL-Model

The parameters in the above model are specified as follows. The patch admittance is determined using the TL-Model and is represented by Y_{patch}. The aperture admittance Y_{ap} is determined using [12]

$$Y_{ap} = -j\frac{2}{Z_{ca}}\cot\left(\frac{k_a L_a}{2}\right) \tag{2.113}$$

Where the slotline characteristic impedance Z_{ca} and wave number k_a are determined using Cohn's slot analysis method [60]. The transformer ratios are taken directly from

[13] and are given by

$$N_1 = \frac{L_a}{b} \tag{2.114}$$

and

$$N_2 = \frac{L_a}{\sqrt{W_{eff}(f)H_1}} \tag{2.115}$$

The input impedance is finally determined using [13],

$$Z_{in} = \frac{(N_2)^2}{(N_1)^2 Y_{patch} + Y_{ap}} - jZ_c \cot(k_l L_s) \tag{2.116}$$

The TL-Model analysis was programmed and the above aperture feed representation used. The results obtained were compared to published results using fullwave analysis and experimental results. These comparisons showed that the accuracy was less than desired. The model used to represent the coupling from the microstrip line to the aperture, and from the aperture to the patch needs to be improved. With an accurate model for the aperture coupling mechanism, this analysis will be able to quickly provide valuable antenna impedance information.

In the pursuit of an analysis tool for this antenna structure a mode matching analysis was attempted next.

2.3.8 Review of The TL-Model Analysis

The TL-Model is well suited to single layer analysis of patch antennas but produces questionable results when applied to multilayer designs. The major source of analysis error is due to be the crude representation used to model the aperture feed. In gen-

eral this method gave the author considerable insight into the mechanics of this antenna, but in its current form, provided little information on the expected antenna input impedance.

2.4 Mode Matching Analysis for an Aperture Fed Patch Antenna

2.4.1 General

A method derived from the original cavity analysis by Pozar [27] and modified by the authors of [15,16,24] is presented here. The fields inside the cavity and the feedline are represented using a modal expansion. By applying the reciprocity theorem along with a reaction concept, the modal field expansion in the two regions are coupled to represent the effects of one region on the other. The theoretical development requires the application of a cavity model analysis for the rectangular patch, and the dynamic planar waveguide model is used to describe the fields in the microstrip feedline.

2.4.2 Modal Expansion of The Patch Cavity Fields

The cavity model of a microstrip patch antenna starts with the definition of a bounded region. This region is defined as being bounded on the top and bottom with electric walls and by magnetic walls on all the side surfaces creating a rectangular cavity.

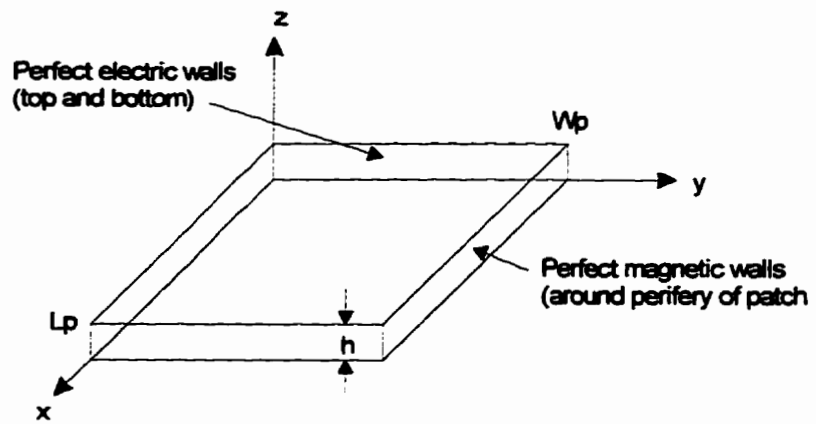

Figure 2.8 Microstrip patch cavity model

With a very thin substrate of height h, it is assumed that there only exist electric fields in the z-direction and magnetic fields transverse to z. The cavity is coupled to a microstrip feedline through a narrow aperture in the ground plane. It is assumed that due to the feedline there exists an induced electric field in the aperture with an x-component only. Application of the field equivalence principle on the slot electric field creates an equivalent magnetic current source with only a y-component. This magnetic current source will produce no y-directed electric field so a TE to y field expansion will be pursued. The wave equation expressed in terms of magnetic and electric vector potentials is,

$$\nabla^2\bar{A} + k^2\bar{A} = 0 \tag{2.117}$$

and

$$\nabla^2\bar{F} + k^2\bar{F} = 0 \tag{2.118}$$

For this TE to y expansion the vector potentials are, $\bar{A} = 0$ and $\bar{F} = \Psi \cdot \hat{y}$. The E and H fields are obtained using

$$\bar{E} = -\nabla \times \bar{F} \tag{2.119}$$

$$\bar{H} = -j\omega\varepsilon\bar{F} + \frac{1}{j\omega\mu}\nabla(\nabla\bar{F}) \tag{2.120}$$

The field componets form (2.119) and (2.120) yield,

$$E_x = \frac{\partial\Psi}{\partial z} \tag{2.121}$$

$$E_y = 0 \tag{2.122}$$

$$E_z = \frac{\partial \Psi}{\partial x} \tag{2.123}$$

$$H_x = \frac{1}{j\omega\mu}\frac{\partial^2 \Psi}{\partial x \partial y} \tag{2.124}$$

$$H_y = \frac{1}{j\omega\mu}\left(\frac{\partial^2}{\partial y^2} + k^2\right)\Psi \tag{2.125}$$

$$H_z = \frac{1}{j\omega\mu}\frac{\partial^2 \Psi}{\partial y \partial z} \tag{2.126}$$

The modal expansion must also obey the wave equation,

$$^2\Psi + k^2\Psi = \tag{2.127}$$

$$\text{where } k = \omega\sqrt{\mu\varepsilon_o\varepsilon_r}$$

When the height of the cavity is very thin it is assumed that the existing fields are constant with respect to z. The solution to the wave equation is known to be of the general form

$$\Psi = [A_x \sin(k_x x) + B_x \cos(k_x x)][A_y \sin(k_y y) + B_y \cos(k_y y)] \tag{2.128}$$

$$\text{where } k^2 = k_x^2 + k_y^2 + k_z^2 \tag{2.129}$$

The unknowns may be reduced using (2.121) to (2.126) along with the boundary conditions imposed on the cavity. The electric walls on the top and bottom surface require that the tangential electric fields vanish on these surfaces, and the tangential magnetic fields vanish on the magnetic side walls. The original field componets now reduce to

$$E_x = 0 \tag{2.130}$$

$$E_y = 0 \tag{2.131}$$

$$E_z = \frac{\partial \Psi}{\partial x} \tag{2.132}$$

$$H_x = \frac{1}{j\omega\mu}\frac{\partial^2 \Psi}{\partial x \partial y} \tag{2.133}$$

$$H_y = \frac{1}{j\omega\mu}\left(\frac{\partial^2}{\partial y^2} + k^2\right)\Psi \tag{2.134}$$

$$H_z = 0 \tag{2.135}$$

Solving (2.133) and (2.134),

$$H_x = \frac{1}{j\omega\mu}[k_x A_x \cos(k_x x) - k_x B_x \sin(k_x x)][k_y A_y \cos(k_y y) - k_y B_y \sin(k_y y)] \tag{2.136}$$

$$H_y = \frac{(k^2 - k_y^2)}{j\omega\mu}[A_x \sin((k_x x) + B_x \cos(k_x x))][A_y \sin((k_y y) + B_y \cos(k_y y))] \tag{2.137}$$

Applying the BC's (boundary conditions) to (2.136)

$H_x = 0$ at $y = 0$ and at $y = W_p$

At $y = 0$, $\quad _x = 0 \rightarrow A_y =$

and at $y = W_p$, $\quad _x = 0 \rightarrow \sin(k_y W_p) = 0 \rightarrow k_y = \frac{n\pi}{W_p}$

Applying the BC's to (2.137)

$$H_y = 0 \text{ at } x = 0 \text{ and at } x = L_p$$

$$\text{At } x = 0, \quad {}_y = 0 \rightarrow B_x =$$

$$\text{and at } x = L_p, \; H_x = 0 \rightarrow \sin(k_x L_p) = 0 \rightarrow k_x = \frac{m\pi}{L_p}$$

Equation (2.128) is now reduced to

$$\Psi = j\omega\mu K_{mn} \sin\left(\frac{m\pi x}{L_p}\right) \cos\left(\frac{n\pi y}{W_p}\right) \tag{2.138}$$

where K_{mn} is a normalization constant to be determined later. The dominant mode of the cavity is determined using

$$k^2 = \left(\frac{m\pi x}{L_p}\right)^2 + \left(\frac{n\pi y}{W_p}\right)^2 \tag{2.139}$$

and $k^2 = \omega^2\mu\varepsilon$

$$\omega_{mn} = \frac{1}{\sqrt{\mu\varepsilon}} \sqrt{\left(\frac{m\pi x}{L_p}\right)^2 + \left(\frac{n\pi y}{W_p}\right)^2} \tag{2.140}$$

This antenna has a larger W_p than L_p and so the mode we are using is m=1 and n=0 (which is not the fundamental mode) with a frequency ω_{10}.

2.4.3 Aperture Coupling of The Patch Cavity

The aperture used in this analysis is a narrow rectangular slot. This shape has been shown to produce maximum coupling at the center of the aperture. The microstrip feedline below the aperture is assumed to induce an electric field across the slot. Using the field equivalence principle an equivalent magnetic current source is obtained.

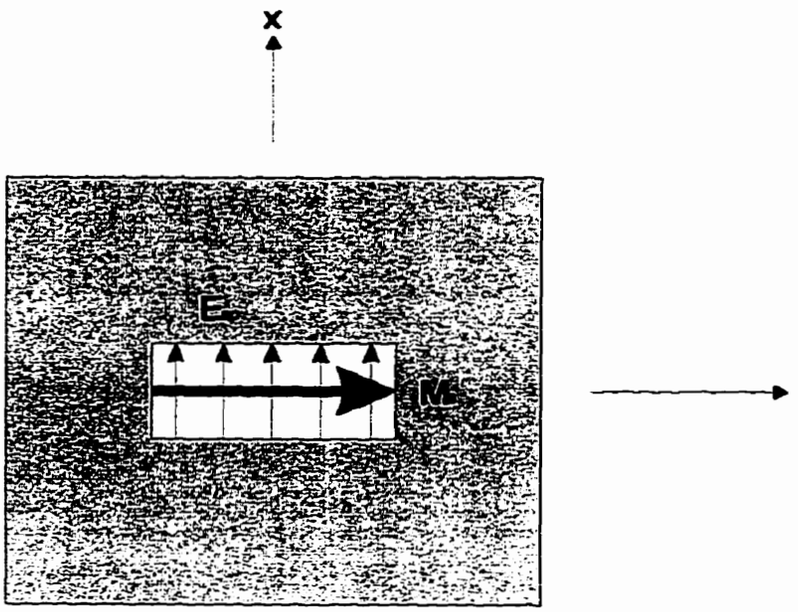

Figure 2.9 Orientation of aperture field

The equivalent aperture magnetic current is, $\overline{M}_s = \hat{n} \times \overline{E}_{ap}$ where $\hat{n}$ is the outward normal vector.

From [11] the induced currents are given by

$$\nabla \times \overline{E} = -j\omega\mu\overline{H} - \overline{M} \tag{2.141}$$

$$\nabla \times \overline{H} = j\omega\varepsilon\overline{E} \tag{2.142}$$

To determine the modal expansion of the fields in the cavity due to the magnetic current

source in the aperture, the H-fields must be expanded using an eigenfunction expansion.

$$\bar{H} = \sum_{mn} b_{mn} \bar{H}_{mn} \tag{2.143}$$

Taking $\nabla \times (\nabla \times \bar{H})$, using (2.141)

$$\nabla \times (\nabla \times \bar{H}) = \omega^2 \mu \varepsilon \bar{H} - j\omega\varepsilon \bar{M} \tag{2.144}$$

Applying the eigenfunction expansion from (2.143),

$$\sum_{mn} b_{mn} [\nabla \times (\nabla \times \bar{H}_{mn})] = \omega^2 \mu \varepsilon \sum_{mn} b_{mn} \bar{H}_{mn} - j\omega\varepsilon \bar{M} \tag{2.145}$$

The aperture magnetic current is the excitation source of the cavity fields but the cavity must also satisfy the source free condition,

$$\nabla \times (\nabla \times \bar{H}_{mn}) = \omega_{mn}{}^2 \mu \varepsilon \bar{H}_{mn} \tag{2.146}$$

combining (2.145) and (2.146)

$$\mu \sum_{mn} (\omega^2 - \omega_{mn}{}^2) b_{mn} \bar{H}_{mn} = -j\omega\varepsilon \bar{M} \tag{2.147}$$

Using mode orthogonality, an expression for b_{mn} is obtained

$$\mu \int_v (\bar{H}_{mn} \cdot \bar{H}_{m'n'}{}^*) dv = \begin{cases} 1 & mn = m'n' \\ 0 & mn \neq m'n' \end{cases} \tag{2.148}$$

where the integral is over the cavity volume. Applying this to (2.147)

$$\mu \sum_{mn} b_{mn} (\omega^2 - \omega_{mn}{}^2) \int_v (\bar{H}_{mn} \cdot \bar{H}_{m'n'}{}^*) dv = -j\omega \sum_{mn} \left(\int_s (\bar{M} \cdot \bar{H}_{mn}) ds \right) \tag{2.149}$$

$$b_{mn} = \sum_{mn} \frac{j\omega}{\omega^2 - \omega_{mn}^2} \int_s (\bar{M} \cdot \bar{H}_{mn}) ds \tag{2.150}$$

The surface integral in (2.150) is over the magnetic current in aperture. Re-writing (2.143) using the solution for b_{mn},

$$\bar{H} = \sum_{mn} \frac{j\omega}{\omega^2 - \omega_{mn}^2} \bar{H}_{mn} \left(\int_s (\bar{M} \cdot \bar{H}_{mn}) ds \right) \tag{2.151}$$

This describes the magnetic modal fields of the cavity due to the magnetic current in the aperture. The normalization factor K_{mn} in (2.138) is required to determine the field components.

$$\bar{H} = H_x \cdot \hat{a}_x + H_y \cdot \hat{a}_y \tag{2.152}$$

$$H_x = -K_{mn} \left(\frac{m\pi}{L_p} \right) \left(\frac{n\pi}{W_p} \right) \cos\left(\frac{m\pi x}{L_p} \right) \sin\left(\frac{n\pi y}{W_p} \right) \tag{2.153}$$

$$H_y = K_{mn} \left(\frac{m\pi}{L_p} \right)^2 \sin\left(\frac{m\pi x}{L_p} \right) \cos\left(\frac{n\pi y}{W_p} \right) \tag{2.154}$$

The normalization factor is determined by applying orthogonality to H which is real,

$$\int_v (\mu \bar{H}_{mn} \cdot \bar{H}_{mn}^*) dv = \int_v \mu \bar{H}_{mn}^2 dv = 1 \tag{2.155}$$

substitution of the magnetic field expressions (2.153), (2.154) into (2.155) yields

$$\int_0^{L_p} \int_0^{W_p} \int_0^h \mu \left[\left(-K_{mn} \left(\frac{m\pi}{L_p} \right) \left(\frac{n\pi}{W_p} \right) \cos\left(\frac{m\pi x}{L_p} \right) \sin\left(\frac{n\pi y}{W_p} \right) \right)^2 + \left(K_{mn} \left(\frac{m\pi}{L_p} \right)^2 \sin\left(\frac{m\pi x}{L_p} \right) \cos\left(\frac{n\pi y}{W_p} \right) \right)^2 \right] dx dy dz = 1 \tag{2.156}$$

Using the integral solutions

$$\int \sin(ax)^2 dx = \frac{x}{2} - \frac{\sin(2ax)}{4a} \tag{2.157}$$

$$\int \cos(ax)^2 dx = \frac{x}{2} + \frac{\sin(2ax)}{4a} \tag{2.158}$$

The integral solution is,

$$\mu K_{mn}^2 \left\{ \left(\frac{m\pi}{L_p}\right)^2 \left(\frac{n\pi}{W_p}\right)^2 \cdot \left(\frac{L_p W_p h}{4}\right) + \left(\frac{m\pi}{L_p}\right)^4 \cdot \left(\frac{L_p W_p h}{4}\right) \right\} = 1 \tag{2.159}$$

The normalization factor solution is,

$$K_{mn} = \frac{2}{m\pi^2} \sqrt{\frac{L_p}{\mu W_p h[(nL_p)^2 + (mW_p)^2]}} \tag{2.160}$$

where $m \neq 0$

This completes the solution of the cavity and the aperture, now the modal expansion solution of the coupling between the feedline and the aperture must be determined.

2.4.4 Modal Expansion of The Microstrip Feedline

To determine the modal field expansion of the E and H fields in the feedline a dynamic planar waveguide model was used [33]. The microstrip line is represented

as a waveguide with electric walls top and bottom and magnetic walls on both sides.

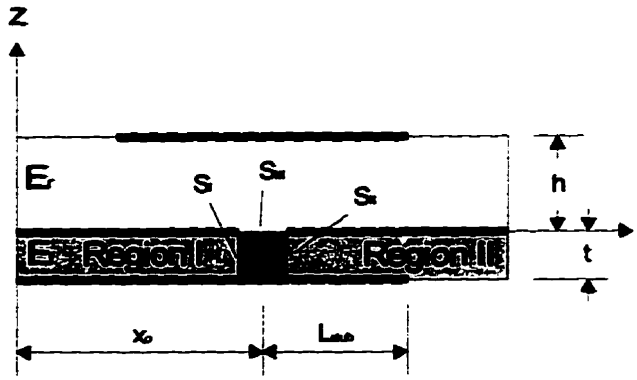

Figure 2.10 Feedline geometry

The feedline is represented using the same dynamic planar waveguide model developed for the TL-Model. The scattered fields in regions *I* and *II* are to the dominant mode of the incident field from region *I* are expanded using TE to *y* modes. The *E* and *H* field components may be determined using (2.119), (2.120), and by applying the boundary condition that Etan=0 on the top and bottom electrical walls and Htan=0 on the side walls. The *E* and *H* fields will be expressed as a dominant mode term, and a summation of all higher order modes. The incident wave is represented by the term $A_o e^{-jk_x x}$.

The solution from [15,16,24] for regions *I* and *II* is

$$\Psi_I^f = A_o e^{-jk_x x} + A_I' e^{-jk_x x} + \sum_{mn} A_{mn}' e^{-j\alpha_{mn} x} \cdot \cos\left[\frac{m\pi}{t}(z+t)\right]\cos\left[\frac{n\pi}{W_{eff}}\left(y - y_o + \frac{W_{eff}}{2}\right)\right] \tag{2.161}$$

$$\Psi_{II}^f = A_{II} e^{-jk_x x} + A_{II}' e^{jk_x x} + \sum_{mn} A_{mn} e^{-j\alpha_{mn} x} \cdot \cos\left[\frac{m\pi}{t}(z+t)\right]\cos\left[\frac{n\pi}{W_{eff}}\left(y - y_o + \frac{W_{eff}}{2}\right)\right] \tag{2.162}$$

$$\text{where} \quad k_x^2 = k_o \varepsilon_{f(f)} - \left(\frac{m\pi}{t}\right)^2 - \left(\frac{n\pi}{W_{eff}}\right)^2 \tag{2.163}$$

$$\alpha_{mn}^2 = \left(\frac{m\pi}{t}\right)^2 + \left(\frac{n\pi}{W_{eff}}\right)^2 - k_o^2 \varepsilon_{f(f)} \tag{2.164}$$

where the summation in (2.161) excludes the dominant mode (mn=00), A_o is the amplitude of the incident field. In region I the unknowns A_I, and A_{mn}' need to be determined; and in region II, A_{mn}, A_{II} and A_{II}' are the expansion coefficients that need to be determined. In region II the coefficients A_{II} and A_{II}' are related through a terminating load at the end of the stub at $x = x_o + L_{stub}$ and by applying perfect magnetic boundary conditions on the end of the line using

$$A_{II}' = A_{II} \cdot e^{-j2k_x(x_o + L_{stub})} \tag{2.165}$$

The complete solution is detailed in [24] and summarized in [15,16] and not included here.

2.4.5 Field Components Determination Using Reciprocity

Application of the reciprocity theorem to the total E and H fields using different sets of test fields over the volume around the slot, allows the determination of the expansion coefficients for the incident and induced fields. The integral form of the Lorentz Reciprocity Theorem for a source free region [6,24] is

$$\iint_S (\bar{E}^a \times \bar{H}^b) \bullet \hat{n} dS = \iint_S (\bar{E}^b \times \bar{H}^a) \bullet \hat{n} dS \tag{2.166}$$

The superscript a denotes total field and b denotes the test field. The test field may be selected arbritrarily as long as it complies with Maxwell's equations along the boundary conditions for that surface.

From the TE to y the $\bar{E}^a$ and $\bar{H}^a$ fields contain the components

$$\bar{E}^a = E_x^a \cdot \hat{a}_x + E_z^a \cdot \hat{a}_z \tag{2.167}$$

$$\bar{H}^a = H_x^a \cdot \hat{a}_x + H_y^a \cdot \hat{a}_y + H_z^a \cdot \hat{a}_z \tag{2.168}$$

and the test fields, similarly,

$$\bar{E}^b = E_x^b \cdot \hat{a}_x + E_z^b \cdot \hat{a}_z \tag{2.169}$$

$$\bar{H}^b = H_x^b \cdot \hat{a}_x + H_y^b \cdot \hat{a}_y + H_z^b \cdot \hat{a}_z \tag{2.170}$$

The left hand side of (2.166) contains contributions from the following surfaces:

$$\iint_S (\bar{E}^a \times \bar{H}^b) \bullet \hat{n} dS = \iint_{S_I} (\bar{E}^a \times \bar{H}^b) \bullet (-\hat{a}_x) dS_1 + \int\int_{S_{II}} (\bar{E}^a \times \bar{H}^b) \bullet \hat{a}_x dS_{II} + \int\int_{S_{III}} (\bar{E}^a \times \bar{H}^b) \bullet \hat{a}_z dIS_{II} \tag{2.171}$$

Performing the cross and dot products these terms reduce to

$$\iint_{S_I} (\bar{E}^a \times \bar{H}^b) \bullet (-\hat{a}_x) dS_1 = \iint_{S_I} (E_z^a \cdot H_y^b) dS_I \tag{2.172}$$

$$\iint_{S_{II}} (\bar{E}^a \times \bar{H}^b) \bullet \hat{a}_x dS_{II} = -\iint_{S_{II}} (E_z^a \cdot H_y^b) dS_{II} \tag{2.173}$$

$$\iint_{S_{III}} (\bar{E}^a \times \bar{H}^b) \bullet \hat{a}_z dS_{III} = \iint_{S_{III}} (E_x^a \cdot H_y^b) dS_{III} \tag{2.174}$$

$$\iint_S (\bar{E}^a \times \bar{H}^b) \bullet \hat{n} dS = \iint_{S_I} (E_z^a \cdot H_y^b) dS_I - \iint_{S_{II}} (E_z^a \cdot H_y^b) dS_{II} + \iint_{S_{III}} (E_x^a \cdot H_y^b) dS_{III} \tag{2.175}$$

The surface S_I is in region I where $E^a = E^I$ and similarly surface S_{II} is in region II where $E^a = E^{II}$. Surface S_{III} is in the aperture given as in [27,31] as a piecewise sinusoidal mode describing the aperture electric field.

$$\bar{E}_{ap} = V \cdot F(y) \cdot \hat{a}_x \tag{2.176}$$

$$\text{where} \quad F(y) = \begin{cases} \frac{1}{W_s} & for\left(\frac{-W_{eff}}{2} \le y \le \frac{W_{eff}}{2}\right) \\ \frac{1}{W_s} \cdot \frac{\sin\left(k_s\left(\frac{L_{ap}}{2} - y\right)\right)}{\sin\left(\frac{k_s}{2}(L_{ap} - W_{eff})\right)} & for\left(\left|\frac{W_{eff}}{2}\right| < |y| \le \left|\frac{L_{ap}}{2}\right|\right) \\ 0 & otherwise \end{cases} \tag{2.177}$$

The test fields used are selected to make the evaluation of the reciprocity equations simple to evaluate and apply in the complex poynting theorem used to create an equivalent circuit model. A field with unit amplitude and the same field configuration as the fundamental mode of the feedline is selected. This is a propagating mode travelling in the positive x-direction:

$$\bar{E}^b = E_y^b \tag{2.178}$$

$$\bar{H}^b = H_x^b \tag{2.179}$$

where the scaler function used is

$$_f = A_o e^{-jk_x x} \tag{2.180}$$

All other field components are zero. These test fields and the total fields are used in (2.166) to give one expression for the dominant mode modal coefficients. This reciprocity procedure is applied to the negative travelling dominant mode to determine the coefficients. The higher order modal coefficients are also obtained using reciprocity, once for a forward travelling, and then for the backward travelling modes. The field solutions from reciprocity for all these modes will now be used to create an equivalent circuit using the Poynting Theorem.

2.4.6 Equivalent Circuit Representation

Since all relevant field components in each region are now known, the Poynting Theorem may now be applied to the fields in the slot volume to determine an expression for the input admittance of an aperture fed patch. Pozar [27] has shown that the discontinuity introduced by the slot is seen as a simple series impedance to the microstrip line.

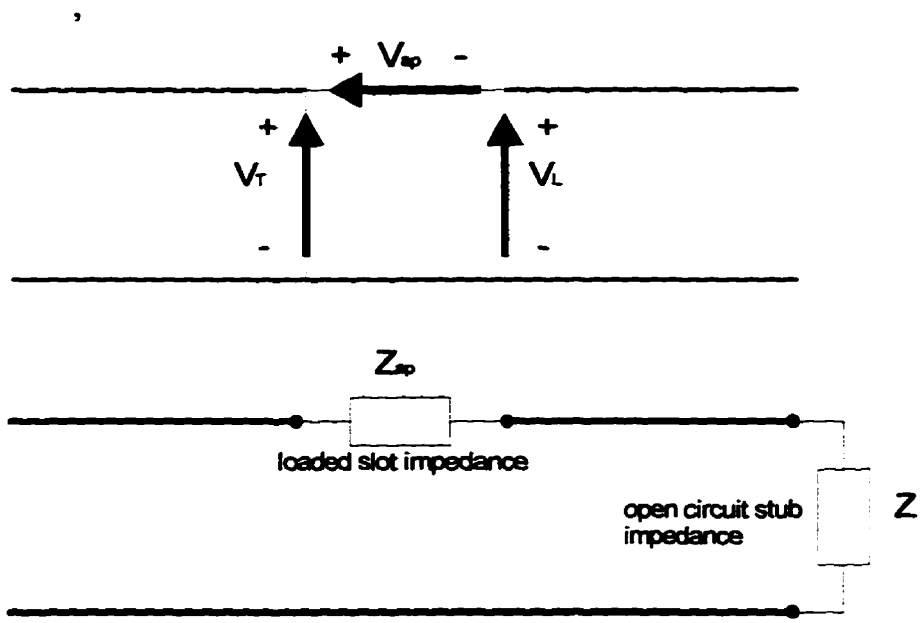

Figure 2.11 Slot voltages and equivalent circuit

The Poynting Theorem states that the complex power supplied by sources inside a volume V is

$$P_s = -\iiint_V (\bar{E} \bullet \bar{J} + \bar{H}^* \bullet \bar{M}) dv \qquad (2.181)$$

with no sources within the volume V, $P_s = 0$. The time averaged power leaving V across the S surfaces is

$$P = \frac{1}{2}\iint_S \bar{E} \times \bar{H}^* \bullet \hat{n} \cdot ds \tag{2.182}$$

The time averaged stored energy in the electric and magnetic fields are

$$W_e = \frac{1}{2}\iiint_V \varepsilon |\bar{E}|^2 dv \tag{2.183}$$

$$W_m = \frac{1}{2}\iiint_V \mu |\bar{H}|^2 dv \tag{2.184}$$

For a lossless problem, the components in the Poynting Theorem for time harmonic fields are

$$P_s = P + j\omega(W_m - W_e) \tag{2.185}$$

The slot is extremely thin so to a first order approximation the volume integration may be neglected and one is left with the power crossing this surface, $P = 0$. This problem has three contributing surfaces so the total power across these surfaces are related as,

$$\frac{1}{2}\int_{S_I} (\bar{E}_I \times \bar{H}_I) \bullet \hat{a}_x ds = \frac{1}{2}\int_{S_{II}} (\bar{E}_{II} \times \bar{H}_{II}) \bullet \hat{a}_x ds + \frac{1}{2}\int_{S_{ap}} E_a H_y ds \tag{2.186}$$

Substitution of the proper E and H components and with some manipulation (2.186) is reduced to

$$y_{in} V_T^2 = y_L V_L^2 + y_s V_s^2 \tag{2.187}$$

The complete derivation for the above equivalent impedances is included in [24] but the summarized version from [15,16] is included here. The term y_L represents the admittance of the matching stub as seen at the slot, y_S is the total admittance comprised of the higher order modes y_e, and the slot-fed antenna y_a, related to y_S using

$$y_S = N^2 \cdot (y_e + y_a) \tag{2.188}$$

The complete antenna admittance is

$$y_{in} = y_L + y_S \tag{2.189}$$

The equivalent circuit for the antenna using the above terms is shown in Figure 2.12.

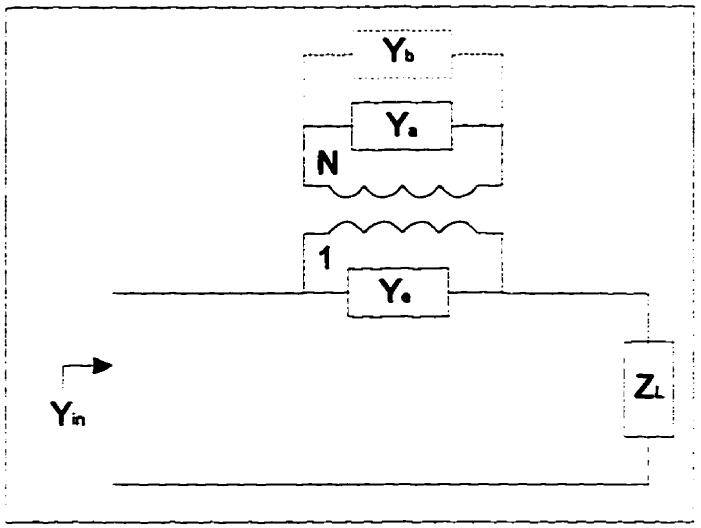

Figure 2.12 Aperture fed microstrip patch equivalent circuit

The higher order mode admittance y_e is much smaller than y_a and was neglected here. The term, y_b in the above figure represents the back radiation, which for a small aperture is assumed to be negligible and was also ignored. The aperture fed admittance was expanded using a Laurent series expansion around the desired resonance ω_{10} and given [16] as

$$y_a = \frac{jW_{ap}^2}{\omega\mu}\left(\frac{2}{Lp_{eff}Wp_{eff}}\right)\left[\frac{\omega^2\alpha_o^2}{2h}\sin\left(\frac{\pi x_o}{Lp_{eff}}\right)^2\left(\frac{1}{\omega_{10}'(\omega-\omega_{10}')}-\frac{1}{2\omega_{10}'^2}\right)+\sum_{mn}\frac{k_0^2\varepsilon a_{eff}-\left(\frac{n\pi}{Wp_{eff}}\right)}{\gamma_n}\right. \tag{2.190}$$
$$\left.\alpha_n^2\sin\left(\frac{m\pi x_o}{Lp_{eff}}\right)^2\frac{\cos(k_z h)}{k_z\sin(k_z h)}\right]$$

$$\text{where} \quad \alpha_n = \int_0^{Wp_{eff}} F(y)\cos\left(\frac{n\pi y}{Wp_{eff}}\right)dy \tag{2.191}$$

$$\omega_{10} = \frac{c_o\pi}{Lp_{eff}\sqrt{\varepsilon a_{eff}}} \tag{2.192}$$

$$\omega_{10}' = \omega_{10}\left(1 - \frac{j}{2Q}\right) \tag{2.193}$$

$$k_z = \left(k_o^2\varepsilon a_{eff} - \left(\frac{m\pi}{Lp_{eff}}\right)^2 - \left(\frac{n\pi}{Wp_{eff}}\right)^2\right)^{\frac{1}{2}} \tag{2.194}$$

$$\varepsilon_{ap} = \sqrt{\frac{\varepsilon_r + \varepsilon_f}{2}} \tag{2.195}$$

The turns ratio N is approximated using a stripline formula [48]:

$$N = \frac{\Delta V}{V} = \frac{1}{t\sqrt{F(k)}} \int_0^{\frac{L_{ap}}{2}} \frac{\sin\left(K\left(\frac{L_{ap}}{2} - x\right)\right)}{\sqrt{1 + k^2\sinh\left(\frac{\pi x}{2t}\right)^2}}dx \tag{2.196}$$

$$\text{where} \quad F(k) = \int_0^{1\infty}\int_0^{\infty} \frac{dx'dy'}{\left|1 + k^2\cosh\left(\frac{\pi(x' + jy')}{2}\right)^2\right|} \tag{2.197}$$

Reducing (2.197), it becomes

$$F(k) = \int_0^{1\infty}\int_0^{\infty} \frac{dx'dy'}{\left[1 + k^4\left(\sinh\left(\frac{\pi x'}{2}\right)^2 + \cos\left(\frac{\pi y'}{2}\right)^2\right) - 2k^2\left(\sinh\left(\frac{\pi x'}{2}\right)^2\cos\pi y' + \cos\left(\frac{\pi y'}{2}\right)^2\right)\right]^{\frac{1}{2}}} \tag{2.198}$$

$$k = \operatorname{sech}\left(\frac{\pi W_f}{4t}\right) \tag{2.199}$$

$$K = \left(\frac{2\pi}{\lambda}\right)\sqrt{\varepsilon_{ap}} \tag{2.200}$$

This completes the parameter models required for the mode matching cavity analysis. This method was not programmed as the availability of a proven commercial fullwave analysis package made an accurate numerical analysis available.

2.4.7 Review of The Mode Matching Analysis

The mode matching cavity model is an efficient analysis tool capable of providing antenna input impedance information for a rectangular aperture fed patch antenna, but currently it is not able to represent more complicated aperture shapes. This method is derived from a rigorous theoretical analysis and provides better results than the TL-Model. The cavity model will need some modification to be able to represent the effects of parasitic antenna elements. The analysis of the antenna element pursued in this thesis requires solution to a complex geometry that exceeds the capabilities of the mode matching cavity method. To accurately model this antenna problem a fullwave analysis is required. The creation of such a tool is outside the scope of the intended research and commercial software was acquired to provide the required analysis.

2.5 The Moment Method

2.5.1 General

The application of the method of moments (MoM) reduces a linear functional equation, to a linear system of equations that can be solved using mature numerical

techniques. In this application, the MoM is used to solve an integral equation [49]. The procedure starts by obtaining a functional equation valid for the electromagnetic problem to be solved. The integral equation will be presented as [50]

$$\int_D G(\bar{r},\bar{r}')f(\bar{r}')dr' = \rho(\bar{r}) \qquad r \in D \tag{2.201}$$

where G is the Green's function, ρ is the known excitation term and f is the unknown function to be determined. The unknown function f is then expressed as a series of known (and preferably simple) basis functions with unknown coefficients, where the basis function is $\phi_n(\bar{r})$ with n=1,2,3,..., N [50].

$$f(\bar{r}) = \sum_{n=1}^{N} c_n \phi_n(\bar{r}) \tag{2.202}$$

The variable c_n is the unknown to be determined. Substituting expansion (2.202) into (2.201) the original integral equation becomes [50],

$$\sum_{n=1}^{N} c_n \int_D G(\bar{r},\bar{r}')\phi_n(\bar{r}')dr' = \rho(\bar{r}) \tag{2.203}$$

The next step in this procedure is to take an inner product of (2.203) with a testing function $\chi_m(\bar{r})$ where m=1,2,3,..., N. The original integral equation is reduced to [50]

$$\sum_{n=1}^{N} K_{mn} c_n = b_m \tag{2.204}$$

and, $K_{mn} = \langle \chi_m(\bar{r}), \int_D G(\bar{r},\bar{r}')\phi_n(\bar{r}')dr' \rangle$

$$b_m = \langle \chi_m(\bar{r}), \rho(\bar{r}) \rangle \tag{2.205}$$

The inner product is usually an integral with respect to r over the region defined by D. The application of the MoM results in a $N \times N$ linear system that is solved for the unknown coefficients in the series expansions using matrix techniques.

2.5.2 The Electric Field Integral Equation

There are two choices for the integral equation, an electric field integral equation (EFIE), or a magnetic field integral equation (MFIE). The MFIE is known to be numerically unstable when thin embedded conductors are encountered [50], which is the usual microstrip conductor profile, so the EFIE is usually preferred. The EFIE is applied only to the surfaces of the conductors and the sole unknown is the true surface current. The boundary condition between dielectric layers is [50]

$$\bar{E}_t = \hat{a}_z \times Z_s \bar{H}_t \tag{2.206}$$

and the boundary condition for the embedded conductors is [50]

$$\hat{n} \times \bar{E} = Z_s \hat{n} \times \bar{J}_s \tag{2.207}$$

where Z_s is the surface impedance. The current $\bar{J}_s$ is the electric surface current excited by the excitation field $\bar{E}^e$. This surface current $\bar{J}_s$ creates a scattered or diffracted field $\bar{E}^d$. A generalized form of the EFIE for the unknown surface current $\bar{J}_s$ is [50]

$$\hat{n} \times \bar{E}^e(\bar{r}) = -\hat{n} \times \int_S G(\bar{r}, \bar{r}') \bar{J}_s(\bar{r}') ds' + Z_s \hat{n} \times \bar{J}_s \tag{2.208}$$

When attacking a multilayer problem the boundary conditions between layers must be included in the derivation of the Green's function which is not a trivial task.

2.5.3 The Green's Function

The most efficient technique using the MoM and formulating the Green's function is to transform the problem to the spectral domain and calculate the Green's function there [50]. Once in the spectral domain there are two choices available. The EFIE may be written and solved in the spectral domain and the surface current $\overline{J}_s$ transformed back into the spatial domain. The second alternative is once the Green's function is determined in the spectral domain, transform it back into the spatial domain and solve the EFIE there. The latter alternative is believed to be more flexible when solving odd conductor shapes and provides more physical insight into the problem.

There are many options available for the potential used to create the Green's functions while in the spectral domain. The most popular potential is Sommerfeld's vertical electric dipole (VED) [50]. This potential choice requires the use of a numerical integration to transform the Green's function back to the spatial domain as there usually is no analytic transform solution available [50].

2.5.4 Testing and Basis Functions

There are several choices available for the basis functions $\phi_n(\bar{r})$ and the testing functions $\chi_m(\bar{r})$. The point matching method uses the simplest choices for these functions, a pulse function as a basis function, and a delta function as the testing function. Due to these function selections, there are no integrations required, and the analytical preprocessing is extremely simple. The price paid for this simplicity is the need for more test points within a problem space for accurate results thus producing larger matrices. A common basis and testing function choice for spectral domain solutions is Galerkin's method with identical rooftop functions for basis and testing. A negative effect of the Galerkin's method is that double integrals have to be evaluated for each matrix element. The benefit is that substantially smaller matrix size is required for the same accuracy obtained using

point matching methods. Results from Galerkin's method have been shown to be variational [50].

2.6 Microstrip Transmission Lines and Feed Circuitry Analysis

There is some concern about the level of feed losses that will be obtained using the commercial grade laminate at Ku-Band. To accurately model feed line losses and radiation a fullwave analysis is required. The feed circuit for this antenna will be designed and analyzed using the commercial MoM package IE3D.

To minimize the feed circuit radiation losses, curvilinear surfaces will be used instead of abrupt right angle bends wherever possible. Simple models do not represent these circuits properly so a fullwave analysis will be used to create the complete feed circuit.

CHAPTER 3: Radiation Models and Array Analysis

3.1 General

The objective of this portion of the thesis work is to develop a numerical model which will predict the radiated far-field for a rectangular microstrip patch above a ground plane. This simple model will be used with an array factor to determine the expected radiated field pattern for specific array configurations. The method used here to predict the patch radiation pattern makes some assumptions for the field distribution and neglects the radiation contributed by the parasitic elements. This will introduce some prediction errors but these effects are secondary to the array pattern which is the primary end goal for this antenna design.

3.1.1 Numerical Models for Radiation Prediction

The method used here is based on the fact that the radiated field from a microstrip patch antenna is primarily due to the fringing fields between the edge of the microstrip top conductor and the ground plane. The first models developed were based on this procedure and assumed that the fringing fields at the radiating edges could be represented as two uniform field slots separated by the patch length [40]. This model was constructed using the field equivalence principle to create an equivalent radiating aperture model. The element radiated far-field is determined using the radiation from a single slot and multiplying it with a two element array factor to account for the second radiating patch edge. This approximate element pattern is then multiplied by an array factor to determine the expected radiation pattern for an array of these elements. The array factor will be obtained using array theory that will be included after the derivation of the element radiation pattern.

3.1.2 Goal For Pattern Prediction

The goal of this radiation pattern prediction is to obtain a closed form model for quick and efficient determination of the element radiated far field. With the element pattern approximated, the array spacing, amplitude and phasing information will be obtained using array factor multiplication. This closed form pattern prediction obtains solutions extremely fast on current computers and many iterations may be performed in a very short time. To verify the radiation pattern analysis developed here, the commercial array pattern software ARPS will be used.

3.2 Radiated Far Field Using The Field Equivalence Principle

3.2.1 Application of the Field Equivalence Principle

The development performed here follows Balanis [6] whose derivation is a general implementation of the field equivalence principle. The field equivalence principle is a principle by which actual sources are replaced by equivalent sources.

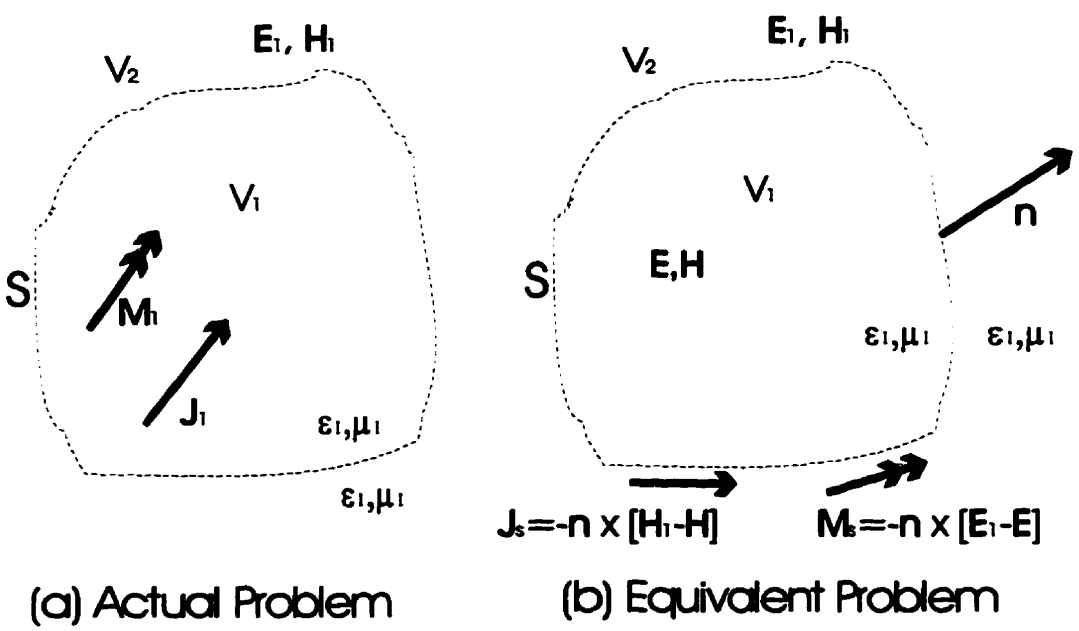

Figure 3.1 Actual and equivalent problem models

The equivalent problem of in Figure 3.1 shows the original sources $\bar{J}_1$ and $\bar{M}_1$ which are to be removed. Assume that there exists a field $\bar{E}$ and $\bar{H}$ inside S and a field $\bar{E}_1$ and $\bar{H}_1$ outside of S. For these fields to exist inside and outside of S they must satisfy the boundary conditions on the tangential electric and magnetic components. On the surface S there must exist the equivalent sources.

$$\bar{J}_s = \hat{n} \times [\bar{H}_1 - \bar{H}] \tag{3.1}$$

$$\bar{M}_s = -\hat{n} \times [\bar{E}_1 - \bar{E}] \tag{3.2}$$

These equivalent sources radiate into an unbounded space of the same medium everywhere. The equivalent sources are said to be equivalent only in the external region V_2. Since the currents radiate into an unbounded space, the fields may be determined using [6] for the geometry shown in Figure 3.2.

$$\bar{A} = \frac{\mu}{4\pi} \iiint_V \bar{J} \frac{e^{-jkR}}{R} dv' \tag{3.3}$$

$$\bar{F} = \frac{\varepsilon}{4\pi} \iiint_V \bar{M} \frac{e^{-jkR}}{R} dv' \tag{3.4}$$

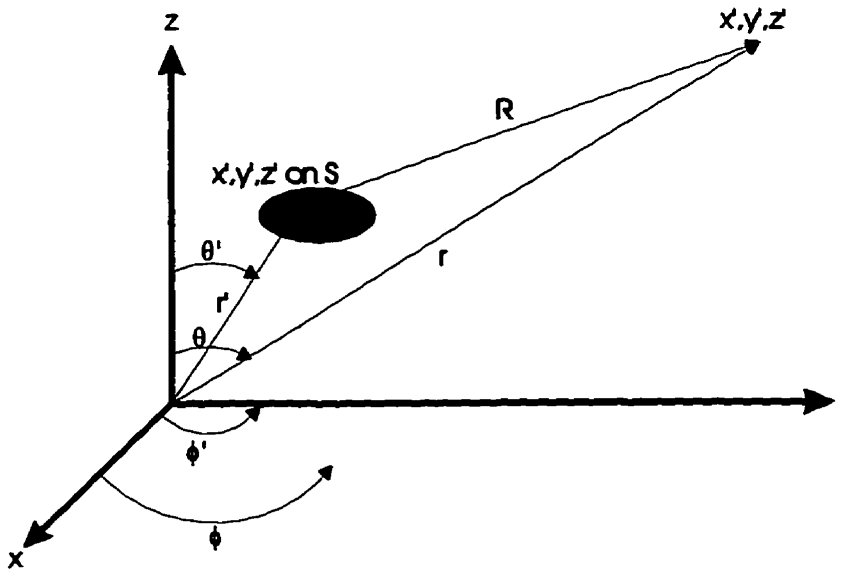

Figure 3.2 Geometry used for calculation of A and F

The steps involved in the application of the equivalence principle for a waveguide aperture in an infinite electric ground plane is derived below. This derivation is analogous to the radiating slots in a microstrip antenna [6].

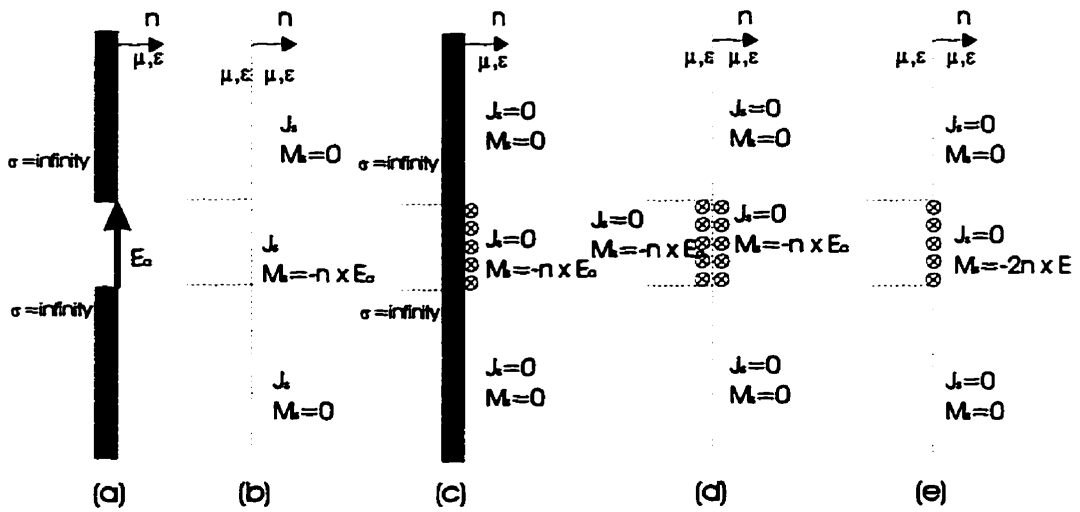

Figure 3.3 Application of field equivalence principle on a waveguide

The original problem in (a) is represented by an infinite plane and the equivalent current densities $\bar{J}_s$ and $\bar{M}_s$. Since the tangential $\bar{E}$ vanishes over the conductor a magnetic cur-

rent density $\bar{M}_s$ exists over the aperture (b). The electric current density $\bar{J}_s$ is non-zero and as yet unknown. Assume a conducting sheet approaches the surface and shorts out the electric current $\bar{J}_s$. The magnetic current still exists and radiates through the conductor (c). The conducting sheet is replaced using image theory (d). Simplifying the remaining components leads to (e). The final equivalent has been reduced to a radiating aperture alone in a uniform medium and the radiated fields determined using $\bar{A}$ (magnetic vector potential), and $\bar{F}$ (electric vector potential).

3.2.2 Radiation Equations

The fields radiated by the electric and magnetic current sources $\bar{J}_s$ and $\bar{M}_s$ in an unbounded medium can be computed using $\bar{A}$ (magnetic vector potential) and $\bar{F}$.(electric vector potential) where the integration is performed over the entire surfaces where the currents $\bar{J}_s$ and $\bar{M}_s$ exist. These equations provide valid solutions for all observation points. The main difficulty in applying this method is the inability to perform the integrations required to determine $\bar{A}$ and $\bar{F}$. Using far-field approximations the complexity of these integrations is reduced considerably. For a far-field observation point $\bar{R}$ the following approximations are used:

$$\text{for phase variations:} \quad R \cong r - r'\cos\Psi \tag{3.5}$$

$$\text{and for amplitude variations:} \quad R \cong r \tag{3.6}$$

The variable Ψ is the angle between the vectors r and r'. The primed coordinates represent the space occupied by the sources J_s and M_s over which the integration must be performed. The unprimed coordinates represent the observation point. The equations for $\bar{A}$ and $\bar{F}$ can be re-written as [6]

$$\bar{A} = \frac{\mu}{4\pi}\iint_S \bar{J}_s \frac{e^{-jkR}}{R} ds' \cong \frac{\mu e^{-jkr}}{4\pi r}\bar{N} \tag{3.7}$$

$$\bar{N} = \iint_s \bar{J}_s e^{-jkr'\cos\psi} ds' \tag{3.8}$$

$$\bar{F} = \frac{\varepsilon}{4\pi}\iint_S \bar{M}_s \frac{e^{-jkR}}{R} ds' \cong \frac{\mu e^{-jkr}}{4\pi r}\bar{L} \tag{3.9}$$

$$\bar{L} = \iint_s \bar{M}_s e^{-jkr'\cos\psi} ds' \tag{3.10}$$

The dominant far-field consists of the θ and ϕ components of the $\bar{E}$ and $\bar{H}$ fields [6].

$$(E_A)_\theta \cong -j\omega A_\theta \tag{3.11}$$

$$(E_A)_\phi \cong -j\omega A_\phi \tag{3.12}$$

$$(E_F)_\theta \cong -j\omega F_\theta \tag{3.13}$$

$$(E_F)_\phi \cong -j\omega F_\phi \tag{3.14}$$

the $\overline{E_F}$ and $\overline{H_A}$ field components are expressed as [6]

$$(E_F)_\theta \cong \eta(H_F)_\phi = -j\omega\eta F_\phi \tag{3.15}$$

$$(E_F)_\phi \cong (-\eta)(H_F)_\theta = j\omega\eta F_\theta \tag{3.16}$$

$$(E_A)_\theta \cong -\frac{(E_A)_\phi}{\eta} = j\omega\frac{A_\phi}{\eta} \tag{3.17}$$

$$(E_A)_\phi \cong \frac{(E_A)_\theta}{\eta} = -j\omega\frac{A_\theta}{\eta} \tag{3.18}$$

Combining the above components the total $\bar{E}$ and $\bar{H}$ fields are [6]

$$E_r \cong 0 \tag{3.19}$$

$$E_\theta \cong -\frac{jke^{-jkr}}{4\pi r}(L_\phi + \eta N_\theta) \tag{3.20}$$

$$E_\phi \cong \frac{jke^{-jkr}}{4\pi r}(L_\theta - \eta N_\phi) \tag{3.21}$$

$$H_r \cong 0 \tag{3.22}$$

$$H_\theta \cong \frac{jke^{-jkr}}{4\pi r}(N_\phi - \eta L_\theta) \tag{3.23}$$

$$H_\phi \cong -\frac{jke^{-jkr}}{4\pi r}\left[N_\theta + \frac{L_\phi}{\eta}\right] \tag{3.24}$$

The variables N_θ, N_ϕ, L_θ and L_ϕ can be obtained using

$$\bar{N} = \iint \bar{J}_s e^{jkr'\cos\psi} ds' = \iint [J_x\hat{a}_x + J_y\hat{a}_y + J_z\hat{a}_z] e^{jkr'\cos\psi} ds' \tag{3.25}$$

$$\bar{L} = \iint \bar{M}_s e^{jkr'\cos\psi} ds' = \iint [M_x\hat{a}_x + M_y\hat{a}_y + M_z\hat{a}_z] e^{jkr'\cos\psi} ds' \tag{3.26}$$

Using the rectangular to spherical transformation matrix [6]

$$\begin{bmatrix} A_r \\ A_\theta \\ A_\phi \end{bmatrix} = \begin{bmatrix} \sin\theta\cos\phi & \sin\theta\sin\phi & \cos\theta \\ \cos\theta\cos\phi & \cos\theta\sin\phi & -\sin\theta \\ -\sin\phi & \cos\phi & 0 \end{bmatrix} \begin{bmatrix} A_x \\ A_y \\ A_z \end{bmatrix} \tag{3.27}$$

The spherical components are [6]

$$N_\theta = \iint_S [J_x\cos\theta\cos\phi + J_y\cos\theta\sin\phi - J_z\sin\theta]e^{jkr'\cos\psi}ds' \tag{3.28}$$

$$N_\phi = \iint_S [-J_x\sin\phi + J_y\cos\phi]e^{jkr'\cos\psi}ds' \tag{3.29}$$

$$L_\theta = \iint_S [M_x\cos\theta\cos\phi + M_y\cos\theta\sin\phi - M_z\sin\theta]e^{jkr'\cos\psi}ds' \tag{3.30}$$

$$L_\phi = \iint_S [-M_x\sin\phi + M_y\cos\phi]e^{jkr'\cos\psi}ds' \tag{3.31}$$

When solving for rectangular apertures with uniform current distributions, the integration over the aperture is in its easiest form. The difference in the effective path length and differential source area for apertures in various planes is included below.

<u>For an aperture in yz-plane</u>

The available current sources are J_y, J_z, M_y, M_z , the remaining current sources are assumed to be zero. The difference in the effective path length and differential source area for this orientation is

$$r'\cos\psi = y'\sin\theta\sin\phi + z'\cos\theta \tag{3.32}$$

$$ds' = dy'dz' \tag{3.33}$$

For apertures in the xz-plane

The available sources are J_x, J_z, M_x, M_z ,

$$r'\cos\psi = x'\sin\theta\cos\phi + z'\cos\theta \tag{3.34}$$

$$ds' = dx'dz' \tag{3.35}$$

For apertures in the xy-plane

The sources are available J_x, J_y, M_x, M_y ,

$$r'\cos\psi = x'\sin\theta\cos\phi + y'\sin\theta\sin\phi \tag{3.36}$$

$$ds' = dx'dy' \tag{3.37}$$

The radiating aperture of the microstrip patch antenna is assumed to have a constant E-field, this reduces the complexity of the analytic integrations of (3.28) to (3.31). These integrations may be solved analytically using the integral solution,

$$\int_{-\frac{c}{2}}^{\frac{c}{2}} e^{j\alpha z}dz = c\left[\frac{\sin\left[\frac{\alpha}{2}c\right]}{\left[\frac{\alpha}{2}c\right]}\right] \tag{3.38}$$

3.2.3 Directivity

The directivity is defined as the ratio of the radiation intensity for the antenna under test (AUT) compared to an isotropic radiator. The directivity of an aperture is found by first determining the radiation intensity $U(\theta, \phi)$ for the far-field region electric and magnetic fields [6].

$$U(\theta, \phi) = \frac{1}{2} Re[(E_\theta a_\theta + E_\phi a_\phi) \times (H_\theta a_\theta + H_\phi a_\phi)^*] = \frac{1}{2\eta}[|E_\theta|^2 + |E_\phi|^2] \tag{3.39}$$

in a normalized form this reduces to [6]

$$U_N(\theta, \phi) = [|E_\theta|^2 + |E_\phi|^2] = B_o F(\theta, \phi) \tag{3.40}$$

The calculation of directivity starts with the determination of the total radiated power.

$$P_{rad} = \int_0^{2\pi} \left[\int_0^{\pi} U(\theta, \phi)(\sin\theta d\theta) \right] d\phi \tag{3.41}$$

The directivity is the ratio of the maximum radiation intensity to the total radiated power and is obtained using

$$Do = \frac{4\pi U(\theta, \phi)|_{MAX}}{P_{rad}} \tag{3.42}$$

where the 4π term is included for the solid angle.

The directivity is also obtained using the term at the end of (3.40) as

$$Do = \frac{4\pi F(\theta, \phi)|_{MAX}}{\int_0^{2\pi} \left[\int_0^{\pi} F(\theta, \phi) \sin\theta d\theta \right] d\phi} \tag{3.43}$$

A frequently used plot of an antenna radiation pattern is the directive gain. The directive gain is the antenna radiation gain, with respect to an isotropic radiator, in any arbitrary direction. This is usually expressed as [6]

$$D_g(\theta,\phi) = \frac{4\pi F(\theta,\phi)}{\int_0^{2\pi}\left[\int_0^{\pi} F(\theta,\phi)\sin\theta d\theta\right]d\phi} \tag{3.44}$$

3.3 Radiation Pattern Prediction for A Microstrip Patch Antenna

3.3.1 Application of The Equivalent Radiating Aperture Method

The microstrip patch antenna orientation used or the radiation pattern derivation is shown in Figure 3.4.

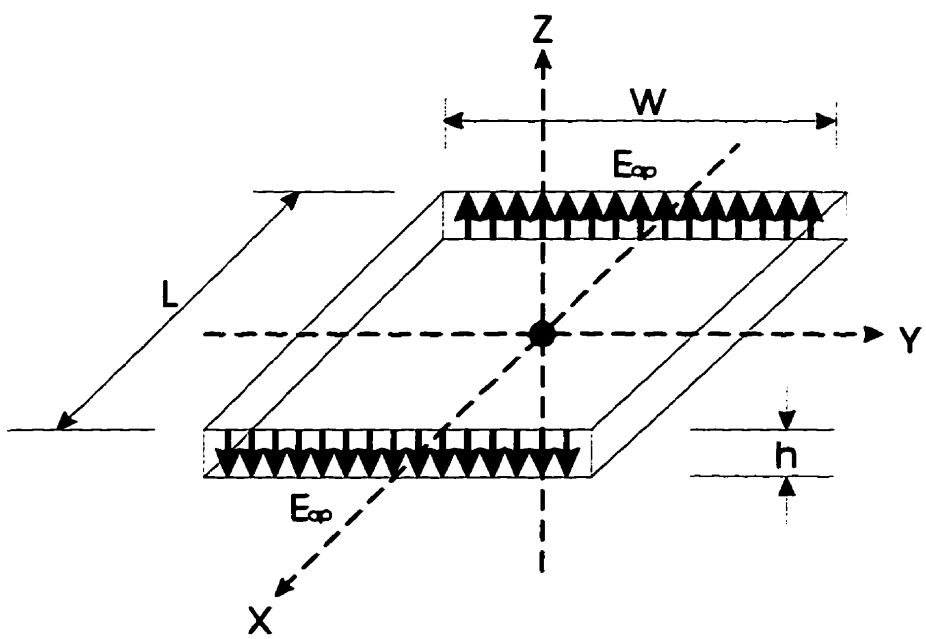

Figure 3.4 Microstrip patch orientation

The above figure shows that the radiating slots lie in the yz-plane. Following the

equivalence principle derivation in the last section the equivalent magnetic current is obtained using

$$\bar{M}_s = 2 \cdot \bar{E}_{ap} \times \hat{n} = 2 \cdot E_0 \cdot \hat{a}_z \times \hat{a}_x = 2 \cdot E_0 \cdot (-\hat{a}_y) = -2 \cdot E_0 \cdot \hat{a}_y \tag{3.45}$$

Using this equivalent magnetic current source, the electric vector potential is determined using (3.9),(3.10), with the terms in (3.30) and (3.31) simplified to [6]

$$L_\theta = \iint_S [M_y \cos\theta \sin\phi] e^{jkr' \cos\psi} ds' \tag{3.46}$$

$$L_\phi = \iint_S [M_y \cos\phi] e^{jkr' \cos\psi} ds' \tag{3.47}$$

Since the aperture lies in the yz-plane the $r' \cos\psi$ phase term is replaced with (3.32) and the differential area with (3.33), the variables L_θ and L_ϕ are now determined using [6]

$$L_\theta = [M_y \cos\theta \sin\phi] \left[\int_{-\frac{w}{2}}^{\frac{w}{2}} e^{jky' \sin\theta \sin\phi} dy' \right] \left[\int_{-\frac{h}{2}}^{\frac{h}{2}} e^{jkz' \cos\theta} dz' \right] \tag{3.48}$$

$$L_\phi = [M_y \cos\phi] \left[\int_{-\frac{w}{2}}^{\frac{w}{2}} e^{jky' \sin\theta \sin\phi} dy' \right] \left[\int_{-\frac{h}{2}}^{\frac{h}{2}} e^{jkz' \cos\theta} dz' \right] \tag{3.49}$$

Using the analytic solution (3.38), the terms in (3.48) and (3.49) are,

$$L_\theta = [M_y \cos\theta \sin\phi] \left[w \frac{\sin\left[k\frac{w}{2}\right]}{\left[k\frac{w}{2}\right]} \right] \left[h \frac{\sin\left[k\frac{w}{2}\right]}{\left[k\frac{h}{2}\right]} \right] \tag{3.50}$$

$$L_\phi = [M_y \cos\phi]\left[w\frac{\sin\left[k\frac{w}{2}\right]}{k\frac{w}{2}}\right]\left[h\frac{\sin\left[k\frac{w}{2}\right]}{\left[k\frac{h}{2}\right]}\right] \tag{3.51}$$

From L_θ the component E_ϕ is determined, and similarly from L_ϕ the component E_θ is determined. The simplified equations are

$$E_\theta = -B_o L_\phi \tag{3.52}$$

$$E_\phi = B_o L_\theta \tag{3.53}$$

The terms in (3.52) and (3.53) provide the radiation for a single aperture, to account for the second aperture, a two element array factor is used. The working neccessities are presented here as later in this chapter array factors are covered in more detail. Array theory assumes point sources along an axis, in this case we have the radiating apertures along the x-axis and separated by the resonant length L. The following figure shows the orientation.

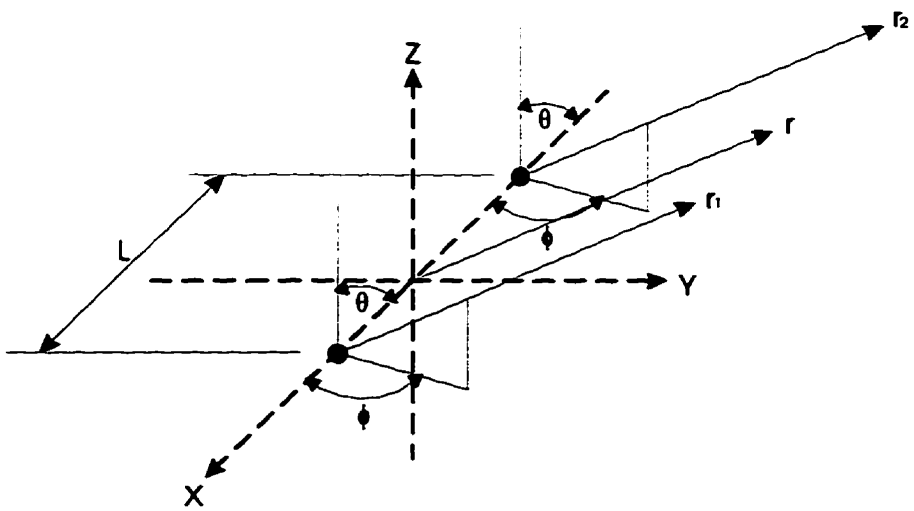

Figure 3.5 Aperture array factor orientation

The array factor is due to the phase variation between the two point sources. In the above diagram the distances r_1 and r_2 may be approximated by the following:

$$\text{for phase variations} \quad r_1 \cong r - \frac{L}{2}\sin\theta\cos\phi \tag{3.54}$$

$$\text{and} \quad r_2 \cong r + \frac{L}{2}\sin\theta\cos\phi \tag{3.55}$$

$$\text{and for amplitude variations} \quad r_1 \cong r_2 \cong r \tag{3.56}$$

The total radiated far-field is [6]

$$\bar{E}_T = \bar{E}_1 + \bar{E}_2 \tag{3.57}$$

$$\bar{E}_T = \hat{a}_\theta G(\theta, \phi)\left[\frac{e^{-jkr_1}}{r_1} + \frac{e^{-jkr_2}}{r_2}\right] \tag{3.58}$$

$$\bar{E}_T = \hat{a}_\theta \frac{G(\theta, \phi)}{r}[e^{-jkr_1} + e^{-jkr_2}] \tag{3.59}$$

$$\bar{E}_T = \hat{a}_\theta \frac{G(\theta, \phi)}{r}\left[e^{-jk\left[r + \frac{L}{2}\sin\theta\cos\phi\right]} + e^{-jk\left[r - \frac{L}{2}\sin\theta\cos\phi\right]}\right] \tag{3.60}$$

$$\bar{E}_T = \hat{a}_\theta \frac{G(\theta, \phi)e^{-jkr}}{r}\left[e^{-jk\left[\frac{L}{2}\sin\theta\cos\phi\right]} + e^{-jk\left[-\frac{L}{2}\sin\theta\cos\phi\right]}\right] \tag{3.61}$$

$$\bar{E}_T = \hat{a}_\theta \frac{G(\theta, \phi)e^{-jkr}}{r}\left[2\cos\left[k\frac{L}{2}\sin\theta\cos\phi\right]\right] \tag{3.62}$$

The two slot array factor for this microstrip patch orientation is

$$AF(\theta, \phi) = 2\cos\left[k\frac{L}{2}\sin\theta\cos\phi\right] \tag{3.63}$$

In the next section the microstrip patch antenna radiation patterns are presented for the model derived here.

3.3.2 Predicted Radiation Pattern for a Microstrip Patch Antenna

The radiation pattern was predicted with a computer program based on the following equations. The radiation from an aperture

$$F(\theta,\phi) = [|E_\theta|^2 + |E_\phi|^2] \tag{3.64}$$

and equation (3.63) for the two aperture array factor. The total radiation is obtained using

$$F_T(\theta,\phi) = F(\theta,\phi)\cdot|AF(\theta,\phi)|^2 \tag{3.65}$$

The directivity was determined using

$$D_g = 4\pi\cdot\frac{F_T(\theta,\phi)}{\int_0^{2\pi}\left[\int_0^{\pi}F_T(\theta,\phi)\cdot\sin\theta d\theta\right]d\phi} \tag{3.66}$$

and the directive gain

$$D_o = 4\pi\cdot\frac{F_T(\theta,\phi)\big|_{MAX}}{\int_0^{2\pi}\left[\int_0^{\pi}F_T(\theta,\phi)\cdot\sin\theta d\theta\right]d\phi} \tag{3.67}$$

The computer code for this calculation is included in Appendix-C. The microstrip patch predicted radiation pattern is shown in Figure 3.6 for the two principle planes.

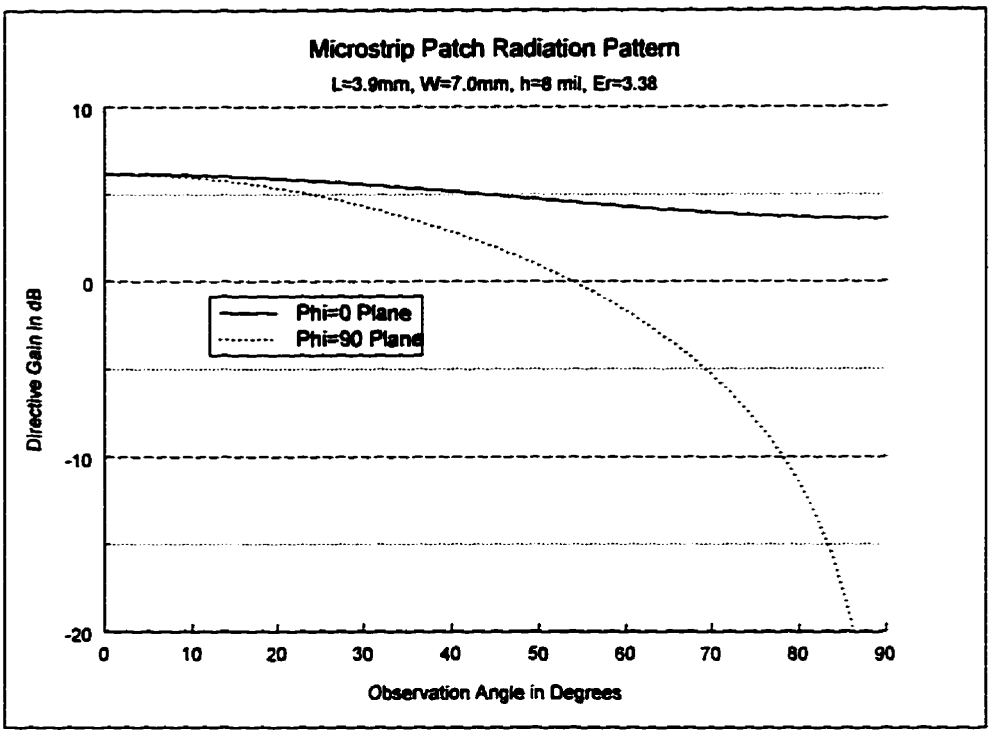

Figure 3.6 E (Phi=0) and H (Phi=90) plane radiation pattern for a MPA

3.4 Array Theory

3.4.1 General

The radiation patterns obtained with a single element in general have relatively wide beamwidthes and a low value of directivity. To obtain narrow beamwidthes, high directivity, low side lobes or some other particularly desirable radiation characteristic, a group of antenna elements is used. This group of antenna elements is usually referred to as an antenna array or simply as an array. The design of an array is in general a three step process. The first step is the selection of the radiating elements to be used. The second step is the determination of the required array geometry to achieve the desired characteristic. The final step is to determine the amplitude and phase relationship between these elements to meet the desired design specifications.

The array may be comprised of identical or different elements. The use of

identical elements makes for a simpler numerical analysis and is the path chosen for this design. The elements may be positioned with periodic or aperiodic spacings, in linear, circular, rectangular, spherical and triangular geometries. The antenna design followed in this thesis is a planar array comprised of linear arrays in two planes perpendicular to each other. The amplitude of each element is a parameter of interest when side lobe levels are of concern. Amplitude distributions formulated in published literature on Chebyshev [62], and Taylor distributions [51] have been shown to produce specific radiation pattern characteristics.

3.4.2 Uniform Spacing and Amplitude Linear Array Factor

An array factor of identical elements may be derived by considering the element locations as point sources. The actual total field is obtained by multiplying the array factor for the isotropic point sources by the field pattern for a single element.

$$F_{Total}(\theta, \phi) = F_{Element}(\theta, \phi) \cdot |AF(\theta, \phi)|^2 \tag{3.68}$$

A simple configuration is a linear array that is oriented along one of the principle axes. The example presented here is a N-element linear array along the z-axis. The array factor is the contribution from each element in the array.

$$AF = 1 + e^{j(kd\cos\theta)} + e^{j2(kd\cos\theta)} + e^{j3(kd\cos\theta)} + \ldots + e^{j(N-1)(kd\cos\theta)} \tag{3.69}$$

$$AF = \sum_{n=1}^{N} e^{j(n-1)(kd\cos\theta)} \tag{3.70}$$

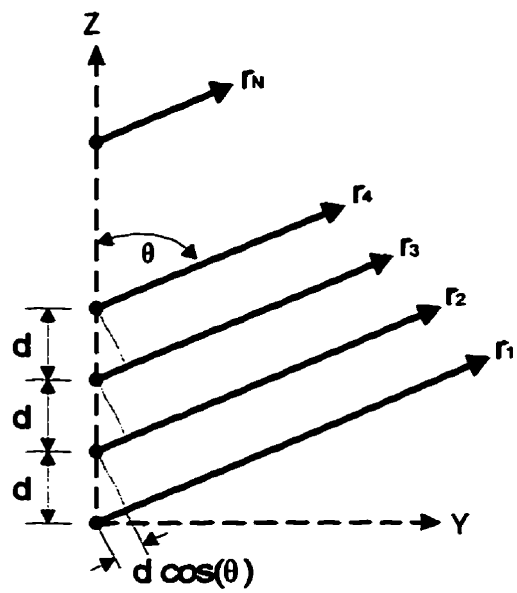

Figure 3.7 Far-field geometry for a N-element array along z-axis

$$AF = \sum_{n=1}^{N} e^{j(n-1)\psi} \tag{3.71}$$

$$\text{where } \psi = kd\cos\theta \tag{3.72}$$

In the process of simplifying, both sides of (3.69) are multiplied by $e^{j\psi}$,

$$AFe^{j\psi} = e^{j(kd\cos\theta)} + e^{j2(kd\cos\theta)} + \ldots + e^{j(N-1)(kd\cos\theta)} + e^{jN(kd\cos\theta)} \tag{3.73}$$

Subtracting (3.69) from (3.73) leaves,

$$AF(e^{j\psi} - 1) = (-1 + e^{jN\psi}) \tag{3.74}$$

which for an array reference point centered along the array reduces to

$$AF = \left[\frac{\sin\left[\frac{N}{2}\psi\right]}{\sin\left[\frac{1}{2}\psi\right]}\right] \tag{3.75}$$

The above equation for small values of ψ may be approximated with,

$$AF \approx \left[\frac{\sin\left[\frac{N}{2}\psi\right]}{\left[\frac{1}{2}\psi\right]}\right] \tag{3.76}$$

This array factor has a maximum of N, normalizing to a maximum array factor value of unity,

$$(AF)_n \approx \frac{1}{N}\left[\frac{\sin\left[\frac{N}{2}\psi\right]}{\left[\frac{1}{2}\psi\right]}\right] \tag{3.77}$$

$$(AF)_n \approx \left[\frac{\sin\left[\frac{N}{2}\psi\right]}{\left[\frac{N}{2}\psi\right]}\right] \tag{3.78}$$

When applied to linear arrays along different axis the ψ changes to different equations. Our elevation plane linear array runs along the x-axis, and uses

$$\psi = kd\sin\theta\cos\phi \tag{3.79}$$

While our azimuth plane linear array runs along the y-axis and uses

$$\psi = kd\sin\theta\sin\phi \tag{3.80}$$

The resulting radiation pattern for a uniform amplitude 4-element linear array that runs

parallel to the x-axis was predicted to produce the following radiation pattern.

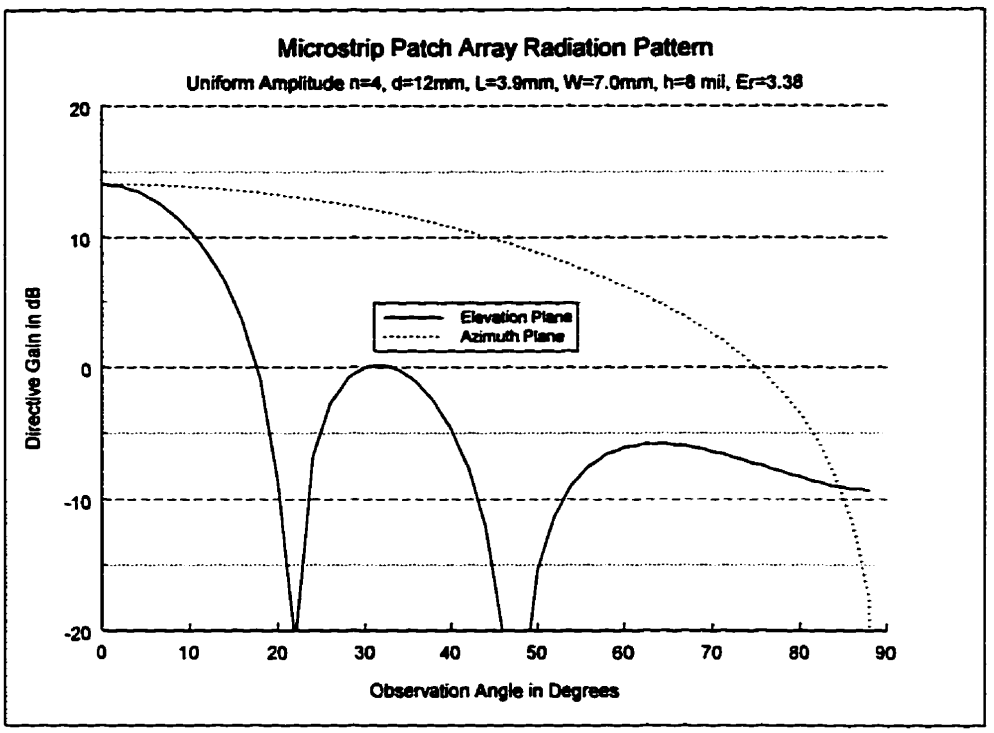

Figure 3.8 Elevation pattern predicted for 4 element uniform linear MPA

A four element azimuth plane, linear array was also simulated with the results shown in Figure 3.9,

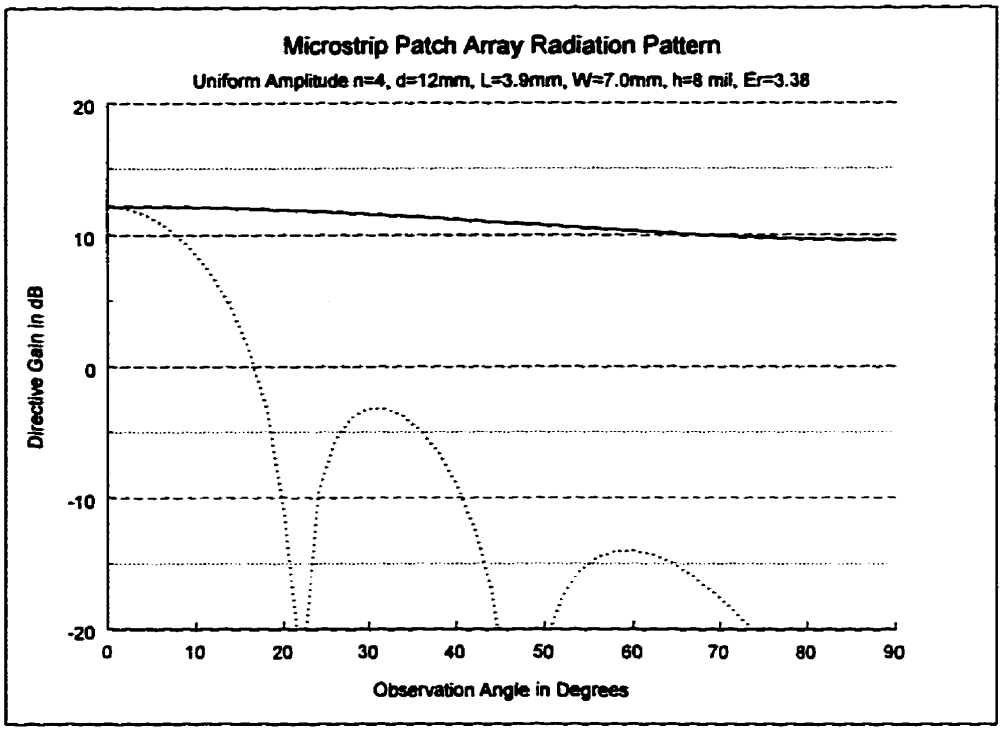

Figure 3.9 Azimuth pattern predicted for 4-element uniform linear MPA

These patterns for the elevation and azimuth planes were acceptable in the sense that the beamwidthes were as desired. Better side lode control is required which will be addressed using a non-uniform amplitude distribution presented in the next section.

3.4.3 Non-Uniform Amplitude Linear Array Factor

A related linear array is the non-uniform amplitude array that uses the same inter-element spacing but uses an excitation amplitude distribution along the array elements. The uniform array of the previous section is known to provide a narrower half power beamwidth $HPBW$ than a similar non-uniform amplitude array [6]. A non-uniform array is preferred when low side lobe levels are a design concern, as uniform arrays do not usually meet the specifications for this characteristic. The array factor for a non-uniform linear array varies slightly for an even or odd number of elements. An even numbered

array will be developed first with the odd numbered array right after it.

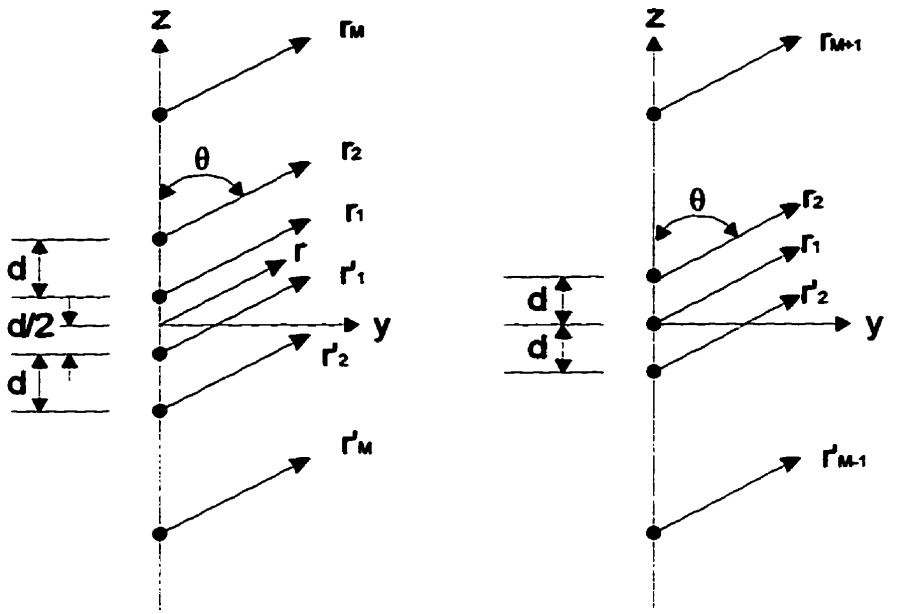

(a) Even number of elements 2M (b) Odd number of elements 2M+

Figure 3.10 Even and odd number of elements in non-uniform linear arrays

In the case of an even number of elements, the array factor for a symmetrical amplitude distribution is [6]

$$(AF)_{2M} = a_1 e^{j\left[\frac{1}{2}\right]kd\cos\theta} + a_2 e^{j\left[\frac{3}{2}\right]kd\cos\theta} + \ldots$$
$$\ldots + a_M e^{j\left[\frac{2M-1}{2}\right]kd\cos\theta} + a_M e^{-j\left[\frac{2M-1}{2}\right]kd\cos\theta} \qquad (3.81)$$
$$\ldots + a_1 e^{-j\left[\frac{1}{2}\right]kd\cos\theta} + a_2 e^{-j\left[\frac{3}{2}\right]kd\cos\theta} + \ldots$$

$$(AF)_{2M} = 2 \cdot \sum_{n=1}^{M} a_n \cos\left[\frac{(2n-1)}{2} kd\cos\theta\right] \qquad (3.82)$$

normalized [6]

$$(AF)_{2M} = \sum_{n=1}^{M} a_n \cos\left[\frac{(2n-1)}{2} kd\cos\theta\right] \tag{3.83}$$

$$(AF)_{2M} = \sum_{n=1}^{M} a_n \cos\left[\frac{(2n-1)}{2} u\right] \tag{3.84}$$

where

<u>array along x-axis,</u>

$$u = kd\sin\theta\cos\phi \tag{3.85}$$

<u>array along y-axis,</u>

$$u = kd\sin\theta\sin\phi \tag{3.86}$$

<u>array along z-axis,</u>

$$u = kd\cos\theta \tag{3.87}$$

The equation in (3.84) will be used along with (3.85) for the elevation array, and with (3.86) for the azimuth array. When an odd number of elements is to used in an array the array factor used is [6]

$$\begin{aligned}(AF)_{2M+1} = {} & 2a_1 + a_2 e^{jkd\cos\theta} + a_3 e^{j2kd\cos\theta} + \ldots \\ & \ldots + a_{M+1} e^{j2Mkd\cos\theta} + a_{M+1} e^{-j2Mkd\cos\theta} \\ & \ldots + a_2 e^{-jkd\cos\theta} + a_3 e^{-j2kd\cos\theta} + \ldots\end{aligned} \tag{3.88}$$

$$(AF)_{2M+1} = 2 \cdot \sum_{n=1}^{M} a_n \cos[2(n-1)kd\cos\theta] \tag{3.89}$$

Normalizing and using the same substitution as for the even number of elements case

$$(AF)_{2M+1} = \sum_{n=1}^{M} a_n \cos[2(n-1)u] \tag{3.90}$$

The equations in (3.84) and (3.90) may be used but an amplitude distribution is required to obtain some unique array property. Some amplitude distributions achieve low side lobes at the expense of a slightly broadened $HPBW$. In the next section a Taylor Line source distribution will be presented that provides good side lobe control without appreciably increasing the beamwidth. The non-uniform linear array radiation patterns obtain using the Taylor distribution will be included later in that section.

3.4.4 Taylor Line Source Amplitude Distribution

The Taylor line source distribution was originally presented in a classic paper [51] on the synthesis of equal side lobe patterns. Using a continuous line source current distribution that satisfied the same criteria as Chebyshev's linear array distribution, Taylor showed that although the ideal pattern was not physically realizable he could approximate it fairly closely using functions based on the two parameters $\bar{n}$ and A. The pattern derived by Taylor has the first $\bar{n}$ side lobes at some desired level and all side lobes beyond this fall off at $\frac{\sin(\pi z)}{\pi z}$ for $z = L\frac{u}{\lambda}$, where L is the length of the array. The synthesized pattern normalized to unity is given as [6,52]

$$F(z, A, \bar{n}) = \frac{\sin(\pi z)}{\pi z} \cdot \prod_{n=1}^{\bar{n}-1} \frac{1 - \frac{z^2}{z_n^2}}{1 - \frac{z^2}{n^2}} \tag{3.91}$$

where z_n are the null locations for the first $\bar{n}$ side lobes obtained using

$$z_n = \begin{cases} \pm\pi\sigma\sqrt{A^2 + \left[n - \frac{1}{2}\right]^2} & 1 \le n < \bar{n} \\ \pm n\pi & \bar{n} \le n < \infty \end{cases} \tag{3.92}$$

The variable σ is a smoothing variable to blend the first $\bar{n}$ side lobes with the remaining outer side lobes. This parameter is defined as,

$$\sigma = \frac{\bar{n}}{\sqrt{A^2 + \left[n - \frac{1}{2}\right]^2}} \tag{3.93}$$

The parameter A is related to the desired side lobe level using

$$A = \frac{1}{\pi} \cdot \operatorname{acosh} R_o \tag{3.94}$$

where R_o is the side lobe ratio obtained from

$$R_o = 10^{\left|\frac{SLL}{20}\right|} \tag{3.95}$$

The parameter $\bar{n}$ is selected by the designer with some specific selection guidelines [6,52]. Small values of $\bar{n}$ produce source distributions that are maximum at the center and monotonically decrease towards the edges. While large values of $\bar{n}$ results in source distributions that are peaked in the center and again at the ends of the array. It is recom-

mended that very small and very large values for $\bar{n}$ be avoided. As a rule of thumb this parameter is usually selected to be at least 3 for arrays with -25dB SLL and at least 6 for -40dB SLL [6,52].

The normalized current distribution that produces the desired pattern is defined by [6,52]

$$I(x') = \frac{1}{L}\left[1 + 2\sum_{p=1}^{\bar{n}-1} SF(p, A, \bar{n}) \cdot \cos\left[2\pi\frac{x'}{L}\right]\right] \tag{3.96}$$

Where $SF(p, A, \bar{n})$ is the approximation to the desired space factor defined by [6,52]

$$SF(p, A, \bar{n}) = \frac{[(\bar{n}-1)!]^2}{((\bar{n}-1+p)!(\bar{n}-1-p)!)} \cdot \prod_{m=1}^{\bar{n}-1}\left[1 - \left[\frac{\pi p}{z_n}\right]^2\right] \qquad |p| < \bar{n}$$
$$0 \qquad |p| \geq \bar{n} \tag{3.97}$$

There is an equation available to predict what the $HPBW$ for this type of array approximated will be:

$$\Theta_o = 2\,\text{asin}\left[\frac{\lambda\sigma}{\pi L}\left[(\text{acosh}\,R_o)^2 - \left[\text{acosh}\frac{R_o}{\sqrt{2}}\right]^2\right]^{\frac{1}{2}}\right] \tag{3.98}$$

The radiation patterns obtained for the elevation and azimuth linear arrays using the Taylor line source distribution with the non-uniform array factor are included in Figure 3.11 and Figure 3.12.

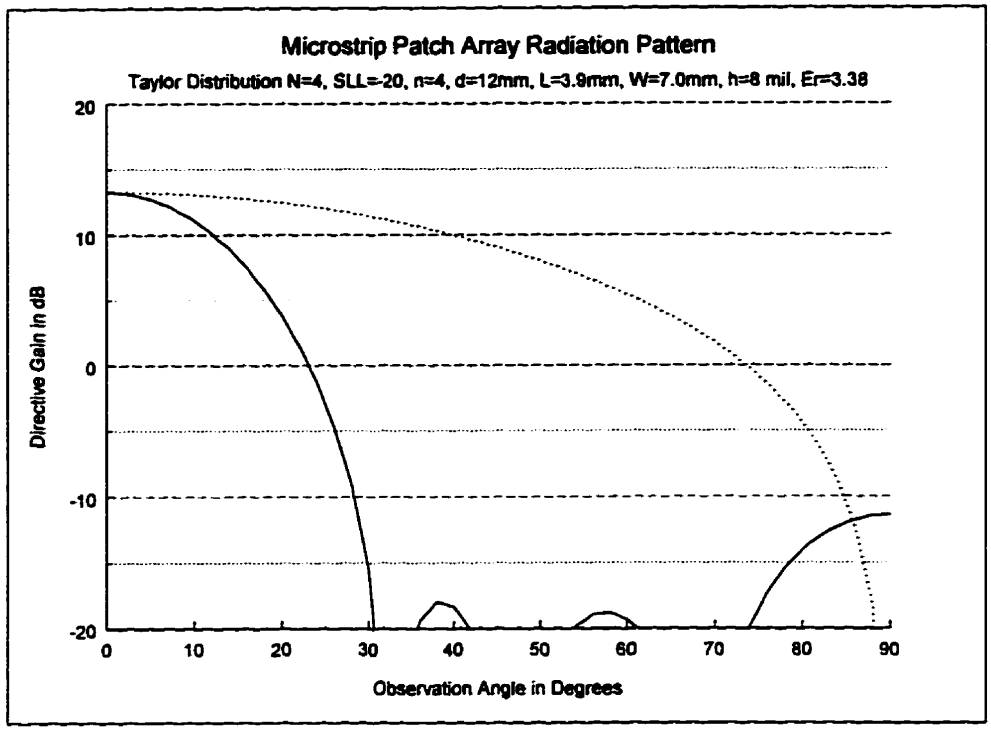

Figure 3.11 Taylor distribution elevation array pattern for N=4, d=12mm

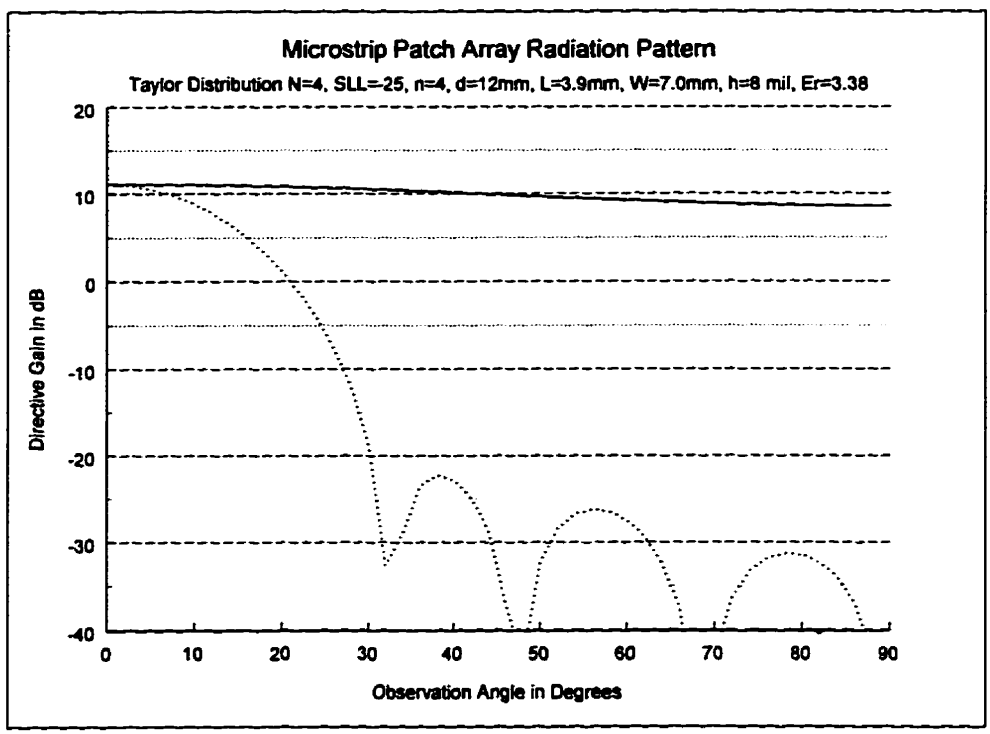

Figure 3.12 Taylor distribution azimuth array pattern for M=4, d=12mm

The predicted radiation patterns for the elevation and azimuth linear arrays meet the prescribed specifications. These linear arrays will be used to develop a planar array.

3.4.5 Planar Array Factor

Planar arrays are the most frequently designed form of microstrip array designed in industry. The reasons for this is simply better performance due to more control parameters that the designer can utilize to produce symmetrical patterns with lower side lobes. When used in a phased array, a planar array is able to scan to any point in space and is not restricted to a single plane of scanning. The antenna design pursued in this thesis will be a rectangular planar array whose radiation pattern is predicted as the product of the elevation and azimuth linear arrays [6]. The planar array factor in [6] is given as

$$AF(\theta,\phi) = AF_{EPlane}(\theta,\phi)\cdot AF_{HPlane}(\theta,\phi) \tag{3.99}$$

where $AF_{EPlane}(\theta,\phi)$ and $AF_{HPlane}(\theta,\phi)$ are either uniform or non-uniform linear array factors defined earlier in this chapter.

The directivity of an antenna is frequently expressed in terms of a closed form expression. If the array is assumed to only produce a major lobe and all side lobes neglected, the directivity is determined using [63]

$$Do \approx \frac{4\pi}{HPBW_E \cdot HPBW_H} \approx \frac{41000}{HPBW_E^{\circ} \cdot HPBW_H^{\circ}} \tag{3.100}$$

This equation is improved with the introduction of two correction factors, ε_M for beam efficiency, and k_p for pattern factor. These factors are introduced into (3.100) as follows:

$$Do \approx \frac{41000 \cdot \varepsilon_M}{k_p \cdot HPBW_E^{\circ} \cdot HPBW_H^{\circ}} \tag{3.101}$$

The beam efficiency, ε_M is a factor less than 1and usually in the range

$$\varepsilon_M = 0.75 \pm 0.15 \tag{3.102}$$

The pattern factor, k_p is 1 for uniform aperture field distributions, and may be slightly larger or less than 1 depending on the field distribution present [63].

A frequently used approximation used for directivity of planar arrays that includes these correction factor terms in its numerator is [6]

$$D_0 = \frac{32400}{HPBW_{EPlane} \cdot HPBW_{HPlane}} \tag{3.103}$$

CHAPTER 4: Design

4.1 General

4.1.1 Antenna Design and Fabrication

The standard procedure for antenna design starts with some pre-determined performance specifications the antenna is to meet. Based on these specifications, all the possible antenna configurations capable of meeting these requirement are evaluated, with their advantages and disadvantages detailed, and the most suitable configuration selected. When the antenna configuration is determined, preliminary design work continues with selection of a microwave laminate. This process is also performed by evaluating all potential laminate alternatives. A selection is made with equal emphasis on performance and manufacturability. Based on the results from these studies, an aperture fed patch with coplanar parasitic element design is to be pursued and be produced on Rogers RO4003 laminate material. This concludes the preliminary design work and provides the framework for the design of the radiating antenna element and the antenna array. This section includes topics common to both the antenna element and the array design, the two sections following discuss the antenna requirements unique to each design.

Circuit Specification: The antenna feed for both the single element, and the array, is required to provide a transfer of power from a 50 ohm coaxial source, to the radiating antenna element or elements. This requires a feed circuit well matched to the source to minimize the amount of power reflected back and not transferred to the radiators. The laminate selected has a higher dielectric loss factor than traditional PTFE laminates frequently used at higher frequencies. To minimize feedline radiation losses, all changes in line direction will use circular radius bends [14]. The feed circuitry is to be designed for a center frequency of 17GHz and will be required to perform acceptably over the entire specified operating band.

The output ports of this feed circuit will be 50 ohms, as the antenna elements are to be designed for this impedance at a fixed point to allow for easy integration of the antenna elements into any subarray or array configuration. The design of the array feed has some extra amplitude and phase requirements discussed further in an array feed network section.

Substrate Material: The selection of a substrate material is an important design consideration for MIC's. Some of the concerns that a microwave circuit designer must consider are:

(1) dispersion

(2) conductor and dielectric losses

(3) surface waves

(4) substrate anisotropy

(5) substrate thermal expansion in x,y and z directions

(6) moisture absorption

(7) manufacturability

(8) material cost

(9) material consistency

(10) material availability

Dispersion and dielectric losses are of concern at higher frequencies like Ku-Band frequencies at which we are attempting to design. Although not ideal these effects are acceptable for the Rogers RO4003 material selected. The surface waves may be controlled with proper permittivity and substrate thickness selection. Substrate anisotropy may result in inconsistent circuit performance due to non-uniform permittivity in the x, y and z planes. The substrate thermal expansion coefficients are of concern for circuit board mounting where mechanical stresses and interactions can cause board failures in the field if not designed properly. Substrate moisture absorption is both a manufacturability and perfor-

mance concern as hydroscopic materials tend to retain moisture and are difficult to process. These materials also have performance variations that depend on the amount of moisture and humidity levels present at any given time, they are not recommended for use in any non-hermetically sealed circuits. Material availability is a manufacturing concern that can lead to lost production time should delivery times and volumes be inconsistent with a program's manufacturing requirements.

Manufacturability is the highest priority concern as standard PTFE circuits require specialized etching processing and special chemical preparation for plating. In general most PTFE board shops are relatively expensive when compared to FR4 board shops. Material cost is also a concern in the substrate selection process. The laminate industry has begun to understand that the PTFE laminates currently available are not easily fabricated in extremely high volumes and have begun developing new commercial grade microwave laminates. These new materials are FR4 like in their physical and fabrication characteristics, but have more PTFE like electrical properties. Since the initial introduction of Rogers RO4003 there have been two additional alternatives to this market, 25N was recently introduced by Arlon, and GML2000 by GIL. Material consistency from lot to lot is also important as some laminate producers do not have controls in place to produce large volumes of consistent, high performance laminates.

Based on the manufacturability and processing cost criteria Rogers RO4003 was selected. The RO4003 material was also selected because of its lower pricing in comparison to traditional PTFE products commonly used at microwave frequencies. It is hoped that FR4 printed circuit board fabricators will be able to process these circuits and the program realize huge price advantages over similar PTFE circuits.

Table 4.1 Rogers RO4003 Properties

Property	Specification
permittivity and tolerance @10GHz	3.38 +/- 0.05
loss tangent @ 10GHz	0.002
water absorbtion	0.06%
copper peel strength (pli)	4.5
coefficient of thermal expansion (ppm/C)	X=11 Y=14 Z=35
thermal coefficient of permittivity (ppm/C)	-30

4.1.2 Corporate Feed Network Design

The configuration selected for excitation of the antenna array elements is a corporate, or parallel, feed network. The excitation of a single element is relatively simple and was designed with considerations for easy integration into an array. Details on excitation of a single antenna element are included later as part of an element matching section. The advantages of corporate feeding are: it is possible to achieve a high degree of amplitude and phase control in two-dimensional planar arrays, and for broadside directed arrays it is easy to minimize frequency scanning in wideband applications with equal electrical line lengths to all elements.

The corporate feed circuit for this array will consist of a combination of simple microstrip circuits, specifically 3-way power splitters or T-junction circuits (actually Y-Shaped in these designs), quarter wave transformers, and radius bends. The power

splitter circuits to be used will have uniform and non-uniform split ratios. There is a limit on the physically realizable ratio of power directed to the high power and low power arms of a T-junction [17]. This limit is based on the line impedance limitations due to fabrication tolerances. In general the width of high impedance lines must be wider than 100um (or 0.004") to be easily realized repeatedly.

The array will be designed as the combination of two linear arrays, one for the desired azimuth radiation pattern and the other for the elevation pattern. The final antenna will be a planar array using a combination of these linear arrays. The resulting array distribution will be a two dimensional Taylor line source distribution for 25 dB side lobes, using a Taylor side lobe control number of n=4. The required Taylor line source distribution will be presented later. Once a feed network has been outlined, a fair amount of design work is required to meet the amplitude and phase requirements for the array in both the azimuth and elevation planes.

4.2 Single Antenna Element Design

4.2.1 Single Antenna Element Specifications

The design specifications for a single antenna element are:

(a) center operating frequency of 17 GHz

(b) back radiation 15dB down from broadside

(c) linear polarization (vertical)

(d) an operational bandwidth of better than 10% (with $|S_{11}| < -10dB$)

(e) the antenna should be matched to a 50 ohm system

The antenna specification that is to be meet is somewhat challenging, a low cost, easily produced in extremely large volume, microstrip antenna, with a better than 10% operating bandwidth. The antenna is to have a center frequency of 17GHz and a functioning band-

width between 16 and 18GHz. There is no specification for cross polarization level but symmetry will be used wherever possible to minimize this property [37].

4.2.2 Antenna Resonant Frequency

This antenna element design started with the goal of obtaining the desired center resonant frequency. The first design will be created using simple empirical design equations [41] to determine the resonant length for a simple microstripline fed antenna element. The laminate thickness selected is 0.8128mm (or 0.032") which is the thickest practical option available in this laminate family. These initial design approximations will then tested numerically using a commercial fullwave analysis MoM package (Ensemble). Using an iterative process with this software package the resonant frequency for this microstrip fed patch will be refined until the desired center frequency is obtained.

4.2.3 Bandwidth Enhancements

The bandwidth of the radiating element will be increased with the addition of two resonant strips to both non-resonant edges of the main patch element. These strips will be designed to resonant at a slightly lower frequency than the main patch to create a double-resonant structure. Both parasitic strips will be made the same length to produce a symmetric pattern in the H-Plane. The parameters available for optimization at this level of the design will be the main patch length and width, the parasitic strips length and width, and the spacing from the main patch. The effects of these parameters on the bandwidth obtained will be analyzed using the Ensemble software. Once a bandwidth close to the desired performance is obtained, the feed will be changed to an aperture feed to eliminate the feed line radiation seen in the microstrip patch broadside radiation pattern.

4.2.4 Aperture Coupled Microstrip Patch Antenna

With a simulated element resonant frequency and bandwidth close to the specified values, the antenna design will be changed to an aperture fed configuration to obtain the additional performance required to meet the design specifications. The aperture feed is initially started using a simple rectangular slot, following the procedures used in other published designs [15,16,23]. With an aperture feed configuration, the patch resonant length, aperture size, and open circuit stub lengths will be adjusted to obtain the desired center frequency. The level of aperture coupling to the patch will be varied by changing the aperture length. The degree of coupling is noted in a Smith Chart impedance plot of the antenna by the diameter of a "coupling loop" in the trace. If the antenna is well designed this loop will be centered and of sufficient size to cover the bandwidth required [32].

When acceptable coupling levels are obtained with a rectangular slot, the aperture shape will be changed to a H-Shaped slot using design curves produced by Cohn in [42] and used by Pozar [32]. The H-Shaped slot has a higher magnetic polarizability than a simple rectangular slot, and thus the length may be reduced by about a third to obtain the same coupling level as a rectangular slot. The advantage of using a smaller H-slot is that the effects of slot resonance and back radiation are reduced [32]. The H-slot is also preferred in terms of manufacturability as the maximum coupling location, or "sweet spot", is wider than that of a rectangular slot as detailed in plots in [32,42].

Aperture fed microstrip antennas have multiple parameters available for optimization they include, the slot aspect ratio of width to length, slot position relative to the antenna element, length of the tuning stub, substrate thickness from microstripline to aperture, substrate thickness from aperture to radiating patch elements. The first three parameters are adjusted freely but the last two parameters may be adjusted with the appropriate adjustment to the microstripline feed and the patch dimensions. Another parameter that may be varied is the impedance of the microstripline under the aperture, this parame-

ter has not been studied in published papers and is not investigated here.

The operating bandwidth may be adjusted with changes to the aperture size, slight adjustment or tweaking of the patch resonant lengths, and changes in the coupling gap between the main and parasitic patches. When the antenna element has the desired center frequency and bandwidth, the antenna will be matched, using a section of transmission line to move the impedance on the real axis of the Smith Chart, and a quarter wave transformer to obtain a 50 ohm system impedance.

4.2.5 Element Impedance Matching

The final design requires a matching circuit on the feedline to obtain the desired system impedance. Using a Smith Chart plot, this will be accomplished by assuming a reference plane at the plane of the slot, and moving towards the generator along a constant impedance line until a purely resistive position on the antenna input impedance plot is observed. At this location a quarter wave transformer is added and an acceptable antenna input impedance matching obtained (Appendix E). Experimental testing of this antenna element was performed using a test fixture and a coax to microstrip K-connector attached at the circuit board edge. The dimensions for a straight feedline antenna element are given in Figure 4.1.

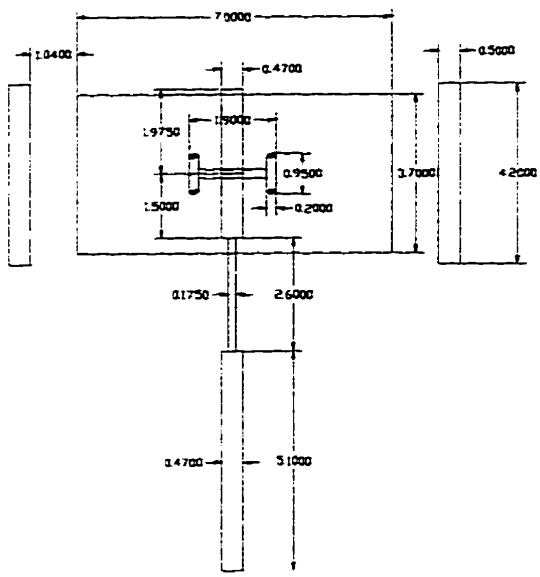

Figure 4.1 Diagram of radiating patch element

4.3 Array Design

4.3.1 Array Design Specifications

The design specifications for antenna array are:

(a) center operating frequency of 17 GHz

(b) a radiation pattern requirement of:

$HPBW_{elv}$ of 15-20 degrees

$HPBW_{az}$ of 20 degrees

Side Lobe Levels (SLL) of 15dB

(c) linear polarization (vertical)

(d) an operational bandwidth of better than 10% (with $|S_{11}| < -10dB$)

(e) impedance matched to a 50 ohm system

The first parameters attacked in this array design are the half power beamwidthes and side

lobe levels which are dependent on the inter-element spacing, amplitude weightings and phasing. These parameters control the radiation pattern that is required to meet the design performance specifications. The array is designed as the combination of two linear arrays, one for the desired azimuth radiation pattern and the other for elevation pattern. The final array is a direct combination of these linear arrays. The required linear arrays were determined using the radiation pattern program of Appendix-C and the Taylor distribution of Appendix-D. Both linear array designs obtained use a Taylor line source distributions for 25 dB side lobes, with a Taylor side lobe control number of n=4. An array feed circuit is then created based on these weightings and phasing requirements. The desired normalized amplitude distribution required for this 16-element (4x4) planar array is shown in Figure 4.2.

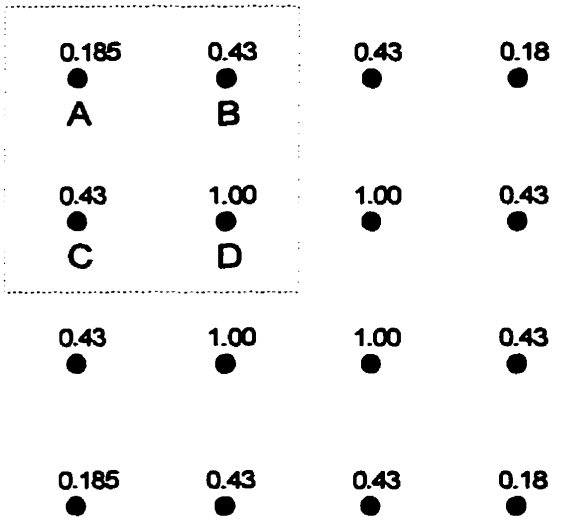

Figure 4.2 The desired planar amplitude distribution and symmetry cell

The above figure shows the desired array amplitude distribution. The specified subarray feed network is to be completely designed, and replicated for the other three subarray cells. In the complete array there will be four subarrays connected with 3dB power dividers. The desired radiation pattern has a broadside beam so all elements are to be kept in phase.

4.3.2 Array Amplitude and Phase Distribution

A feed network design is required to produce the amplitude and phase values determined in the previous section. The design of this network starts with a large amount of preliminary design work to determine the amplitude levels required throughout the feed circuit. The preliminary work begins with a translation of the array amplitude weightings into the required power levels at each output port. These power levels were then used to create power splitters with physically realizable split ratios throughout the corporate feed network.

The empirical calculation of the feed network power splitters was programmed in the mathematical software package Mathcad (see Appendix-F) for quick iterative solutions when line impedances were changed. The numerical solution obtained for the power levels to the elements in the subarray denoted in Figure 4.2 as A,B,C and D were A= -10.44 dB, B= -6.77 dB, C= -6.77 dB and D= -3.1 dB. These values were referred to as the lossless ideal power levels. The elements A and B will be connected with one splitter, and elements C and D with another splitter. The input of the AB and CD splitters is also to be connected using another splitter referred to as ABCD. Four groupings of these subarrays are to be connected using 3dB power splitters to realize the entire 16 element array. To determine the required power levels in the full array, the lossless ideal power levels for elements A to D are decreased by another 6 dB and are required to be A= -16.44 dB, B= -12.77 dB, C= -12.77 dB, and D= -9.1 dB. The subarray configuration is given in Figure 4.3 while all dimensions are provided in Appendix-H.

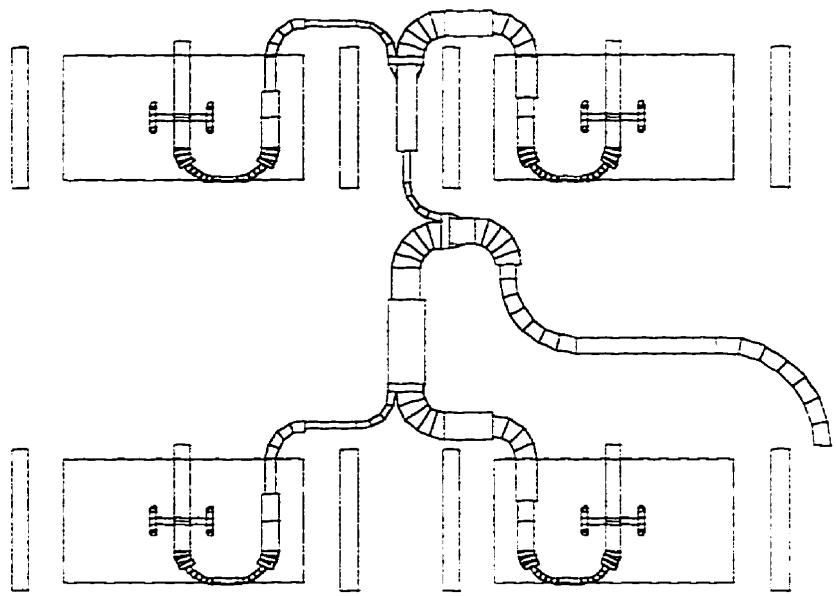

Figure 4.3 4-element subarray with proper amplitude and phasing

4.4 Corporate Feed Design

4.4.1 General

The array feed method selected is a corporate feed for two main reasons. The first reason is that a corporate feed is able to provide control of the array amplitude distribution in both elevation and azimuth planes. The second reason is that the electrical length to each antenna element is required to be identical to prevent frequency scanning, which is possible with this type of feed network. The final array design is to be a 16-element array using 4-element subarray groupings (see Figure 4.3). These subarrays are to be connected with three 3dB power splitters, to realize the full array.

To minimize the feed circuit losses, the array feed design uses radius bends throughout the network [14]. Even the power splitters are designed with swept radius bends and formed into a Y-Junction instead of the normal T-Junctions usually used. In the effort to produce a compact feed circuit and adhere to the radius curved design, the ele-

ment feed line is changed to a swept radius bend as shown in Figure 4.3. To maintain the same degree of impedance match some minor antenna element modifications are required that were determined using the Ensemble MoM package. This new swept radius feed requires that the aperture length be decreased to $L_{ap} = 1.85mm$ and the tuning stub at the end of the feed line be increased to $L_{stub} = 2.275mm$ (see Appendix-H).

4.4.2 Subarray Feed Network Design

The subarray circuit design requires the design of a passive transmission line network comprised of power dividers, quarter wave transformers and radius bends. The transmission lines may be routed in any desired fashion as long as they do not come within a few line widthes of each other. This should reduce the degree of undesirable coupling between parallel lines. The change of line direction will be performed with radius bends that are of sufficient radius to introduce a minimal effect on the line. In [64] it was stated that for radius bend of $R \geq 4.0h$, the introduced effect will produce a $VSWR < 1.05$.

Once the arm impedances for the power splitters are determined (see Appendix-F), the circuits are created using a transmission line model to determine the required line widthes for a desired arm impedance. The power divider output arms act like parallel lines and appear at the junction as an equivalent impedance, determined using

$$Z_{eq} = \frac{1}{\frac{1}{R_a} + \frac{1}{R_b}} \tag{3.99}$$

where Z_{eq} is the equivalent impedance presented at the junction, R_a and R_b are the output line impedances. This equivalent junction impedance is then transformed to the required input impedance with a quarter wave transformer, determined using

$$Z_{TX} = \sqrt{Z_{eq} \cdot Z_{in}} \tag{3.100}$$

where Z_{TX} is the required transformer impedance, and Z_{in} is the power splitter input impedance.

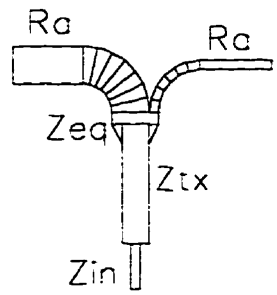

Figure 4.4 Details of a power splitter

After an initial paper design all circuits will be analyzed numerically using the MoM software IE3D to determine power split ratios expected, and refine the arm impedances as necessary. The MoM analysis is performed on the entire feed network on a block by block basis to assure proper power split ratios down to each element.

The original amplitude distribution weightings are used to obtain initial target values for the splitter output arms. The power at each output port is added and the efficiency of the power splitter determined. This efficiency number is both a figure of merit for a splitter design, and useful later when the ideal lossy power split is required for verification of the simulated feed network performance. Using the Y-Junction splitter configuration the simulated power splitters were 95% efficient, or produced about a 0.22dB loss. The initial lossless target power levels at each arm were adjusted with the efficiency number, and new lossy power target levels obtained (Appendix-F).

The individual splitters are then connected together to form the complete subarray and the power at each port compared to the lossy ideal number (Appendix-F). This was an iterative process until acceptable power levels were obtained at all ports of the feed circuit.

4.4.3 Full Array Feed Network Design

When an acceptable subarray design is obtained, the subarray is then connected to two 3dB power splitters to create the full array feed circuit. This circuit's power levels were also compared to the lossy ideal levels for acceptable values. The full array is shown in Figure 4.4 with all dimensions given in Appendix-H.

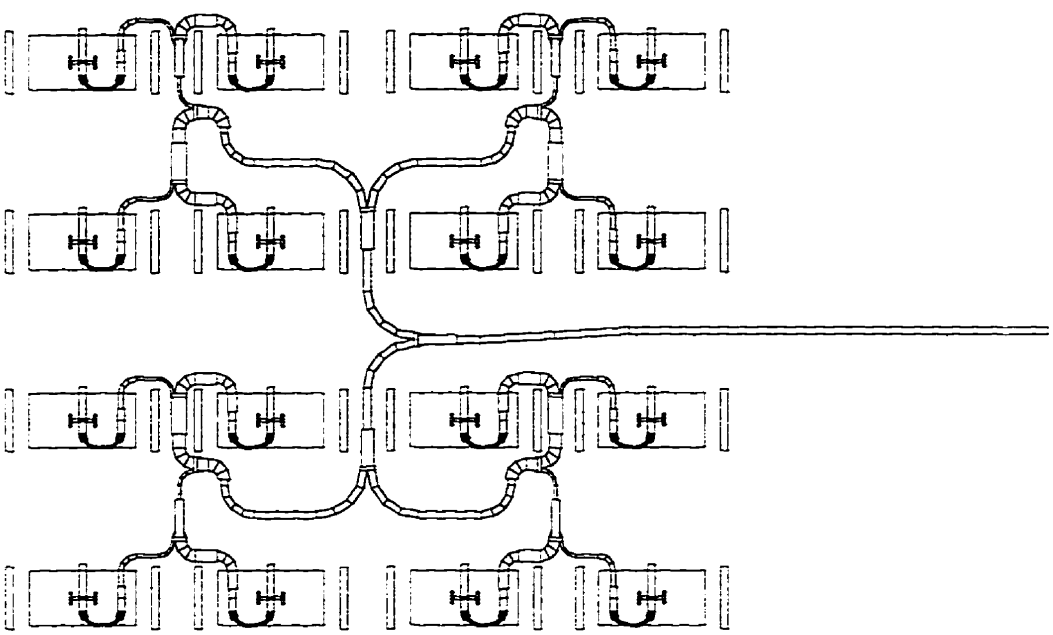

Figure 4.5 A Ku-Band 16-element microstrip array

The array feed circuit is created as a 17-port circuit with all ports terminated in the same impedance. The simulated data obtained for the circuit is then stored as a 17-port device, an s-parameter file. The antenna element is simulated separately on Ensemble and the impedance information stored as a 1-port s-parameter file. A linear simulator is included in the IE3D package and is used to determine the overall array impedance. The feed circuit obtained with IE3D is shown in Figure 4.5. The simulated results for the phase and amplitude of the full array feed network obtained from IE3D are included in Appendix-G.

4.5 Radome Design

4.5.1 Radome Performance Specifications

The radome for this antenna is required to protect the antenna from damage in the harsh automotive environment with minimum degradation of antenna performance. The radome must withstand vibration, extreme high and low temperature cycling, exposure to petroleum based fluids, it must be waterproof, and mechanically strong enough to withstand bumps and knocks from flying stones and other debris. The radome is required to have a minimal effect on the antenna impedance matching and have very low radiation losses.

4.5.2 Radome Configuration

The design of single walled radomes may be divided into two main groupings, thin walled radomes and thick walled radomes [64]. The thin walled design requires a radome protective layer that is usually less than $\frac{\lambda}{10}$, which for this application is too thin to provide sufficient protection. By elimination, a thick walled radome is to be used. The required radome thickness is to be determined using [64],

$$d = \frac{n\lambda}{2\sqrt{(\varepsilon_r - \sin(\theta)^2)}} \tag{4.1}$$

Where n is an integer, λ the free space wavelength, ε_r the effective radome material permittivity, and θ the angle of incidence.

The antenna radome configuration chosen was a half wavelength thick single walled ULTEM. ULTEM is a thermoplastic polyethermide from General Electric with excellent mechanical properties. Its electrical properties are specified as a dielectric constant of roughly $\varepsilon_r = 3.5$ and a dielectric loss tangent of roughly $\tan\delta = 0.005$. Using (4.1), the empricial design for this radome requires the determination of the radome thick-

ness. An estimate for the ULTEM effective permittivity at 17GHz was required as the supplied information stopped at 10GHz. The estimated value used is, $\varepsilon_{r_{eff}} = 2.85$. Using this effective permittivity a thickness of 5.2mm (or 0.205") was desired. The required spacing between the radome and the antenna surface is of yet unknown but a half wavelength will be used as an initial spacing. A half wavelength spacing was anticipated to provide the minimum transmission loss as the reflections off the inner radome surface should add in phase with the next wave front off the antenna surface. The free space half wavelength used is 8.81mm (or 0.350").

CHAPTER 5: Experimental Results

5.1 Single Element

5.1.1 Physical Dimensions and Laminate Properties

The experimental testing of the antenna array started with a verification of the element design. These antennas are fabricated on the RO4003 series of laminates. The core thickness used for the feed circuit is 203.2um (0.008"), and the patch radiators on a 812.8um (0.032") core. The dielectric constant for RO4003 is stated to be $\varepsilon_r = 3.38$ and the dielectric loss tangent, $\tan\delta = 0.005$. These two substrates will be bonded together with an ARLON 6700 bonding film, 38um (0.0015") thick, with a dielectric constant of $\varepsilon_r = 2.35$, and a dielectric loss tangent of $\tan\delta = 0.0025$. Included below are all relevant patch dimensions, these dimensions are included in Figure 4.1.

The dimensions of the microstrip patch antenna element are as follows:

Main patch width $W_d = 7.0mm$
Main patch resonant length $L_d = 3.70mm$
Parasitic patch width $W_p = 0.5mm$
Parasitic patch resonant length $L_p = 4.20mm$
H-plane gap between main and parasitic patches $S_y = 1.04mm$
Coupling aperture width $W_{ap} = 0.2mm$
Coupling aperture length $L_{ap} = 1.90mm$
The vertical arms of the H-slot are $\frac{L_{ap}}{2} = 0.95mm$

The feed line to the aperture dimensions are as follows:

The 50 ohm feed line was $W_{50} = 0.47mm$
The matching stub beyond the slot was $L_{stub} = 1.975mm$
The line length from the aperture to the transformer, $L_1 = 1.50mm$
The matching transformer was 8.54 ohms and $W_{85.4} = 0.175mm$
The transformer length was $L_{85.4} = 2.60mm$

A 50 ohm feedline is connected with a microstrip to coaxial cable tab K-connector at the edge of the board for test measurements. The final design will have no microwave connectors as the entire transceiver will be located on the feed circuit layer.

5.1.2 Resonant Frequency

Antenna resonance and impedance measurements are performed on a Hewlett Packard 8510C vector network analyzer (VNA). Before any measurements are performed, the VNA is calibrated for one port measurements. The calibration process involves the measurement of a set of calibration test standards (a 50 ohm matched load, a short, and an open). The VNA then uses these calibration measurements to numerically set the reference plane for the measurements at the end of the VNA system coaxial cables. This effectively removes the effects of all cabling upto this point.

The VNA is able to collect both amplitude and phase information on the signal reflected back from the device under test (DUT). The magnitude of the reflected signal is used to determine the DUT return loss. When both the reflected amplitude and phase information are used, the system is able to produce information on the complex impedance of the DUT and conveniently plots it using a Smith Chart.

The measurement trace in Figure 5.1 shows the double resonance of the single antenna element. The main patch being shorter is the resonance seen in the -33.9dB dip at 17.26GHz. The longer parasitic patch elements are resonant at 16.58GHz as noted by a -34.5dB dip in the reflection magnitude. The close proximity of these resonances produces the wide bandwidth desired.

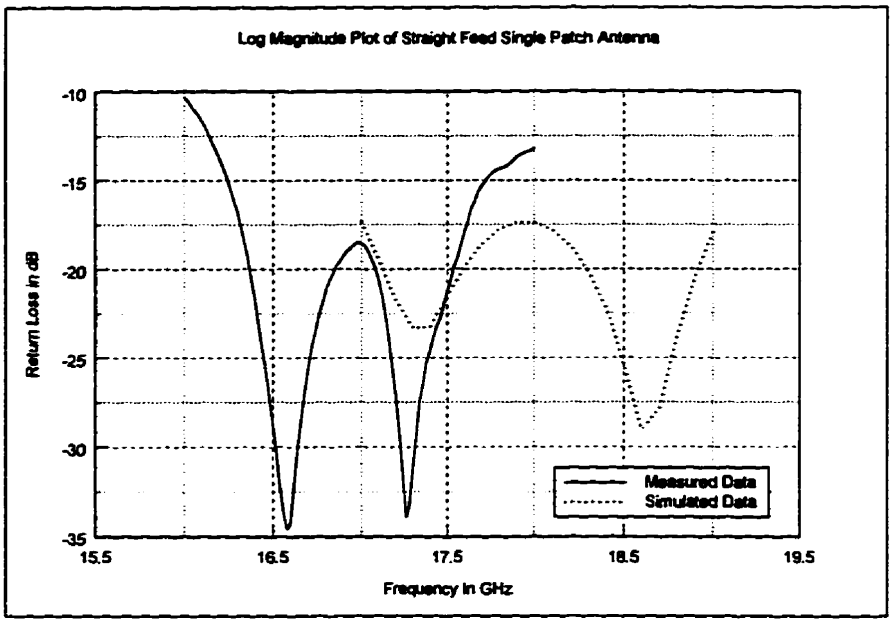

Figure 5.1 Return loss log magnitude plot for a single antenna element

The dimensions used for the fabricated experimental element were determined using the commercial MoM package Ensemble. This designer is quite familiar with the results obtained using this package and compensated for the 5-7% shift down in frequency from simulated to realized experimental results. The simulation results are included with the measured results in Figure 5.1. The simulated data trace shows a double resonance, but these resonances are at 18.6GHz (with a -29dB dip) for the main patch, and for the parasitic patches, at 17.3GHz (referring to the -23dB notch).

5.1.3 Input Impedance

The input impedance measurement is an important parameter used by most antenna designers. The complex antenna impedance is usually displayed in polar form as a Smith Chart plot. The input impedance is used extensively in the design of this antenna element as the level of coupling is clearly noted on the Smith Chart as a loop [32]. The antenna is over-coupled when a large coupling loop is noted, and under-coupled when a small coupling loop (or no loop) is seen. The optimum loop size depends on the bandwidth and match level desired.

As mentioned, the design verification of this element was performed using the Ensemble MoM software package. The input impedance obtained with this tool is shown in Figure 5.2. The plot shows a good sized coupling loop and is well placed for optimum bandwidth for this design.

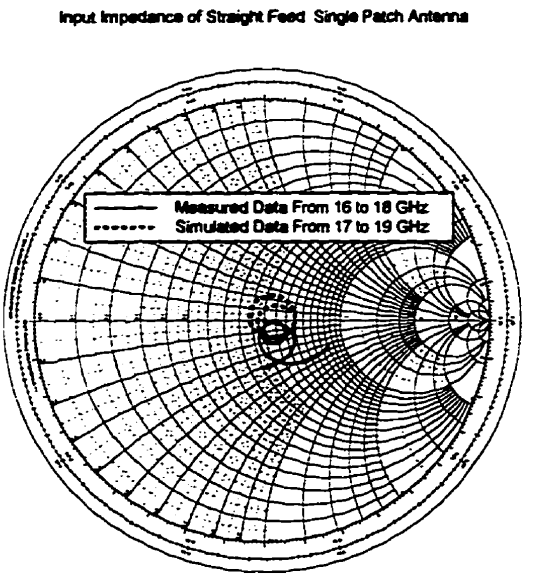

Figure 5.2 Smith Chart input impedance plots for a single antenna element

The measured input impedance is also shown in Figure 5.2 and the two traces agree quite well. There is a small discrepancy between the plotted data which might be attributed to the bonding film that is not included in the antenna model simulated. Another possible source of error is the 50um (0.002") etch resolutions obtained with current processing

equipment. The required layer to layer registration for this circuit is yet another possible source of error due to any slight misalignment. The effects of the K-connector used to connect the antenna to VNA coaxial cable is also not accounted for and could contribute to the discrepancy noticed.

5.1.4 Bandwidth

A very important design specification for this antenna is the operating bandwidth. The bandwidth, for this antenna is determined using the microstrip patch impedance bandwidth, including the feed matching circui, and the antennas radiation properties over the specified frequency range. The useful impedance bandwidth is defined by the antenna return loss, which is the range where the match was better than -10 dB. Looking back at Figure 5.1, the acceptable impedance bandwidth extends over the entire measured range from 16 to 18 GHz. This bandwidth referenced to the center frequency of 17GHz equates to better than a 11.75% bandwidth. This bandwidth was deemed acceptable as the required operating bandwidth is from 16.25GHz to 17.75GHz or 8.8%. The measurements of the radiation pattern did not show a noticeable variation across this bandwidth so the impedance was deemed to be the bandwidth limiting factor.

The simulated results for this antenna element showed a bandwidth considerably wider than the 17 to 19GHz bandwidth simulated as the return loss at these band edges was -17dB. As mentioned previously, the simulated results are performed over a slightly higher operating frequency, to compensate for the shift down in measured data, seen previously by the author on other designs produced with Ensemble.

5.1.5 Radiation Properties

The antenna radiation pattern measurements were performed in an anechoic chamber at HE Microwave. The data is collected automatically using an in house labview data collection program. The far-field region of an antenna is commonly specified as beginning at $\frac{2D^2}{\lambda_o}$ [6]: this requirement is meet for the following measurements presented. The procedure used collect this information is to first calibrate the anechoic chamber test measurement equipment using a standard gain horn antenna with known broadside gain characteristics across the frequency band of interest. The calibration horn is then replaced with our antennas under test (AUT) and gain measurements performed in the two principle planes (E-Plane and H-Plane).

The single patch antenna elements were fabricated on 4.45cm x 4.45 cm (3.5"x3.5") circuits. These circuit dimension were dictated by the allocated area for the antenna in the final product. The small ground plane produced with this board size is responsible for the edge diffraction effects [61] seen in the E-plane measurements, as shown in Figure 5.3. The pattern would have been cleaner had a larger ground plane circuit been used, but the purpose of the element design is to prove that the element did in fact radiate before creation of an array.

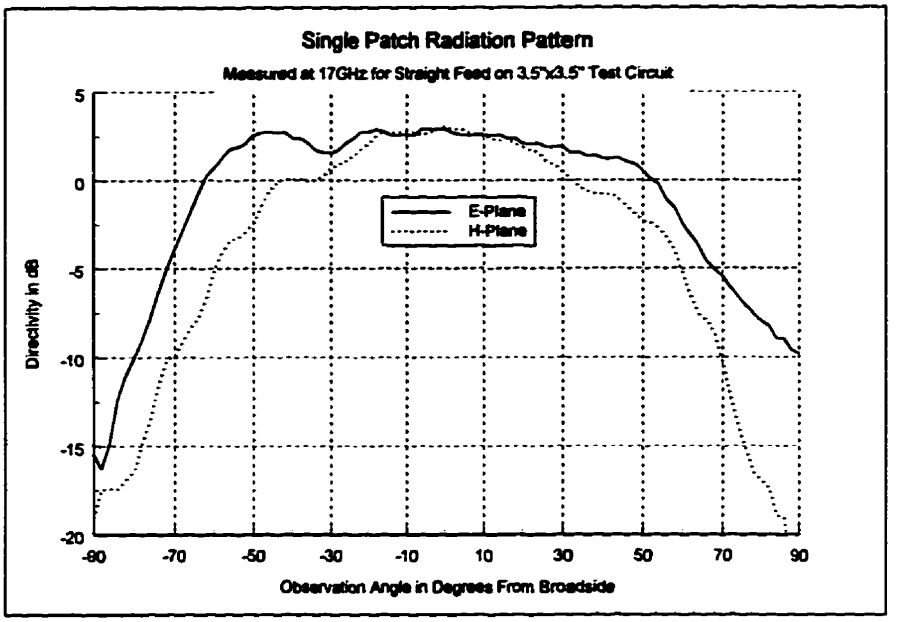

Figure 5.3 Measured radiation pattern for a patch antenna element

The simulated radiation pattern for this element from Ensemble shows the same form as the measured data (without the finite ground plane ripple).

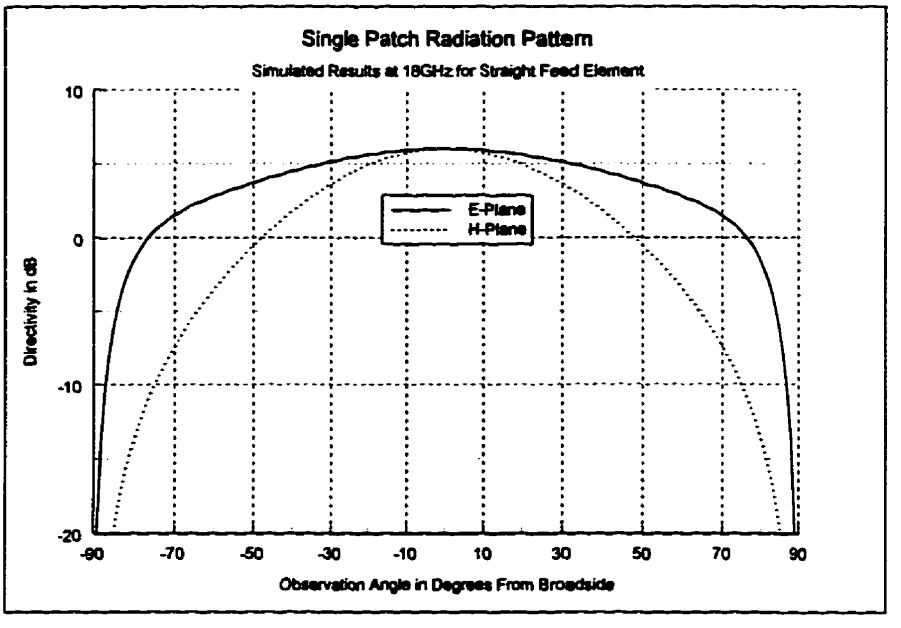

Figure 5.4 Simulated element radiation pattern

5.1.6 Directivity

The directivity of an antenna is a measure of an antenna's ability to receive or transmit energy in a certain direction. This measurement is usually defined as the ratio of the maximum radiation intensity of the tested antenna divided by the expected radiation intensity of an isotropic radiator. There is no easy means of determining the directivity so a closed form empirical approximation is used. The widely used approximation of Balanis [6] uses the half power beamwidthes (HPBW) of the two principle planes.

$$D_0 = \frac{32400}{\theta_E \theta_H} \tag{5.1}$$

Where the E-Plane half power beamwidthes is θ_E, and the H-Plane θ_H. The ripples in the measured radiation data makes the determination of the element HPBW difficult but values were extracted from the measured data as is. The E-Plane HPBW is measured to be $\theta_E = 115.66$ and the H-Plane HPBW $\theta_H = 74$. The directivity is calculated to be $D_0 = 3.79$ in linear units or $D_o = 5.78$ dB.

5.1.7 Gain

The gain characteristics of an antenna is a measurable quantity that usually determines if an antennas performance is acceptable. The standard procedure used is to calibrate the antenna measurement equipment, by measuring a known gain reference antenna and referring the AUT measured data to these values. The gain is analytically expressed as the product of the antenna directivity and the antenna efficiency [6].

$$G = e_t D_o \tag{5.2}$$

The efficiency factor is a number less than unity that accounts for the losses present when compared to the analytic expression for directivity. The measured gain of this antenna had

a slight discrepancy between the E and H-Plane values. The E-Plane produced a measured gain of 2.9dB and the H-Plane 3.07dB. The higher of these two values is used for all calculations. Before this gain value is used the reference plane is moved to the feed line directly below the aperture. This is accomplished by artificially adding back the transmission line losses. The transmission line losses were determined using the VNA to measure the insertion loss for various lengths of 50 ohm transmission line. The experimental results determined the insertion loss to be about 0.295dB/cm (or 0.75dB/inch). The single patch had roughly 4.45cm (1.75") of line length from the edge of the board to the desired reference location under the slot. Using this dimension it is determined that 1.31dB should be added to account for the losses over this length of transmission line. The gain for the reference plane adjusted antenna is

$$G = 4.38 \text{ dB} \tag{5.3}$$

or in linear units,

$$G = 2.74 \tag{5.4}$$

5.1.8 Efficiency

The antenna efficiency is a factor used to account for all losses experienced. There are three mechanisms for loss in this antenna. The antenna will experience a mismatch loss e_r if the antenna is not well matched to the feed circuit. The largest source of antenna loss are usually the conductor and dielectric losses e_{cd} which are usually measured together and are presented here as a single term. The total antenna efficiency is the product of these terms [6]:

$$e_t = e_r e_{cd} \tag{5.5}$$

The antenna return loss is used to determine the reflection coefficient [6].

$$S_{11} = 10\log(|\Gamma|) \tag{5.6}$$

The return loss measured at the center frequency is -18.6dB. Using (5.6) the reflection coefficient is determined as $|\Gamma| = 0.014$. The mismatch efficiency is determined using [6],

$$e_r = 1 - |\Gamma|^2 \tag{5.7}$$

For this antenna the mismatch efficiency is $e_r = 0.9998$ which is close enough to unity to be considered 1. The overall antenna efficiency is then determined using the ratio of realized gain to the expected directivity from the approximating equation (5.1). The antenna efficiency is

$$e_t = \frac{G}{D_o} = \frac{2.74}{3.79} = 0.722 \tag{5.8}$$

This number will be used in the calculation of array efficiency later in the antenna array section.

5.2 Antenna Array

5.2.1 Physical Dimensions

The single antenna element of the previous section, with slight modifications (see Appendix-H), is used to create a 16-element array in a 4x4 configuration. There are too many array dimensions to list here but all dimensions are included in Appendix-H in exploded views.

5.2.2 Resonant Frequency

The antenna array resonant frequency is measured using a VNA and plotted in a log magnitude format. In Figure 5.5 a double resonance may be seen with a lower resonance at 16.6GHz but the second higher resonance seems to have flattened out and is less prominent. The measured circuit showed the same downward frequency shift of around 5-7% when compared to the MoM design results using IE3D.

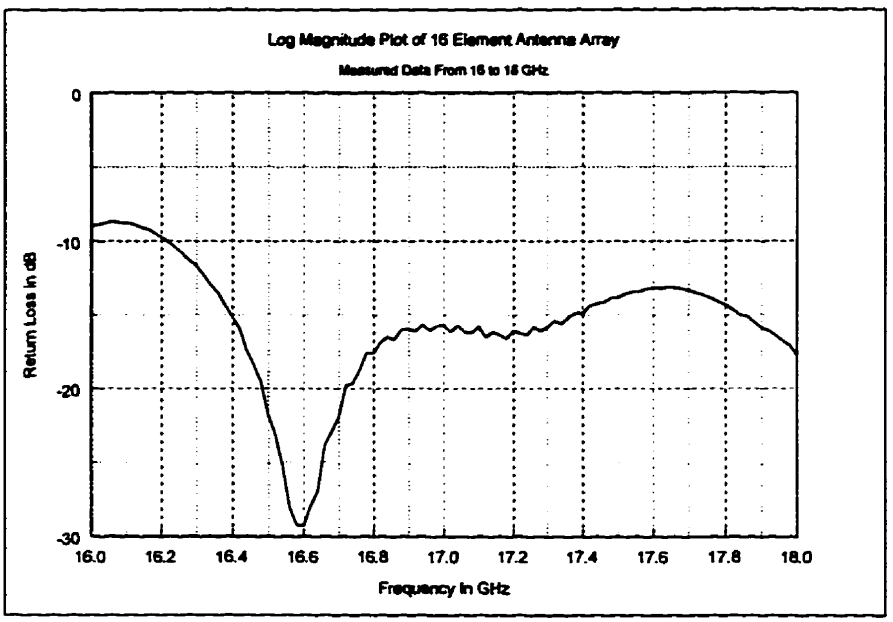

Figure 5.5 Measured log magnitude plot of the 16-element array

The simulated results with a coarse frequency sweep are included in Figure 5.6 on the next page.

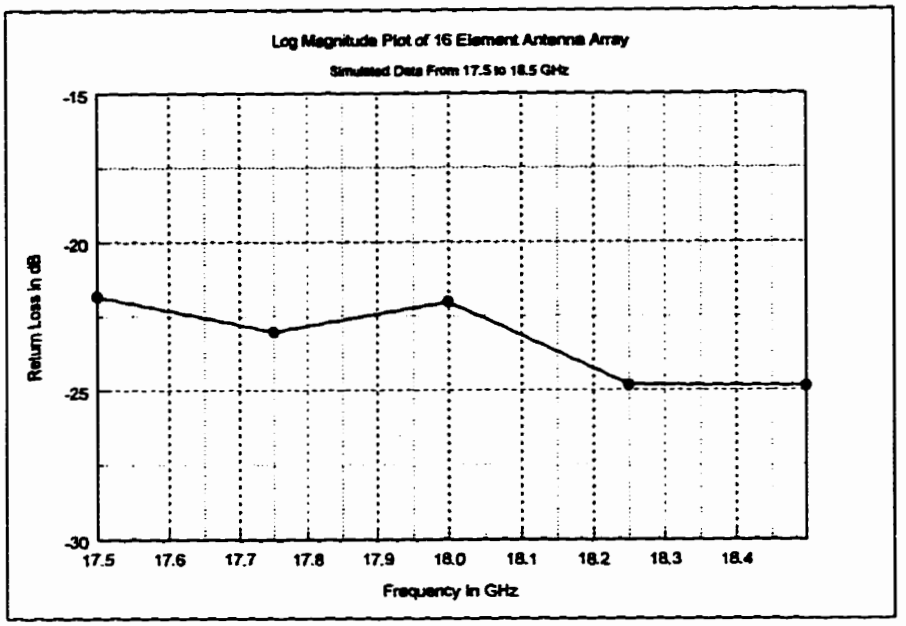

Figure 5.6 Simulated log magnitude plot of the 16-element array

5.2.3 Input Impedance

The measured input impedance is shown in Figure 5.7. The measured data shows a very good sized coupling loop centered on the chart for near optimum bandwidth performance.

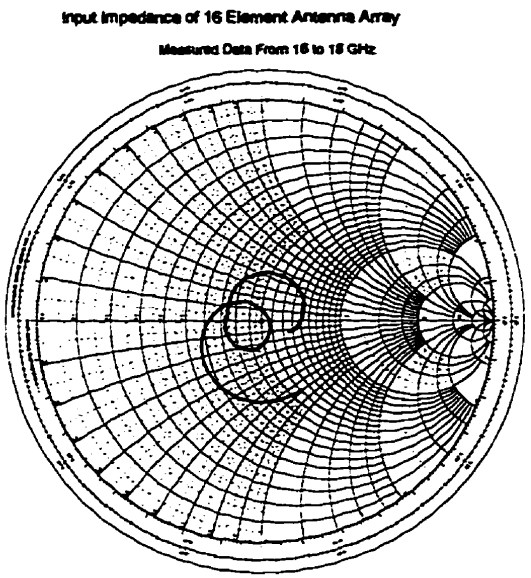

Figure 5.7 Measured input impedance of the 16-element array

The simulated results for the full array are included in Figure 5.8. This plot shows that the design was well matched for simulated frequencies from 17.5 to 18.5 GHz. More simulated data should have been collected but due to computer resources available (memory) and time contraints, only this subset of the desired range was simulated.

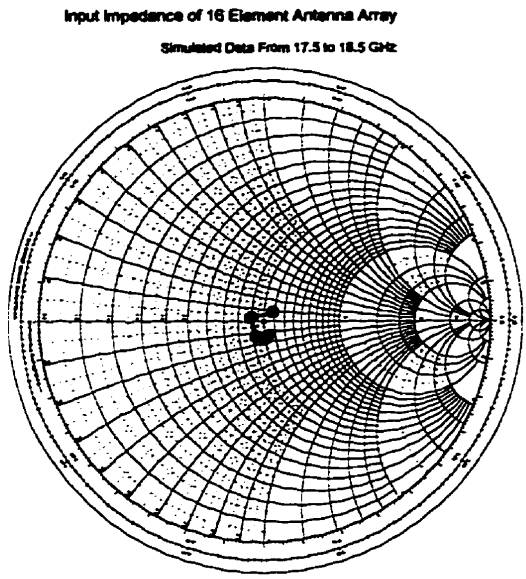

Figure 5.8 Simulated input impedance of the 16-element array

5.2.4 Bandwidth

The bandwidth of this array may be extracted from Figure 5.5. In this figure there exists a return loss better than -15dB from 16.2GHZ to better than 18.0GHz. This measured information corresponds to a better than 9% operating bandwidth.

5.2.5 Radiation Properties

The array is again measured using the same test calibration as the single element. The measured array radiation pattern of Figure 5.9 does not show any of the diffraction effects seen in the single element measurements. The radiation pattern exhibits symmetry and meets the design specifications in terms of side lobe level and required azimuth (H-Plane) and elevation (E-Plane) half power beamwidths.

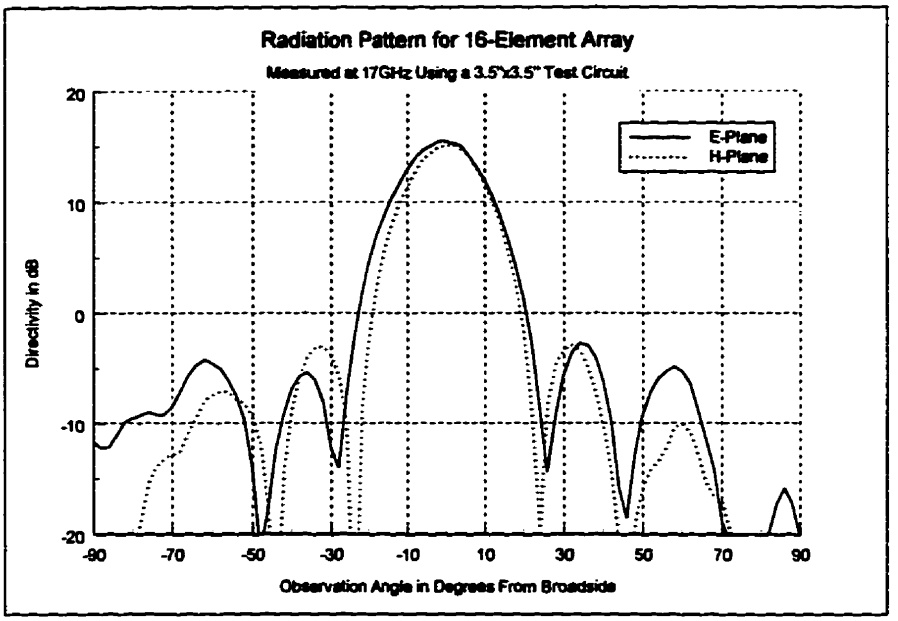

Figure 5.9 Radiation pattern measured for 16-element array

The radiation pattern obtained from linear array simulations for the azimuth and elevation arrays is shown in Figure 5.10 (see Figure 5.12 and Figure 5.15 for the array configurations used).

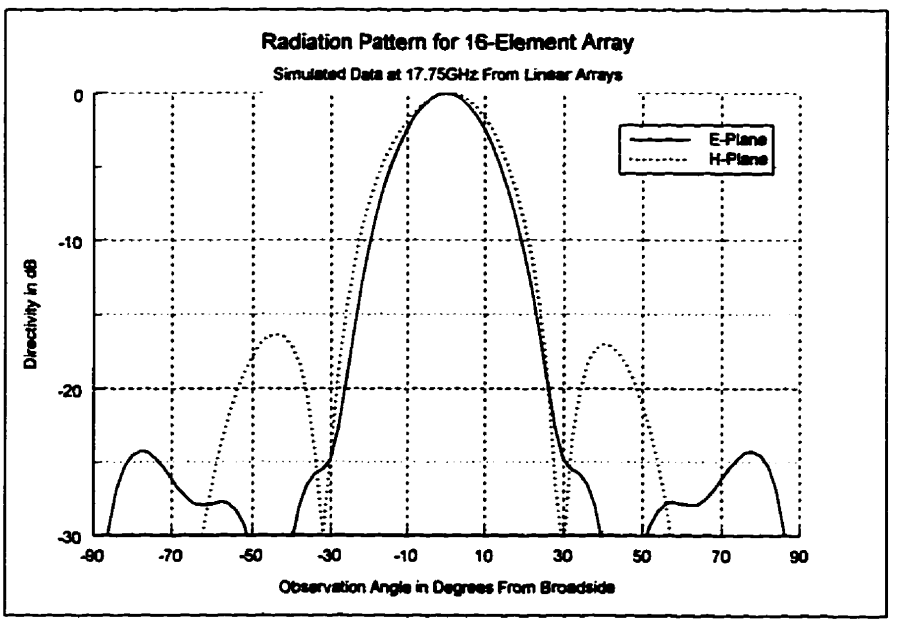

Figure 5.10 Simulated radiation pattern using linear array approximations

5.2.6 Directivity

The directivity for this antenna is again approximated using (5.1), the HPBW's for this antenna is extracted from the raw measured radiation pattern data. The E-Plane HPBW is $\theta_E = 18.26$ and the H-Plane $\theta_H = 19.93$. The estimated directivity for this antenna is

$$D_o = 89.03 \tag{5.9}$$

or

$$D_o = 19.5\,\text{dB} \tag{5.10}$$

5.2.7 Gain

The measured gain for this antenna is obtained from the measured radiation pattern data. There was a slight discrepancy for the gain measured in the two planes. The measured E-Plane gain was 15.44dB, while the measured H-Plane gain was 15.10dB; the higher value of the two was assumed to be the gain of this antenna.

$$G = 15.44\,\text{dB} \tag{5.11}$$

or in linear units

$$G = 35 \tag{5.12}$$

5.2.8 Efficiency

The efficiency for the radiating elements in the array is assumed to be the same as the value calculated for the single element. Using this assumption the total power loss of the array feed circuitry could be extracted. This section shows the crude method used to extract these feed circuitry losses. The antenna efficiency of $e_t = 0.722$ was changed to a loss of $L_\eta = 1.41$ dB. Assuming that (5.1) is accurate for this antenna the losses due to the feed circuit L_{FC} is the difference between the directivity and the antenna efficiency compensated, measured gain.

$$L_{FC} = D_o - (G + L_\eta) \tag{5.13}$$

The resulting feed circuit losses are estimated to be,

$$L_{FC} = 2.65\,\text{dB} \tag{5.14}$$

The overall antenna efficiency including the feed circuit losses is

$$= \frac{35}{89.03} = 0.393 \tag{5.15}$$

This efficiency although not ideal was deemed acceptable for use in an automotive radar system.

5.2.9 Mutual Coupling

The mutual coupling for this array configuration has been analyzed numerically using the Ensemble MoM package. This tool has proven to be extremely accurate and could easily provide this information. The problem is reduced to first an E-Plane line array, then as an H-Plane array. The simulated problem had four ports, one for each element, with the array amplitude distributions used at each element. The element used for

the E-Plane simulations is shown in Figure 5.11.

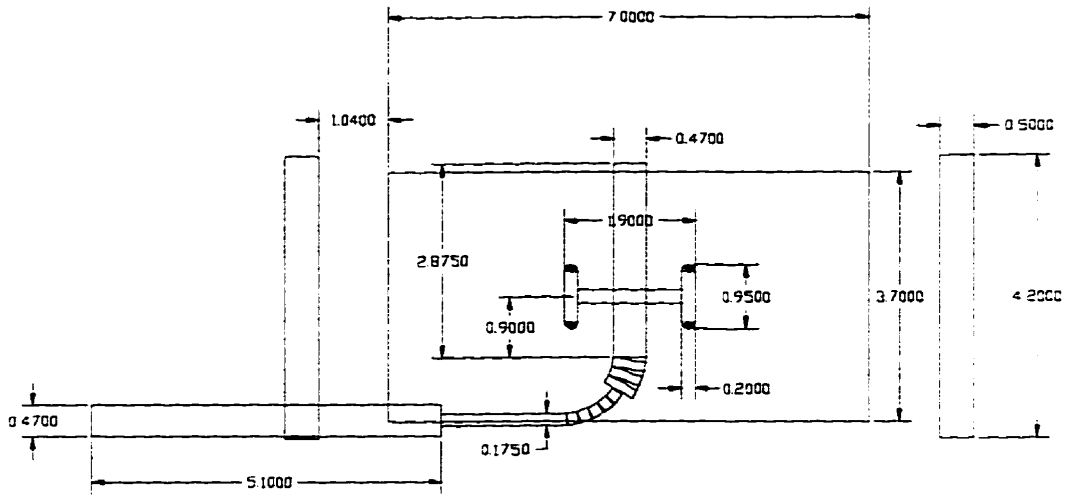

Figure 5.11 Element used in elevation plane mutual coupling analysis

The configuration used for the E-Plane simulation has elements with 12mm spacing between centers as shown in Figure 5.12.

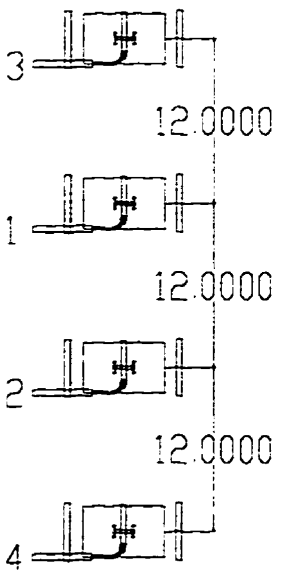

Figure 5.12 E-Plane configuration used to determine the mutual coupling

The mutual coupling between each element across this plane of the array is shown in Figure 5.13. In general the coupling level between the closest elements was approximately $-17dB$ with a slight increase as the frequency increases.

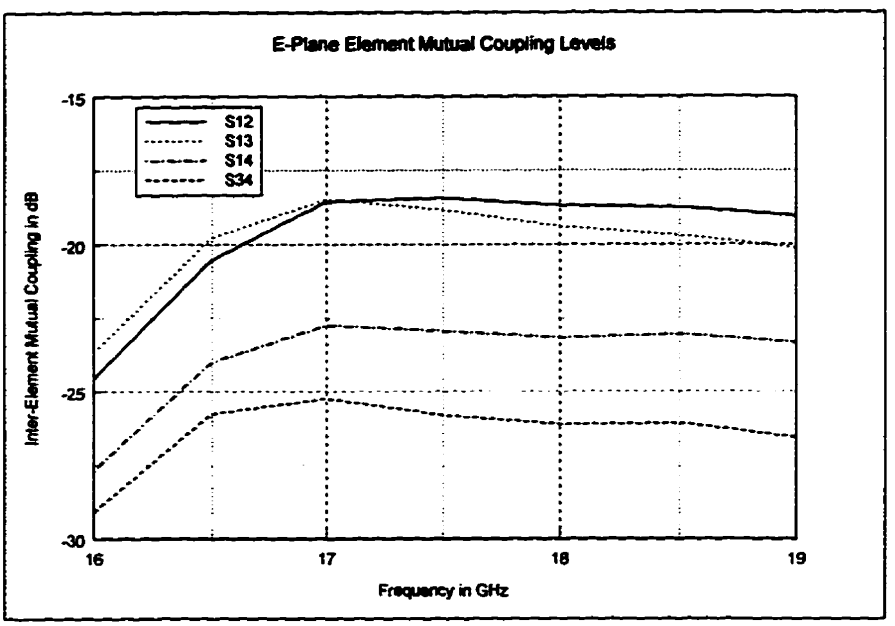

Figure 5.13 E-Plane element mutual coupling levels

The antennas elements used for the azimuth linear array analysis are shown in Figure 5.14.

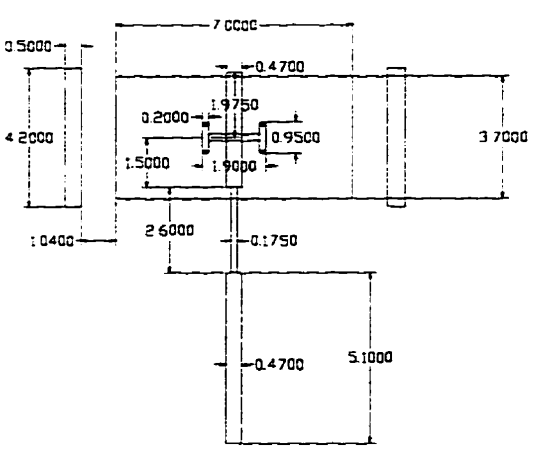

Figure 5.14 Elementcenter used in azimuth plane mutual coupling analysis

The azimuth linear array used to determine the H-Plane mutual coupling is shown below in Figure 5.15.

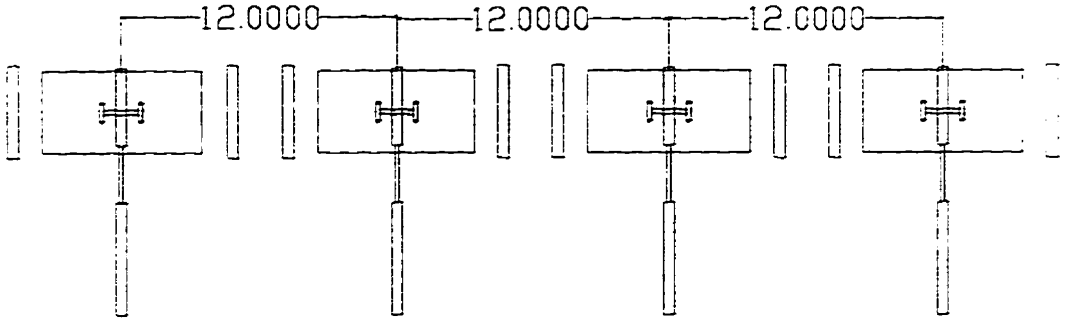

Figure 5.15 Configuration used to simulate H-Plane mutual coupling

In general the mutual coupling in H-Planes is lower than the level observed for the E-Plane. The mutual coupling levels obtained from this simulation are shown in Figure 5.16. This plot shows a lower coupling level than the E-Plane linear array, but it tends to increase at higher frequencies where the E-Plane coupling levels remain relatively flat.

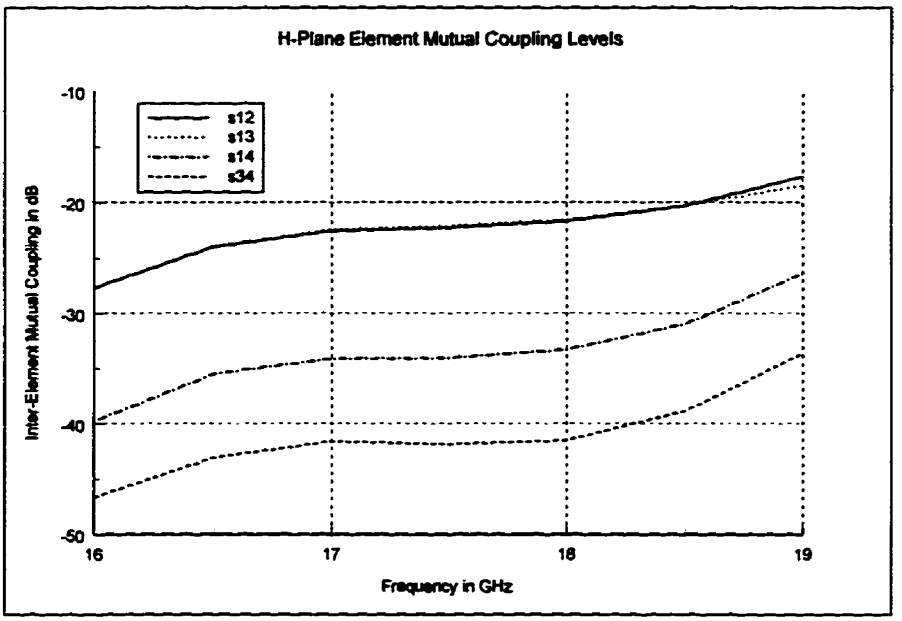

Figure 5.16 H-Plane element mutual coupling levels

This mutual coupling information will be used for the integrated transmit

and receive antenna to be designed later. This design is required to meet an isolation specification of 50dB, which may require some modifications to the substrate between the antenna arrays.

5.3 Radome Covered Antenna Array

5.3.1 Physical Dimensions and Material Properties

As detailed in the chapter on design, the radome was required to cover this antenna to protect it from the harsh environmental conditions it will experience. The material used was a material from General Electric called ULTEM. This material has similar properties to lexan but is also able to withstand exposure to hydrocarbons. The ULTEM layer used was a halfwave length which was determined to be about 5.2mm (0.205"). This protective layer was located roughly a halfwave wavelength above the antenna surface or 8.81mm (0.350"). The radome profile view of the configuration is shown in Figure 5.17.

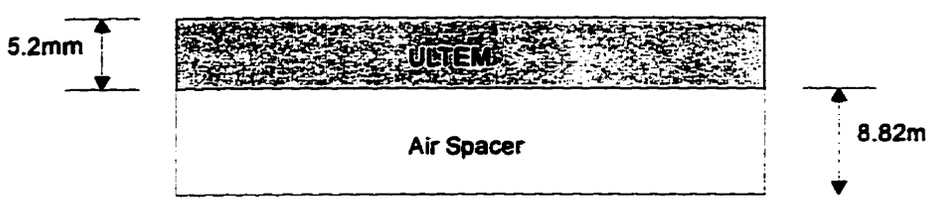

Figure 5.17 Profile of radome configuration

5.3.2 Resonant Frequency

The array resonant frequency was not changed appreciably when used with the radome configuration of the previous section.

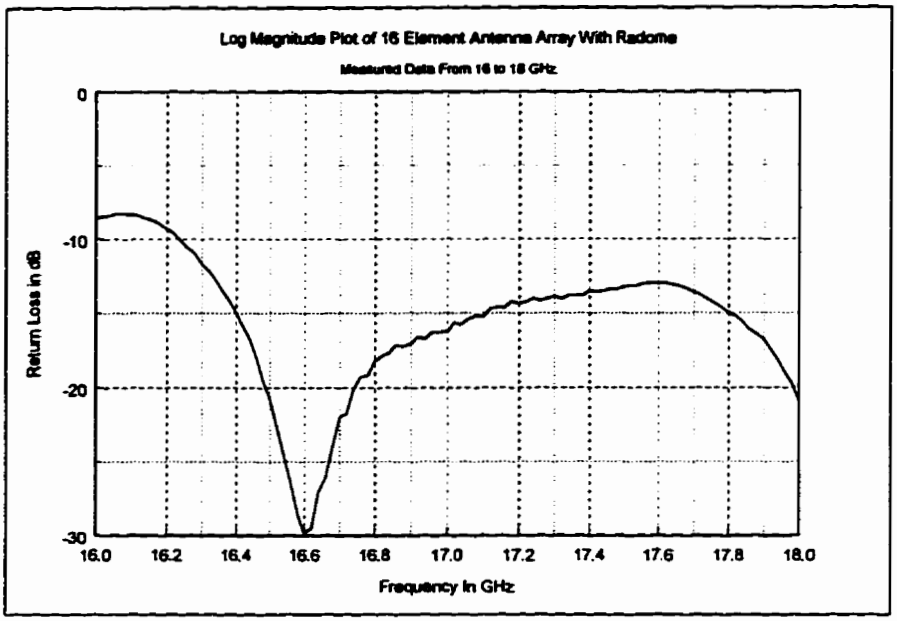

Figure 5.18 Radome covered 16-element antenna return loss

5.3.3 Input Impedance

The experimental measurements on the radome covered antenna show that with the spacing used, the radome had little or no effect on antenna input impedance.

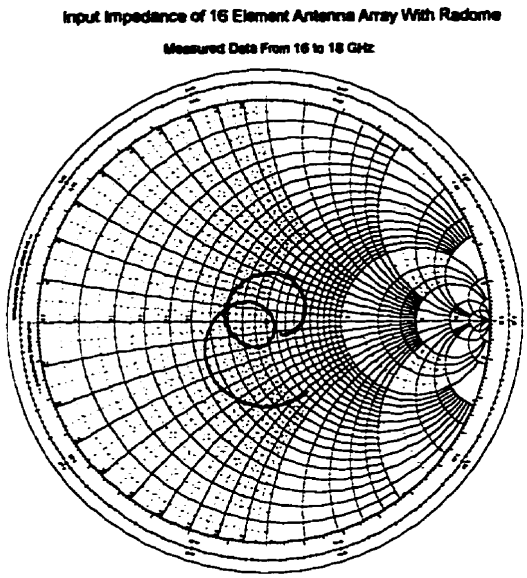

Figure 5.19 Radome covered 16-element antenna input impedance

5.3.4 Bandwidth

The radome design used proved to be very successful in terms of minimizing its loading effects on the antenna as the operating bandwidth was almost identical to the uncovered array measurements. This radome design might be compromised in the future as size is a major concern in the automotive market and there is pressure to move to a thinner radome structure.

5.3.5 Radiation Properties

To determine the radome transmission losses the antenna array radiation pattern is re-measured with the radome in place, and compared to the uncovered case. The H-Plane radiation plot with the covered and uncovered results super-imposed is shown in Figure 5.20.

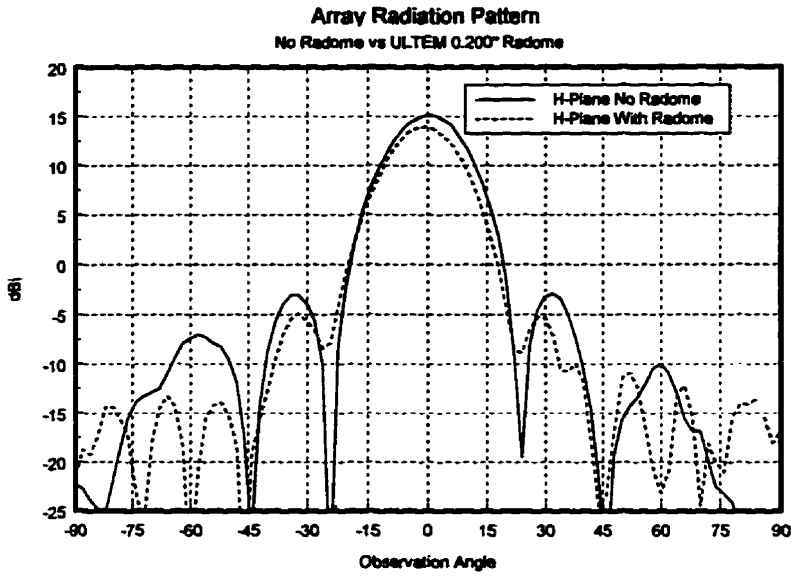

Figure 5.20 H-Plane radiation pattern of uncovered vs covered antenna array

5.3.6 Transmission Losses

The transmission losses for this radome configuration are determined by subtracting the gain measured with the radome, from the gain measured without the radome. The transmission loss was determined to be 1.16dB at the center frequency of 17.0GHz. These losses increased at both the upper and lower band edges. At the lower edge 16.2GHz the measured losses are 1.67dB and at the upper band edge the measured transmission loss is 1.42dB. The measured transmission loss minimum is close to the antenna center frequency; this confirms that the radome thickness used is near optimum.

CHAPTER 6: Conclusions

6.1 Conclusions

6.1.1 General

To start the concluding remarks a brief summary of the purpose of this research is provided. The antenna design presented in this thesis is part of the research into the development of a receive antenna for a potentially large volume automotive collision avoidance product. The automotive industry is notorious for aggressive pricing policies and this complex radar system was required to be produced with considerable pressure to reduce costs. The design created was relatively novel in terms of configuration, but entered a new realm of microwave engineering with the attempt to design a Ku-Band product on a commercial grade laminate. Traditional laminate materials are based on poly-tetraflouroethylene (PTFE) which although superior in electrical performance are considerably more expensive and did not meet the material cost projections for this program.

The design of an aperture fed microstrip patch antenna with parasitic elements on RO4003 was successful, and a working prototype fabricated, with the desired performance. This radiating element was then used in the creation of a 16-element array, in a 4x4 configuration, with a Taylor line source amplitude distribution to reduce side lobes. There were some concerns during the array development that the RO4003 would be too lossy to be used at Ku-Band, these concerns were moderated with the curvilinear array feed network developed. The feed circuit losses were determined to be 2.65dB which is in the range of array feed circuit losses experienced using much higher performance PTFE laminates.

The array design was successful as the array performance exceeded the antenna specifications. The 16-element array configuration was recently changed to a 24-element array for reduction of ground clutter seen in the elevation plane. The new array

design will be based on this work, and the same procedure used here, will be followed for that design.

6.1.2 Multilayer Antenna Analysis

The accurate analysis of a parasitic loaded, aperture fed antenna is critical for this design configuration to be utilized for any application. The attempt to produce simplified analysis models for this configurations fell short of providing accurate input impedance data but did provide substantial insight into the mechanics of this antenna. There is some work required to improve the accuracy of the aperture representation in the Transmission Line Model for this analysis to be applied to aperture fed antennas. The mode matching cavity model develops a rigorous analysis of the aperture feed, but requires a modified cavity representation to use this analysis method for parasitic loaded aperture fed antenna.

Fullwave analysis software of the same quality as Ensemble and IE3D are almost a necessity to obtain a well matched high performance antenna. These tools will only get more accurate and faster as theoretical engineers and mathematicians develop the science of numerical analysis of these complex multilayer structures, and the processing power of computers increases as it has in the last decade.

6.1.3 Microstrip Antenna Element

The aperture coupled patch antenna with coplanar parasitics was a successful design that was realized after many numerical design iterations. The success of this design is directly attributed to the availability of accurate commercial fullwave analysis tools like Ensemble and IE3D.

Simulated and experimentally measured results for the design created were in very good agreement. The measured results obtained for this antenna element met or

exceeded all element specifications. The impedance bandwidth was better than 16 to 18GHz (or 11.75%) with a center frequency of 17GHz. The minimum acceptable bandwidth was 16.25 to 17.75GHz or 8.8%. The radiation patterns measured were symmetrical for both the E and H-Plane measurements, which eliminated any concerns that the parasitic elements degrade the H-Plane radiation pattern. The element efficiency at $\eta = 0.722$ was lower than desired but was deemed acceptable and was a performance trade-off accepted when the design was committed to a commercial grade laminate. There is some concern about the element back radiation, although it has not been measured to date due to the limitations of our current measurement setup. The back radiation was seen in numeric simulations to be in the order of -15dB for the curved feed element. A new antenna test chamber is being assembled and these tests will be performed in future radiation pattern measurements.

This antenna element design was aided immensely with the fullwave analysis tools available at the research facility, and would have been difficult if not impossible to create without them. The commercial packages, Ensemble and IE3D, have been invaluable for this design work and are strongly recommended for microstrip antenna designers able to afford these pricy commercial tools.

6.1.4 Microstrip Array

The primary goal of this research was to develop a relatively wideband microstrip array design for a potentially large volume automotive radar program. This design was successful in that an acceptable array bandwidth was obtained, and the array radiation pattern met the half power bandwidth specifications of the time. The pattern measured had an elevation half power beamwidth of 18.26 degrees, and an azimuth beamwidth of 19.93 degrees. The measured antenna gains of 15.44dB were well below the theoretical directive gain based on half power beamwidths of 19.5dB. The array efficiency

determined to be $\eta = 0.393$ was lower than desired but was deemed acceptable considering the laminates used.

The experimental antenna element, and array, designed in this work is a precursor to future work in the ultra high volume automotive radar applications. Using microstrip antenna arrays fabricated on commercial grade laminates, at relatively high frequencies like Ku-Band, has been proven to be viable.

6.2 Future Work

This design was determined to have a few weak points, one of which was the ARLON 6700 bond ply used to laminate the fabricated protoype units. The use of this bond film is not easily incorporated in large volume processes, so alternative bond techniques will be required before production starts. A study of prepreg materials has already been started and modified designs should be completed relatively soon.

Another weak point of this design and a topic for future work is the antenna back radiation due to the aperture and feed circuit. There are plans to attempt to reduce this negative side-effect by using a stripline antenna feed, instead of the current microstrip. This configuration is also attractive as it permits the entire radar unit to manufactured as a multilayer board with microwave electronics, analogue circuits, and the power supply circuits separated from the feed network with a ground plane.

Yet another topic for future research is an investigation of a high permittivity dielectric feed layer. This study will begin if and when high permittivity commercial grade material become available.

There will be a parallel design created for the final product for ARLON 25N which is a new laminate product intended to compete against RO4003. This new material has an advantage over RO4003 in that a prepreg bond material is currently available which Rogers has promised to produce in the first quarter of 1998.

References

[1] D.M. Pozar, "A Microstrip Antenna Aperture Coupled to a Microstrip Line", Electronic Letters, Vol. 21, January 17, 1985 pp.49-50

[2] D.M. Pozar, "Microstrip Antennas", IEEE Proc., vol.80, Jan 1992, pp79-91

[3] D.H. Schaubert, "Microstrip Antennas", Electromagnetics, vol.12, pp 381-401, 1992

[4] D.M. Pozar and D.H. Schaubert, Microstrip Antennas: The analysis and design of microstrip antennas and arrays, IEEE Press, New York, 1995

[5] D.H. Schaubert and F.G. Farrar 'Some conformal printed circuit antenna designs", Proc. Printed Circuit Antenna Tech. Workshop, New Mexico State University, Las Cruces, 1979

[6] C.A. Balanis, "Antenna Theory Analysis and Design", John Wiley & Sons 1982

[7] K.R. Carver and J.W. Mink, "Microstrip Antenna Technology", IEEE Trans. on Antennas and Propagation vol. AP-29 no.1 Jan 1981 pp 2-24

[8] R.E. Collin, "Field Theory of Guided Waves", IEEE Press 1991

[9] R.E. Collin, "Foundations for Microwave Engineering", McGraw-Hill, Inc. NewYork

[10] T. Horng and N.G. Alexopoulos, "Corporate Feed Design for Microstrip Arrays:, IEEE Trans. on Antennas and Propagation vol. AP-41 no.12 Dec 1993 pp.1615-1624

[11] R.F. Harrington, "Time-Harmonic Electromagnetic Fields", McGraw-Hill Inc 1961

[12] M. Himdi, J.P. Daniel and C. Terret, "Analysis of Aperture-Coupled Microstrip Antenna Using Cavity Method", Electronic Letters 16 March 1989 vol. 25 no.6 pp.391-392

[13] M. Himdi, J.P. Daniel and C. Terret, "Transmission Line Analysis of Aperture-Coupled Microstrip Antenna", Electronic Letters 31 Aug 1989 vol. 25 no.18 pp. 1229-1230

[14] P.S. Hall and C.M. Hall, "Coplanar Corporate Feed Effects in Microstrip Patch Array Design", IEE Proceedings vol.135 Pt. H no.3 June 1988 pp. 180-186

[15] A. Ittipiboon, R. Oostlander and Y.M.M. Antar, "Modal Expansion Method of Analysis for Slot-Coupled Microstrip Antenna", Electronic Letters 28 Sept. 1989 vol.25 no.20 pp.1338-1340

[16] A. Ittipiboon, R. Oostlander, Y.M.M. Antar and M. Cuhaci, "A Modal Expansion Method of Analysis and Measurement on Aperture-Coupled Microstrip Antenna", IEEE Trans. on Antennas and Propagation vol. AP-39 no.11 Nov 1991 pp.1567-1574

[17] Edited by J.R. James and P.S. Hall, "Handbook of Microstrip Antennas", Peter Peregrinus Ltd. 1989

[18] R.P Jedlinka, M.T Poe and K.R. Carver, "Measured Mutual Coupling Between Microstrip Antennas", IEEE Trans. on Antennas and Propagation vol. AP-29 no.1 Jan 1981 pp.147-149

[19] P.B. Katehi, "A Generalized method for the Evaluation of Mutual Coupling in Microstrip Arrays", IEEE Trans. on Antennas and Propagation vol. AP-35 no.2 Feb 1987 pp.125-133

[20] P.B. Katehi, "Mutual Coupling Between Microstip Dipoles in Multi-Element Arrays", IEEE Trans. on Antennas and Propagation vol. AP-37 no.3 March 1989 pp.275-280

[21] J.D. Kraus and K.R. Carver, "Electromagnetics", 2nd Edition, McGraw-Hill Book Co., Toronto 1973

[22] D.F. Kelley and W.L. Stutzman, "Array Antenna Pattern Modeling Methods That Include Mutual Coupling Effects", IEEE Trans. on Antennas and Propagation vol. AP-41 no.12 Dec 1993 pp.1625-1632

[23] R. Oostlander, Y.M.M. Antar, A. Ittipiboon, and M. Cuhaci, "Aperture Coupled Microstrip Antenna Element Design", Electronic Letters 15 Feb 1990 vol. 26 no. 4 pp.224-225

[24] R. Oostlander, "A Study of Microstrip Antenna Elements Fed Via Aperture Coupling", M.Eng. Thesis, Royal Military College of Canada 1989

[25] D.M. Pozar, "Input Impedance and Mutual Coupling of Rectangular Microstrip Antennas", IEEE Trans. on Antennas and Propagation vol.AP-30, no.6 Nov 1982 pp1191-1196

[26] D.M. Pozar, "Considerations for Millimeter Wave Printed Antennas", IEEE Trans. on Antennas and Propagation vol.AP-31, no.5 Sept 1983 pp740-747

[27] D.M. Pozar, "A Reciprocity Method of Analysis for Printed Slot and Slot-Coupled Microstrip Antennas", IEEE Trans. on Antennas and Propagation vol.AP-34, no.12 Dec 1986 pp.1439-1446

[28] D.M. Pozar, "Analysis of an Infinite Phased Array of Aperture Coupled Microstrip Patches", IEEE Trans. on Antennas and Propagation vol.AP-37, no.4 April 1989 pp.418-425

[29] D.M. Pozar, "Recent Developments in the Analysis and Design of Microstrip Arrays", ANTEM 1992 Conference Proceedings Aug 1992 pp.509-515

[30] J.S. Rao, K.K. Joshi and B.N. Das, "Analysis of Small Aperture Coupling Between Rectangular Waveguide and Microstrip Line", IEEE Trans. on Microwave Theory and Techniques vol MTT-29 no.2 Feb 1981 pp.150-154

[31] P.L. Sullivan and D.H. Schaubert, "Analysis of an Aperture Coupled Microstrip Antenna",

IEEE Trans. on Antennas and Propagation vol.AP-34, no.8 Aug 1986 pp.977-984

[32] F. Croq and D.M. Pozar, "Millimeter Wave Design of Wide-Band Aperture Coupled Stacked Microstrip Antennas", IEEE Trans. on Antennas and Propagation vol.AP-39, no.12 Dec 1991 pp.1770-1776

[33] R.K. Hoffmann, "Handbook of Microwave Integrated Circuits", Artech House 1987

[34] D.M . Pozar and S.D. Targonski, "Improved Coupling For Aperture Coupled Microstrip Antennas", Electronic Letters 20 June 1991, pp.1129-1131

[35] M. El Yazidi, M. Himdi and J.P. Daniel, "Transmission Line Analysis of Nonlinear Slot Coupled Microstrip Antenna", Electronic Letters 16 July 1992, vol 28 no.15, pp1406-1408

[36] D.M. Pozar and R.W. Jackson, "An Aperture Coupled Microstrip Antenna With a Proximity Feed on a Perpendicular Substrate", IEEE Trans. on Antennas and Propagation vol.AP-35, no.6 June 1987 pp.728-731

[37] D.H. Schaubert, "A Review of Some Microstrip Antenna Characteristics", Microstrip Antennas IEEE Press, 1995 pp.59-67

[38] Y.K. Cho, G.H. Son, G.S. Chae, L.H. Yun and J.P. Hong, "Improved Analysis Method for Broadband Rectangular Microstrip Antenna Geometry Using E-Plane Gap Coupling", Electronic Letters 28 Oct 1993, vol 29 no.22 pp.1907-1909

[39] G. Kumar and K.C. Gupta, "Non-radiating Edges and Four Edges Gap-Coupled Multiple Resonator Broad-Band Microstrip Antennas", IEEE Trans. on Antennas and Propagation vol.AP-33 1984 pp.1375-1379

[40] R.E. Munson, "Conformal Microstrip Antennas and Microstrip Phased Arrays", IEEE Trans. on Antennas and Propagation vol.AP-22 no.1 Jan 1974 pp.74-78

[41] I.J. Bahl and P. Bhartia, "Microstrip Antennas", Canton, Mass., Artech House, 1980

[42] G. Matthaei, L. Young and E.M.T Jones,"Microwave Filters, Impedance-Matching Networks, and Coupling Structures", Dedham Mass., Artech House Books, Reprinted in 1980

[43] H. Pues and A. Van de Capelle, "Accurate Transmission-Line Model for The Rectangular Microstrip Antenna", IEE Proceedings vol.131 Pt. H no.6 Dec 1984 pp.334-340

[44] M. Himdi and J.P. Daniel, "Analysis of Printed Linear Slot Antenna Using Lossy Transmission Line Model", Electronic Letters 12 March 1992, vol 28 no.28 pp.598-601

[45] E.H. Van Lil and A.R. Van de Capelle, "Transmission Line Model for Mutual Coupling Between Microstrip Antennas', IEEE Trans. on Antennas and Propagation vol.AP-32 no.8 Aug 1984 pp816-821

[46] D.M. Pozar and J.R. James, "A Review of CAD for Microstrip Antennas and Arrays", Microstrip Antennas: The analysis and design of microstrip antennas and arrays, IEEE Press, New York, 1995

[47] M. Kirschning, R.H. Jansen and N.H.L. Koster,"Accurate Model For The Open End Effect of Microstrip Lines", Electronic Letters 17 March 1981 pp.123-125

[48] J.S. Rao and B.N. Das, "Impedance Characteristics of Transverse Slots In The Ground Plane of a Stripline", IEE Proceedings vol.125 Pt. H no.1 Jan 1978 pp. 29-32

[49] R.F. Harrington, "Field Computation by Moment Methods", New York, Macmillan Company 1968

[50] Edited by T. Itoh, "Numerical Techniques for Microwave and Millimeter-Wave Passive Structures", New York, John Wiley & Sons 1989

[51] T.T Taylor, "Design of Line-Source Antennas for Narrow Beamwidth and Low Sidelobes", IRE Trans. Antenna Propagation, vol AP-3, no.1 pp.16-28 1955

[52] Edited by Y.T. Lo and S.W. Lee, "Antenna Handbook", New York, Van Nostrand Reinhold 1993

[53] R.Q. Lee and K.F. Lee, "Gain Enhancement of Microstrip Antennas With Overlaying Parasitic Directors", Electronic Letters 26 May 1988 pp.656-658

[54] E.Levine, G.Malumud, S.Shtrikman, and D.Treves,"A study of microstrip antennas with the feed network," IEEE Trans. on Antennas and Propagation vol.AP-37 no.4 Aug 1989 pp426-434

[55] E. Hammerstad, 0. Jensen,"Accurate Models For Microwave Computer Aided Design", IEEE MTT Symposium Digest 1980 pp 407-409

[56] M. Kirschning and R.H. Jansen, "Accurate Models for Effective Dielectric Constant of Microstrip with Validity up to Millimeter Wave Frequencies", Electronic Letters vol. 18 no.6 1982 pp.272-273

[57] R.H Jansen and M. Kirschning,"Arguements and an Accurate Mathematical Model for the Power Current Formulation of Microstrip Characteristic Impedance",Arch. Elektronik u. Ubertragungstechn, vol. 37 1983

[58] M. Abramowitz and I. Stegun, "Handbook of Mathematical Functions", US Government Printing Office, 1993

[59] D. Rhodes, "Synthesis of planar antenna sources", Oxford University Press 1974

[60] S.B. Cohn, "Slot-line on a dielectric substrate",IEEE MTT vol.17 no.10 pp. 768-778

[61] J. Huang, "The Finite Ground Plane Effect on the Microstrip Antenna Radiation Patterns", IEEE Trans. on Antennas and Propagation vol.AP-31 no.4 July 1983 pp.649-653

[62] R.J. Stegun, "Excitation Coefficients and Beamwidthes of Tschebyscheff Arrays", Proceedings of the IRE, Jan. 1952 pp. 78-82

[63] J.D. Kraus, "Antennas", McGraw Hill, New York, 1988

[64] Edited by J.D. Walton, "Radome Engineering Handbook", Marcel Dekker, New York, 1970

[65] B.C. Wadell,"Transmission Line Design Handbook", Artech House, Boston, Ma. 1991

Appendix A

C++ Computer Programs
for
Microstrip Transmission Line Model

A.1 Main Transmission Line Model Program

```
#include<math.h>
#include<iostream.h>
#include<fstream.h>
#include<stdio.h>
#include <io.h>
#include <stdlib.h>
#include "dnm-math.h"
#include "cct-4r1.h"
const double EO=8.854e-12;
const double UO=1.25664e-6;
const double PI=acos(-1);
const double Ce=0.577216;
const double CO=1/sqrt(EO*UO);
const double NO=sqrt(UO/EO);
const int MAXPATH=128;
// Global Variables
SUBSTRATE sub;
PATCH_DIMS patch;
LINE_DIMS line;
double fmin, fmax;
double  test_pts;
// Function Declaration
void get_input_data();
// MAIN PROGRAM
void main()
{get_input_data();
ofstream output_File("mstpfed.dat");
output_File.clear();
output_File.precision(6);
output_File.width(8);
PATCH_CCT patchimpedance;
LINE_DATA line1;
fcomplex Z;
fcomplex linegamma;
double freq;
double delta_freq=(fmax-fmin)/test_pts;
for (freq=fmin;freq<(fmax+delta_freq);freq=freq+delta_freq)
{patchimpedance=pcct( sub, patch, freq );
Z=patchimpedance.Z;
line1=linecalc(sub, line, freq );
linegamma=line1.gamma;
cout << "\n" << freq << "\t" << Z.r << "\t"
<< Z.i << "\t" << line1.Zcf << "\t\t"
<< linegamma.r << "\t" << linegamma.i;
output_File << "\n" <<freq << "\t" << Z.r
<< "\t" << Z.i << "\t" << line1.Zcf
<< "\t" << linegamma.r << "\t" << linegamma.i;
}
output_File.close();
```

```
}
// GET PATCH INPUT DATA
void get_input_data()
{FILE *input_data;
char file_name[MAXPATH];
printf("\nFile With Patch Data:");
gets(file_name);
if ((input_data=fopen(file_name,"r"))==NULL)
{fprintf(stderr,"Cannot Open File %s\n",file_name);
exit;
}
if (file_name[0]=='\0')
{fprintf(stderr,"No File Name Entered\n");
exit;
}
if (access(file_name,04)==0)
{fscanf(input_data,"%*s%*s%*s%*s");
fscanf(input_data,"%*s%*s");
fscanf(input_data,"%lf",&patch.l);
fscanf(input_data,"%*s%*s");
fscanf(input_data,"%lf",&patch.w);
fscanf(input_data,"%*s%*s");
fscanf(input_data,"%lf",&patch.feedwidth);
fscanf(input_data,"%*s%*s%*s%*s%*s");
fscanf(input_data,"%*s%*s");
fscanf(input_data,"%lf",&fmax);
fscanf(input_data,"%*s%*s");
fscanf(input_data,"%lf",&fmin);
fscanf(input_data,"%*s%*s");
fscanf(input_data,"%lf",&test_pts);
fscanf(input_data,"%*s%*s%*s%*s%*s");
fscanf(input_data,"%*s%*s");
fscanf(input_data,"%lf",&sub.er);
fscanf(input_data,"%*s%*s");
fscanf(input_data,"%lf",&sub.h);
fscanf(input_data,"%*s%*s");
fscanf(input_data,"%lf",&sub.t);
fscanf(input_data,"%*s%*s");
fscanf(input_data,"%lf",&sub.os);
fscanf(input_data,"%*s%*s%*s");
fscanf(input_data,"%lf",&sub.og);
fscanf(input_data,"%*s%*s");
fscanf(input_data,"%lf",&sub.lossTan);
fscanf(input_data,"%*s%*s%*s");
fscanf(input_data,"%lf",&sub.ds);
fscanf(input_data,"%*s%*s%*s%*s%*s");
fscanf(input_data,"%lf",&sub.dg);
fscanf(input_data,"%*s%*s%*s");
fscanf(input_data,"%lf",&line.l);
fscanf(input_data,"%*s%*s");
fscanf(input_data,"%lf",&line.w);
}
}
```

A.2 Function Routines Called By Main TL-Model Program

```
#include<iostream.h>
#include <math.h>
#include "dnm-math.h"

const doublePI=acos(-1);
const doubleEO=1e-9/(36*PI);
const doubleUO=4*PI*1e-7;
const doubleCO=1/sqrt(EO*UO);
const doubleNO=sqrt(UO/EO);
const doubleCe=0.577216;
typedef struct SUBSTRATE
{double er;double h;
double lossTan;
double os;double og;
double ds;double dg;
double t;
}substrate;
typedef struct PATCH_DIMS
{double l;double w;
double feedwidth;
}patch_dims;
typedef struct LINE_DIMS
{double l;double w;
}line_dims;
typedef struct PATCH_DATA
{double wh;double wt;double fn;
double Er0;double Erf;double W0;
double Wf;double lext;double Zc0;
double Zcf;double beta;double attn;
}patch_data;
typedef struct LINE_DATA
{double Er0;double Erf;double W0;
double Wf;double Zc0;double Zcf;
fcomplex gamma;
}line_data;
typedef struct PATCH_CCT
{fcomplex Z;fcomplex Ys;
fcomplex Ym;fcomplex gamma;
}patch_cct;
typedef struct STEP_DIMS
{double w1;double w2;
double w1f;double w2f;
double Er1f;double Er2f;
double Z1f;double Z2f;
int juncFLAG;
}step_dims;
typedef struct STEP_CCT
{double Ls;double Cp;
}step_cct;
//************************************
//********** Function List **********
```

```
//************************************
PATCH_CCT pcct(SUBSTRATE sub,PATCH_DIMS patch,double freq );
double F_ZC_freq(SUBSTRATE sub,double w,double Er0,double Erf,
   double Zc0, double freq);
double F_lext(SUBSTRATE sub,PATCH_DIMS patch,PATCH_DATA pdata );
double F_ER_freq(SUBSTRATE sub,double w,double wt,
   double fn,double Er0 );
double F_ER_static( SUBSTRATE sub, double w );
double F_W_static( SUBSTRATE sub, double wt );
double F_W_freq(double Erf,double h,double Zcf );
fcomplex F_Ys(double n_s,double n_w,SUBSTRATE sub,
   PATCH_DATA pdata);
fcomplex F_Ym(double n_l,double n_s,double n_w,fcomplex Ys);
double F_attn( SUBSTRATE sub,double W,double Wt,double W0,double freq,
   double beta, double Zc0, double Er0, double Erf );
fcomplex LINEFEDpatch(PATCH_DIMS patch,PATCH_DATA pdata,
   PATCH_CCT admits );
LINE_DATA linecalc(SUBSTRATE sub,LINE_DIMS line,double freq );
fcomplex F_wstep( SUBSTRATE sub,double W1,double W2,double Erf1,
   double Erf2,double Wf1,double Wf2,double Zc1,
   double Zc2,double Freq, int juncFLAG );
//************************************************
// FUNCTION: STEP IN FEEDLINE WIDTH
//************************************************
fcomplex F_wstep(SUBSTRATE sub,double W1,double W2,double Erf1,
   double Erf2,double Wf1,double Wf2,double Zc1,
         double Zc2,double Freq, int juncFLAG )
{if( Wf1<Wf2 )// NOTICE REQUIRE THAT:Wf1>Wf2
double Wtemp=Wf1;double Ztemp=Zc1;double ERtemp=Erf1;
Wf1=Wf2;
Zc1=Zc2;
Erf1=Erf2;
Wf2=Wtemp;
Zc2=Ztemp;
Erf2=ERtemp;
}
double a=Wf2/Wf1;
double D=sqr(4*a/(1-sqr(a)));
int SS=2;
// NOTICE "juncFLAG" for symmetrical=0 or asymmetrical=1
juncFLAG=0;
if( juncFLAG==1 ){ SS=1;
}else{SS=2;}
double lambda1=CO/(Freq*sqrt(Erf1));
double lambda2=CO/(Freq*sqrt(Erf2));
double AAtemp=sqrt(1-sqr(2*Wf1/(SS*lambda1)));
double AA=pow((1+a)/(1-a),2/a)*((1+AAtemp)/(1-AAtemp))
   -((1+3*sqr(a))/(1-sqr(a)));
   double BBtemp=sqrt(1-sqr(2*Wf2/(SS*lambda2)));
   double BB = pow((1+a)/(1-a),a/2)*((1+BBtemp)/(1-BBtemp))
   -((3+sqr(a))/(1-sqr(a)));
fcomplex ans;
ans.r = ((Zc1*4*Wf1)/(SS*lambda1*2*PI*Freq))*
   (log(((1-sqr(a))/(4*a))
```

```
    *pow((1+a)/(1-a),(a+(1/a))/2))
    +2*((AA+BB+2*D)/(AA*BB-sqr(D)))
    +sqr(Wf1/(2*SS*lambda1))
    *pow((1-a)/(1+a),4*a)
    *sqr(((5*sqr(a)-1)/(1-sqr(a)))
    +((4*D*sqr(a))/(3*AA))));
ans.i=((sqrt(Erf1)/(Zc1*CO))-(EO*sub.er*W1/sub.h))*((W1-W2)/2);
return ans;
};
//*************************************************************
// FUNCTION: MICROSTRIP LINE CALCULATOR
//*************************************************************
LINE_DATA linecalc(SUBSTRATE sub,LINE_DIMS line,double freq )
{
LINE_DATA ldata;
ldata.Er0=F_ER_static(sub, line.w);
double wt=line.w+(sub.t/PI)*(1+log(4/sqrt(pow(sub.t/sub.h,2)
    +pow(1/PI,2)/pow((line.w/sub.t)+1.1,2))));
ldata.W0=F_W_static(sub, wt);
ldata.Zc0=(sub.h*NO)/(ldata.W0*sqrt(ldata.Er0));
double fn=freq*sub.h*1e-6;
ldata.Erf=F_ER_freq(sub,line.w,wt,fn,ldata.Er0);
ldata.Zcf=F_ZC_freq(sub,line.w,ldata.Er0,ldata.Erf,ldata.Zc0,freq);
ldata.Wf=F_W_freq(ldata.Erf,sub.h,ldata.Zcf);
double ko=2*PI*freq/CO;
double beta=ko*sqrt(ldata.Erf);
double attn=F_attn(sub,line.w,wt,ldata.W0,freq,beta
    ,ldata.Zc0,ldata.Er0,ldata.Erf);
ldata.gamma=Complex(attn,beta);
return ldata;
}
//*************************************************
// FUNCTION: PATCH PARAMETERS
//*************************************************
PATCH_CCT pcct(SUBSTRATE sub,PATCH_DIMS patch,double freq )
{
PATCH_DATA pdata;
PATCH_CCT poutput;
pdata.Er0=F_ER_static(sub,patch.w);
pdata.wt=patch.w+(sub.t/PI)*(1+log(4/sqrt(pow(sub.t/sub.h,2)
    +pow(1/PI,2)/pow((patch.w/sub.t)+1.1,2))));
pdata.W0=F_W_static(sub, pdata.wt);
pdata.Zc0=(sub.h*NO)/(pdata.W0*sqrt(pdata.Er0));
pdata.fn=freq*sub.h*1e-6;
pdata.Erf=F_ER_freq(sub,patch.w,pdata.wt,pdata.fn,pdata.Er0);
pdata.lext=F_lext( sub, patch, pdata );
pdata.Zcf=F_ZC_freq(sub,patch.w,pdata.Er0,pdata.Erf,pdata.Zc0,freq);
pdata.Wf=F_W_freq(pdata.Erf,sub.h,pdata.Zcf);
double ko=2*PI*freq/CO;
double n_s=ko*pdata.lext;
double n_w=ko*pdata.Wf;
double n_l=ko*(patch.l+pdata.lext);
pdata.beta=ko*sqrt(pdata.Erf);
poutput.Ys=F_Ys(n_s,n_w,sub,pdata);
```

```
poutput.Ym=F_Ym(n_l,n_s,n_w,poutput.Ys);
pdata.attn=F_attn(sub,patch.w,pdata.wt,pdata.W0,freq,pdata.beta
    ,pdata.Zc0,pdata.Er0,pdata.Erf);
poutput.gamma=Complex(pdata.attn,pdata.beta);
poutput.Z=LINEFEDpatch(patch,pdata,poutput);
return poutput;
}
//*************************************
// FUNCTION: LINE FED PATCH
//*************************************
fcomplex LINEFEDpatch(PATCH_DIMS patch,PATCH_DATA pdata
    ,PATCH_CCT admits)
{
admits.gamma=Complex(pdata.attn,pdata.beta);
double f_ratio=1-patch.feedwidth/pdata.Wf;
fcomplex Yf=(f_ratio-1)*admits.Ys;
fcomplex Yc=Complex(1/pdata.Zcf,0);
fcomplex Yin=(sqr(Yc)+sqr(admits.Ys)-sqr(admits.Ym)
    +(2*admits.Ys*Yc*coth(patch.l*admits.gamma))
    -(2*admits.Ym*Yc*csch(patch.l*admits.gamma)))
          /(admits.Ys+Yc*coth(patch.l*admits.gamma));
Yin=Yin+Yf;
fcomplex Zin=1/Yin;
return Zin;
}
//*************************************************
// FUNCTION ATTENUATION CONSTANT
//*************************************************
double F_attn(SUBSTRATE sub,double W,double Wt,double W0
    ,double freq,double beta,double Zc0
          ,double Er0,double Erf)
{
double attn,alpn;
double Fs=1+2*sub.h/Wt*(1-(1/PI)+((Wt-W)/sub.t));
double Rss=sqrt(PI*freq*UO/sub.os);
double Rsg=sqrt(PI*freq*UO/sub.og);
double Fds=1+(2/PI)*atan(1.4*sqr(Rss*sub.ds*sub.os));
double Fdg=1+(2/PI)*atan(1.4*sqr(Rsg*sub.dg*sub.og));
double alpd=0.5*beta*(sub.er/Erf)*((Erf-1)/(sub.er-1))*sub.lossTan;
if (Wt/sub.h < 1)
{alpn=(1/(4*PI*sub.h*Zc0))*((32-sqr(Wt/sub.h))/(32+sqr(Wt/sub.h)));
}else
{alpn=(sqrt(Er0)/(2*NO*W0))*(Wt/sub.h+((0.667*Wt/sub.h)/
    (Wt/sub.h+1.444)));
}
double alpcs=alpn*Rss*Fds*Fs;
double alpcg=alpn*Rsg*Fdg;
attn=alpd+alpcs+alpcg;
return attn;
}
//*************************************************
// FUNCTION: MUTUAL SLOT ADMITTANCE
//*************************************************
fcomplex F_Ym(double n_l,double n_s,double n_w,fcomplex Ys)
```

```
{fcomplex ans;
double Gs=Ys.r;
double Bs=Ys.i;
double Fg=bessj0(n_l)+(sqr(n_s)/(24-sqr(n_s)))*bessj(2,n_l);
double Gm=Gs*Fg;
double Fb=(PI/2)*((bessy0(n_l)+(sqr(n_s)/(24-sqr(n_s)))
   *bessy(2,n_l))/(log(n_s/2)+Ce-1.5+((sqr(n_s)/12)
   /(24-sqr(n_s)))));
double Kb=1-exp(-0.21*n_w);
double Bm=Bs*Fb*Kb;
return ans=Complex(Gm,Bm);
}
//*****************************************
// FUNCTION: SLOT ADMITTANCE
//*****************************************
fcomplex F_Ys(double n_s,double n_w,SUBSTRATE sub,PATCH_DATA pdata)
{fcomplex ans;
double Bs,Gs,Yc_f;
Yc_f=1/pdata.Zcf;
Bs=Yc_f*tan(pdata.beta*pdata.lext);
Gs=(1/(PI*NO))*((n_w*Si(n_w)+sinc(n_w)+cos(n_w)-2)
   *(1-sqr(n_s)/24)+(sqr(n_s)/12)
   *(1/3+cos(n_w)/sqr(n_w)-sin(n_w)/pow(n_w,3)));
ans=Complex(Gs,Bs);
return ans;
}
//**************************
// FUNCTION: Weff(f)
//**************************
double F_W_freq(double Erf,double h,double Zcf)
{double ans;
ans=(h*NO)/(Zcf*sqrt(Erf));
return ans;
}
//***********************
// FUNCTION: Zc(f)
//***********************
double F_ZC_freq(SUBSTRATE sub,double w,double Er0,double Erf
   ,double Zc0, double freq)
{double ans,r7,r9;
double wh=w/sub.h;
double r1=0.03891*pow(sub.er,1.4);
double r2=0.267*pow(wh,7);
double r3=4.766*exp(-3.228*pow(wh,0.641));
double r4=0.016+pow(0.0514*sub.er,4.524);
double r5=pow(freq*sub.h*1e-6/28.843,12);
double r6=22.20*pow(wh,1.92);
if (r1>50.0)
{r7=1.206;
}
if (r2>50.0)
{r7=1.206-0.3144*exp(-r1);
}
if ((r1<=50.0) && (r2<=50.0))
```

```
{r7=1.206-0.3144*exp(-r1)*(1-exp(-r2));
}
double r8=1+1.275*(1-exp(-0.004625*r3*pow(sub.er,1.674)
   *pow(freq*sub.h*1e-6/18.365,2.745)));
if (r6>50.0)
{r9=0.0;
}else
{r9=5.086*r4*(r5/(0.3838+0.386*r4))*(exp(-r6)
   /(1+1.2992*r5))*(pow(sub.er-1,6)
         /(1+10*pow(sub.er-1,6)));
}
double r10=0.00044*pow(sub.er,2.136)+0.0184;
double r11=pow(freq*sub.h*1e-6/19.47,6)
   /(1+0.0962*pow(freq*sub.h*1e-6/19.47,6));
double r12=1/(1+0.00245*pow(wh,2));
double r13=0.9408*pow(Erf,r8)-0.9603;
double r14=(0.9408-r9)*pow(Er0,r8)-0.9603;
double r15=0.707*r10*pow(freq*sub.h*1e-6/12.3,1.097);
double r16=1.0+0.0503*sqr(sub.er)*r11*(1-exp(-pow(wh/15,6)));
double r17=r7*(1-1.241*(r12/r16)*exp(-0.026
   *pow(freq*sub.h*1e-6,1.15656)-r15));
return ans=Zc0*pow(r13/r14,r17);
}
//*********************************************
// FUNCTION: Effective Line Extension
//*********************************************
double F_lext(SUBSTRATE sub,PATCH_DIMS patch,PATCH_DATA pdata)
{double wh=patch.w/sub.h;
double Ci1=0.434907*((pow(pdata.Erf,0.81)+0.26)
   /(pow(pdata.Erf,0.81)-0.189))
         *((pow(wh,0.8544)+0.236)/(pow(wh,0.8544)+0.87));
double Ci2=1+(pow(wh,0.371)/(2.358*sub.er+1));
double Ci3=1+((0.5274*atan(0.084*pow(wh,1.9413/Ci2)))
   /pow(pdata.Erf,0.9236));
double Ci4=1+0.0377*atan(0.067*pow(wh,1.456))
   *(6-5*exp(0.036*(1-sub.er)));
double Ci5=1-0.218*exp(-7.5*wh);
double answer;
return answer=sub.h*Ci1*Ci3*Ci5/Ci4;
}
//************************
// FUNCTION: Ereff(f)
//************************
double F_ER_freq(SUBSTRATE sub,double w,double wt
   ,double fn,double Er0)
{double u=(w+((wt-w)/sub.er))/sub.h;
double p4=1+2.751*(1-exp(-pow(sub.er/15.916,8)));
double p3=0.0363*exp(-4.6*u)*(1-exp(-pow(fn/38.7,4.97)));
double p2=0.33622*(1-exp(-1*0.03442*sub.er));
double p1=0.27488+u*(0.6315+(0.525/pow(1+0.0157*fn,20)))
   -0.065683*exp(-8.7513*u);
double p=p1*p2*pow(((0.1844+p3*p4)*fn),1.5763);
double answer;
return answer=sub.er-((sub.er-Er0)/(1+p));
```

```
}
//***************************
// FUNCTION: Ereff(0)
//***************************
double F_ER_static(SUBSTRATE sub,double w)
{double wh=w/sub.h;
double b=0.564*exp((-0.2)/(sub.er+0.3));
double a=1+(1/49)*log((pow(wh,4)+pow(wh/52,2))/(pow(wh,4)+0.432))
   +(1/18.7)*log(1+pow(wh/18.1,3));
double g=pow((1+10/wh),-a*b)-(log(4)/PI)*(sub.t/sqrt(w*sub.h));
double answer;
return answer=((sub.er+1)/2)+((sub.er-1)/2)*g;
}
//***************************
// FUNCTION: Weff(0)
//***************************
double F_W_static(SUBSTRATE sub,double wt)
{double f=6+(2*PI-6)*exp((-4*pow(PI,2)/3)*pow((sub.h/wt),(3/4)));
double answer;
return answer=(2*PI*sub.h)/log((sub.h*f/wt)
   +sqrt(1+pow((2*sub.h/wt),2)));
}
```

A.3 User Supplied TL-Model Parameters File

PATCH ANTENNA DATA BLOCK

Patch Length:
4.064e-3

Patch Width:
6.985e-3

Feed Width:
457e-6

TEST FREQUENCY DATA BLOCK

Maximum Frequency:
20e9

Minimum Frequency:
16e9

Data Points:
40.0

MICROSTRIP SUBSTRATE DATA BLOCK

Dielectric Constant:
3.38

Substrate Thickness:
0.8128e-3

Conductor Thickness:
17.0e-6

Conductor Conductivity:
55.6e6

Ground Plane Conductivity:
55.6e6

Loss Tangent:
0.005

Conductor Surface Roughness:
3.5e-6

Ground Plane Conductor Roughness:
1.7e-6

Microstrip Line Length:

5.08e-3

Line Width:
0.457e-6

A.4 User Defined Math Functions

```
#include <math.h>
#include<iostream.h>
#define ACC 40.0
#define BIGNO 1.0e10
#define BIGNI 1.0e-10
// GLOBAL CONSTANTS
const double PI=acos(-1.0);
const double pi=PI;
const double TINY=1e-20;
// COMPLEX VARIABLE TYPE CAST
typedef struct FCOMPLEX {double r,i;} fcomplex;
//Complexing Two Real Numbers
fcomplex Complex(double re,double im)
{fcomplex c;
c.r=re;
c.i=im;
return c;
}
// Conjugating A Complex Number
fcomplex conjugate(fcomplex z)
{return Complex(z.r,-z.i);
}
// Addition Operator Overloading
fcomplex operator+(fcomplex a1, fcomplex a2)
{ return Complex(a1.r+a2.r, a1.i+a2.i);
}
fcomplex operator+(fcomplex a1, double a2)
{return Complex(a1.r+a2, a1.i);
}
fcomplex operator+(double a1, fcomplex a2)
{ return Complex(a2.r+a1, a2.i);
}
// Subtraction Operator Overloading
fcomplex operator-(fcomplex a1, fcomplex a2)
{ return Complex(a1.r-a2.r, a1.i-a2.i);
}
fcomplex operator-(fcomplex a1, double a2)
{ return Complex(a1.r-a2, a1.i);
}
fcomplex operator-(double a1, fcomplex a2)
{ return Complex(a1-a2.r, -a2.i);
}
fcomplex operator-(fcomplex a1)
{ return Complex(-a1.r, -a1.i);
}
// Multiplication Operator Overloading
fcomplex operator*(fcomplex a1, fcomplex a2)
{ return Complex(a1.r*a2.r-a1.i*a2.i, a1.i*a2.r+a1.r*a2.i);
}
```

```
fcomplex operator*(fcomplex a1, double a2)
{ return Complex(a1.r*a2, a1.i*a2);
}
fcomplex operator*(double a1, fcomplex a2)
{ return Complex(a2.r*a1, a2.i*a1);
}

// Division Operator Overloading
fcomplex operator/(fcomplex a1, fcomplex a2)
{ double r,den;
if (fabs(a2.r) >= fabs(a2.i))
{ r=a2.i/a2.r;
den=a2.r+r*a2.i;
return Complex((a1.r+r*a1.i)/den,(a1.i-r*a1.r)/den);
}else
{ r=a2.r/a2.i;
den=a2.i+r*a2.r;
return Complex((a1.r*r+a1.i)/den,(a1.i*r-a1.r)/den);
}
}
fcomplex operator/(fcomplex a1, double a2)
{ return Complex(a1.r/a2,a1.i/a2);
}
fcomplex operator/(double a1, fcomplex a2)
{ double r,den;
if(fabs(a2.r) >= fabs(a2.i))
{ r=a2.i/a2.r;
den=a2.r+r*a2.i;
return Complex((a1)/den,(-r*a1)/den);
}else
{ r=a2.r/a2.i;
den=a2.i+r*a2.r;
return Complex((a1*r)/den,(-a1)/den);
}
}

// Absolute Value Of Complex Numbers
double cabs(fcomplex z)
{ double x,y,ans,temp;
x=fabs(z.r);
y=fabs(z.i);
if (x == 0.0)
ans=y;
else if (y == 0.0)
 ans=x;
else if (x > y) {
 temp=y/x;
ans=x*sqrt(1.0+temp*temp);
}else
{ temp=x/y;
ans=y*sqrt(1.0+temp*temp);
}
return ans;
}
```

```
// Arguement Of Complex Numbers
double carg(fcomplex z)
{ double ans;
if (z.r==0.0)
{ if (z.i>0.0)
{ ans=PI/2.0;
}else if (z.i<0.0)
{ ans=-PI/2.0;
}else if (z.i==0.0)
{ ans=0.0;
}
}
else if (z.i==0.0)
{ if (z.r>0.0)
{ ans=0.0;
}
if (z.r<0.0)
{ ans=PI;
}
}else if ((z.r!=0.0)&&(z.i!=0.0))
{ if ((z.r<0.0)&&(z.i>0.0))
{ ans=atan(z.i/z.r)+PI;
}else if ((z.r<0.0)&&(z.i<0.0))
{ ans=atan(z.i/z.r)-PI;
}else if (z.r>0.0)
{ ans=atan(z.i/z.r);
}
}
return ans;
}
// Square Of Complex Numbers */
fcomplex sqr(fcomplex z)
{ fcomplex ans;
ans=z*z;
return ans;
}
// Square Of Double Numbers*/
double sqr(double z)
{double ans;
ans=z*z;
return ans;
}
// Square Root Of Complex Numbers*/
fcomplex sqrt(fcomplex z)
{ double x,y,w,r;
double cre,cim;
if ((z.r == 0.0) && (z.i == 0.0))
{ return Complex(0.0,0.0);
}else
{x=fabs(z.r);
y=fabs(z.i);
if (x >= y)
{ r=y/x;
w=sqrt(x)*sqrt(0.5*(1.0+sqrt(1.0+r*r)));
```

```
} else
{r=x/y;
w=sqrt(y)*sqrt(0.5*(r+sqrt(1.0+r*r)));
}
if (z.r >= 0.0)
{cre=w;
cim=z.i/(2.0*w);
}else
{cim=(z.i>=0.0)?w:-w;
cre=z.i/(2.0*cim);
}
return Complex(cre,cim);
}
}
// Complex Exponential
fcomplex exp(fcomplex a)
{ double r1,r2,im1;
r1=exp(a.r);
r2=cos(a.i);
im1=sin(a.i);
return Complex(r1*r2,r1*im1);
}
// Complex Natural Logarithm
fcomplex log(fcomplex a)
{ double re,im;
re=log(cabs(a));
im=carg(a);
return Complex(re,im);
}
// Complex Logarithm Base 10
fcomplex log10(fcomplex a)
{ double re,im;
re=log10(cabs(a));
im=log10(exp(carg(a)));
return Complex(re,im);
}
// Bessel Function J0
double bessj0(double x)
{ double ax,z;
double xx,y,ans,ans1,ans2;
if ((ax=fabs(x)) < 8.0)
{ y=x*x;
ans1=57568490574.0+y*(-13362590354.0+y*(651619640.7
+y*(-11214424.18+y*(77392.33017+y*(-184.9052456)))));
ans2=57568490411.0+y*(1029532985.0+y*(9494680.718
+y*(59272.64853+y*(267.8532712+y*1.0))));
ans=ans1/ans2;
} else
{ z=8.0/ax;
y=z*z;
xx=ax-0.785398164;
ans1=1.0+y*(-0.1098628627e-2+y*(0.2734510407e-4
+y*(-0.2073370639e-5+y*0.2093887211e-6)));
ans2 = -0.1562499995e-1+y*(0.1430488765e-3
```

```
+y*(-0.6911147651e-5+y*(0.7621095161e-6
-y*0.934935152e-7)));
ans=sqrt(0.636619772/ax)*(cos(xx)*ans1-z*sin(xx)*ans2);
}
return ans;
}
// Bessel Function J1
double bessj1(double x)
{ double ax,z;
double xx,y,ans,ans1,ans2;
if ((ax=fabs(x)) < 8.0)
{ y=x*x;
ans1=x*(72362614232.0+y*(-7895059235.0+y*(242396853.1
+y*(-2972611.439+y*(15704.48260+y*(-30.16036606))))));
ans2=144725228442.0+y*(2300535178.0+y*(18583304.74
+y*(99447.43394+y*(376.9991397+y*1.0))));
ans=ans1/ans2;
} else
{ z=8.0/ax;
y=z*z;
xx=ax-2.356194491;
ans1=1.0+y*(0.183105e-2+y*(-0.3516396496e-4
+y*(0.2457520174e-5+y*(-0.240337019e-6))));
ans2=0.04687499995+y*(-0.2002690873e-3
+y*(0.8449199096e-5+y*(-0.88228987e-6
+y*0.105787412e-6)));
ans=sqrt(0.636619772/ax)*(cos(xx)*ans1-z*sin(xx)*ans2);
if (x < 0.0) ans = -ans;
}
return ans;
}
// Bessel Function Jn
double bessj(int n,double x)
{ int j,jsum,m;
double ax,bj,bjm,bjp,sum,tox,ans;
ax=fabs(x);
if (ax == 0.0)
return 0.0;
else if (ax > (double) n)
{ tox=2.0/ax;
bjm=bessj0(ax);
bj=bessj1(ax);
for (j=1;j<n;j++)
{ bjp=j*tox*bj-bjm;
bjm=bj;
bj=bjp;
}
ans=bj;
} else
{tox=2.0/ax;
m=2*((n+(int) sqrt(ACC*n))/2);
jsum=0;
bjp=ans=sum=0.0;
bj=1.0;
```

```
for (j=m;j>0;j--)
{bjm=j*tox*bj-bjp;
bjp=bj;
bj=bjm;
if (fabs(bj) > BIGNO)
{bj *= BIGNI;
bjp *= BIGNI;
ans *= BIGNI;
sum *= BIGNI;
}
if (jsum) sum += bj;
jsum=!jsum;
if (j == n) ans=bjp;
}
sum=2.0*sum-bj;
ans /= sum;
}
return  x < 0.0 && n%2 == 1 ? -ans : ans;
}
// Bessel Function Y0
double bessy0(double x)
{double z;
double xx,y,ans,ans1,ans2;
if (x < 8.0)
{y=x*x;
ans1 = -2957821389.0+y*(7062834065.0+y*(-512359803.6
+y*(10879881.29+y*(-86327.92757+y*228.4622733))));
ans2=40076544269.0+y*(745249964.8+y*(7189466.438
+y*(47447.26470+y*(226.1030244+y*1.0))));
ans=(ans1/ans2)+0.636619772*bessj0(x)*log(x);
} else
{z=8.0/x;
y=z*z;
xx=x-0.785398164;
ans1=1.0+y*(-0.1098628627e-2+y*(0.2734510407e-4
+y*(-0.2073370639e-5+y*0.2093887211e-6)));
ans2 = -0.1562499995e-1+y*(0.1430488765e-3
+y*(-0.6911147651e-5+y*(0.7621095161e-6
+y*(-0.934945152e-7))));
ans=sqrt(0.636619772/x)*(sin(xx)*ans1+z*cos(xx)*ans2);
}
return ans;
}
// Bessel Function Y1
double bessy1(double x)
{double z;
double xx,y,ans,ans1,ans2;
if (x < 8.0)
{ y=x*x;
ans1=x*(-0.4900604943e13+y*(0.1275274390e13
+y*(-0.5153438139e11+y*(0.7349264551e9
+y*(-0.4237922726e7+y*0.8511937935e4)))));
ans2=0.2499580570e14+y*(0.4244419664e12
+y*(0.3733650367e10+y*(0.2245904002e8
```

```
+y*(0.1020426050e6+y*(0.3549632885e3+y)))));
ans=(ans1/ans2)+0.636619772*(bessj1(x)*log(x)-1.0/x);
} else
{ z=8.0/x;
y=z*z;
xx=x-2.356194491;
ans1=1.0+y*(0.183105e-2+y*(-0.3516396496e-4
+y*(0.2457520174e-5+y*(-0.240337019e-6))));
ans2=0.04687499995+y*(-0.2002690873e-3
+y*(0.8449199096e-5+y*(-0.88228987e-6
+y*0.105787412e-6)));
ans=sqrt(0.636619772/x)*(sin(xx)*ans1+z*cos(xx)*ans2);
}
return ans;
}
// Bessel Function Yn
double bessy(int n,double x)
{ int j;
double by,bym,byp,tox;
tox=2.0/x;
by=bessy1(x);
bym=bessy0(x);
for (j=1;j<n;j++)
{ byp=j*tox*by-bym;
bym=by;
by=byp;
}
return by;
}
// Hankel_0 Function Order 0
fcomplex Hankel_0(double a)
{ return Complex(bessj0(a),bessy0(a));
}
// Complex Argument Sine Function
fcomplex sin(fcomplex a1)
{ fcomplex ans;
ans=((exp(Complex(0.0,1.0)*a1)-exp(Complex(0.0,1.0)*-a1))
/Complex(0.0,2.0));
return ans;
}
// Complex Argument Cosine Function
fcomplex cos(fcomplex a1)
{ fcomplex ans;
ans=( (exp(Complex(0.0,1.0)*a1)+exp(Complex(0.0,1.0)*-a1))/2.0 );
return ans;
}
// Complex Argument Tangent Function
fcomplex tan(fcomplex a1)
{ fcomplex ans;
ans=( sin(a1)/cos(a1) );
return ans;
}
// Complex Argument Cotangent Function
double cot(double a1)
```

```
{ double ans;
ans=( cos(a1)/sin(a1) );
return ans;
}
// Complex Argument Cotangent Function
fcomplex cot(fcomplex a1)
{ fcomplex ans;
ans=(cos(a1)/sin(a1));
return ans;
}
// Double Argument Cosecant Function
double csc(double a)
{ double ans;
ans=1.0/sin(a);
return ans;
}
// Complex Argument Cosecant Function
fcomplex csc(fcomplex a)
{ fcomplex ans;
ans=1.0/sin(a);
return ans;
}
// Double Argument Secant Function
double sec(double a)
{ double ans;
ans=1.0/cos(a);
return ans;
}
// Complex Argument Secant Function
fcomplex sec(fcomplex a)
{ fcomplex ans;
ans=1.0/cos(a);
return ans;
}
//XXXXXXXXXXXXXXXXXXXXXXXXXXXXXXXXXXXXXX
// Complex Argument Inverse Sine Function
//XXXXXXXXXXXXXXXXXXXXXXXXXXXXXXXXXXXXXX
fcomplex asin(fcomplex a)
{ fcomplex ans;
ans=Complex(0.0,-1.0)*log(Complex(0.0,1.0)*a+sqrt(1.0-sqr(a)));
return ans;
}
// Complex Arqument Inverse Cosine Function
fcomplex acos(fcomplex a)
{ fcomplex ans;
ans=Complex(0.0,-1.0)*log(a+Complex(0.0,1.0)*sqrt(1.0-sqr(a)));
return ans;
}
// Complex Argument Inverse Tangent Function
fcomplex atan(fcomplex a)
{ fcomplex ans;
ans=Complex(0.0,0.5)*log((Complex(0.0,1.0)+a)/(Complex(0.0,1.0)-a));
return ans;
}
```

```
//XXXXXXXXXXXXXXXXXXXXXXXXXXXXXXXXXXXXXXXX
// Double Argument Hyperbolic Sine Function
//XXXXXXXXXXXXXXXXXXXXXXXXXXXXXXXXXXXXXXXX
double sinh(double a1)
{ double ans;
ans=( (exp(a1)-exp(-a1))/2.0  );
return ans;
}
//XXXXXXXXXXXXXXXXXXXXXXXXXXXXXXXXXXXXXXXXX
// Complex Argument Hyperbolic Sine Function
//XXXXXXXXXXXXXXXXXXXXXXXXXXXXXXXXXXXXXXXXX
fcomplex sinh(fcomplex a1)
{ fcomplex ans;
ans=( (exp(a1)-exp(-a1))/2.0  );
return ans;
}
//XXXXXXXXXXXXXXXXXXXXXXXXXXXXXXXXXXXXXXXXX
// Double Argument Hyperbolic Cosine Function
//XXXXXXXXXXXXXXXXXXXXXXXXXXXXXXXXXXXXXXXXX
double cosh(double a1)
{ double ans;
ans=( (exp(a1)+exp(-a1))/2.0  );
return ans;
}
//XXXXXXXXXXXXXXXXXXXXXXXXXXXXXXXXXXXXXXXXX
// Complex Argument Hyperbolic Cosine Function
//XXXXXXXXXXXXXXXXXXXXXXXXXXXXXXXXXXXXXXXXX
fcomplex cosh(fcomplex a1)
{ fcomplex ans;
ans=( (exp(a1)+exp(-a1))/2.0  );
return ans;
}
//XXXXXXXXXXXXXXXXXXXXXXXXXXXXXXXXXXXXXXXXX
// Double Argument Hyperbolic Tangent Function
//XXXXXXXXXXXXXXXXXXXXXXXXXXXXXXXXXXXXXXXXX
double tanh(double a1)
{ double ans;
ans=( sinh(a1)/cosh(a1)  );
return ans;
}
//XXXXXXXXXXXXXXXXXXXXXXXXXXXXXXXXXXXXXXXXX
// Complex Argument Hyperbolic Tangent Function
//XXXXXXXXXXXXXXXXXXXXXXXXXXXXXXXXXXXXXXXXX
fcomplex tanh(fcomplex a1)
{ fcomplex ans;
ans=( sinh(a1)/cosh(a1)  );
return ans;
}
//XXXXXXXXXXXXXXXXXXXXXXXXXXXXXXXXXXXXXXXXX
// Double Argument Hyperbolic Cotangent Function
//XXXXXXXXXXXXXXXXXXXXXXXXXXXXXXXXXXXXXXXXX
double coth(double a1)
{ double ans;
ans=( cosh(a1)/sinh(a1)  );
```

```
return ans;
}
//XXXXXXXXXXXXXXXXXXXXXXXXXXXXXXXXXXXXXXXX
// Complex Argument Hyperbolic Cotangent Function
//XXXXXXXXXXXXXXXXXXXXXXXXXXXXXXXXXXXXXXXX
fcomplex coth(fcomplex a1)
{ fcomplex ans;
ans=( cosh(a1)/sinh(a1) );
return ans;
}
//XXXXXXXXXXXXXXXXXXXXXXXXXXXXXXXXXXXXXXXX
// Double Argument Hyperbolic Cosecant Function
double csch(double a)
{ double ans;
ans=1.0/sinh(a);
return ans;
}
//XXXXXXXXXXXXXXXXXXXXXXXXXXXXXXXXXXXXXXXX
// Complex Argument Hyperbolic Cosecant Function
fcomplex csch(fcomplex a)
{ fcomplex ans;
ans=1.0/sinh(a);
return ans;
}
// Double Argument Hyperbolic Secant Function
double sech(double a)
{ double ans;
ans=1.0/cosh(a);
return ans;
}
// Complex Argument Hyperbolic Secant Function
fcomplex sech(fcomplex a)
{ fcomplex ans;
ans=1.0/cosh(a);
return ans;
}
// Double Argument Inverse Hyperbolic Sine Function
double asinh(double a)
{ double ans;
ans=log( a+sqrt( sqr(a)+1.0 ) );
return ans;
}
// Double Inverse Hyperbolic Cosine Function
double acosh(double a)
{ double ans;
ans=log( a+sqrt( sqr(a)-1.0 ) );
return ans;
}
// Double Inverse Hyperbolic Tangent Function
double atanh(double a)
{ double ans;
ans=0.5*log( (1.0+a)/(1.0-a) );
return ans;
}
```

```
// Double Inverse Hyperbolic Cotangent Function
double acoth(double a)
{ double ans;
ans=0.5*log( (a+1.0)/(a-1.0) );
return ans;
}
// Double Inverse Hyperbolic Secant Function
double asech(double a)
{ double ans;
ans=log( (1.0+sqrt(1.0-sqr(a)) )/a );
return ans;
}
// Double Inverse Hyperbolic Cosecant Function
double acsch(double a)
{ double ans;
ans=log( (1.0+sqrt(1.0+sqr(a)) )/a );
return ans;
}
// Complex Argument Inverse Hyperbolic Sine Function
fcomplex asinh(fcomplex a)
{ fcomplex ans;
ans=log( a+sqrt( sqr(a)+1.0 ) );
return ans;
}
// Complex Argument Inverse Hyperbolic Cosine Function
fcomplex acosh(fcomplex a)
{ fcomplex ans;
ans=log( a+sqrt( sqr(a)-1.0 ) );
if (a.r<0.0)
{ ans=log( a-sqrt( sqr(a)-1.0 ) );
}else
{ ans=log( a+sqrt( sqr(a)-1.0 ) );
}
if (ans.r<0.0)
{ans.r=-ans.r;
ans.i=ans.i-PI;
}
return ans;
}
// Complex Arguement Inverse Hyperbolic Tangent Function
fcomplex atanh(fcomplex a)
{ fcomplex ans;
ans=0.5*log( (1.0+a)/(1.0-a) );
return ans;
}
// Complex Arguement Inverse Hyperbolic Cotangent Function
fcomplex acoth(fcomplex a)
{ fcomplex ans;
ans=0.5*log( (a+1.0)/(a-1.0) );
return ans;
}
// Complex Arguement Inverse Hyperbolic Secant Function
fcomplex asech(fcomplex a)
{ fcomplex ans;
```

```
ans=log( (1.0+sqrt(1.0-sqr(a)) )/a );
return ans;
}
// Complex Arguement Inverse Hyperbolic Cosecant Function
fcomplex acsch(fcomplex a)
{ fcomplex ans;
ans=log( (1.0+sqrt(1.0+sqr(a)) )/a );
return ans;
}
// Sinc Function
double sinc(double val)
{ if (fabs(val)<TINY)
{ return 1.0;
}else
{ return(sin(val)/val);
}
}
// Gaussian Quadrature Integrating Routine (5 Point)
double qgaus(double (*gaus_func)(double), double a, double b)
{ int j;
double xr,xm,dx,s;
static double  x[]={0.0,0.1488743389,0.4333953941,
0.6794095682,0.8650633666,0.97390652};
static double  w[]={0.0,0.2955242247,0.2692667193,
0.2190863625,0.1494513491,0.06667134};
xm=0.5*(b+a);
xr=0.5*(b-a);
s=0.0;
for (j=1;j<=5;j++)
{ dx=xr*x[j];
s += w[j]*((*gaus_func)(xm+dx)+(*gaus_func)(xm-dx));
}
return s *= xr;
}
// Si Integral Function
double Si(double x)
{ double integral,a;
a=0.0;
integral=qgaus(sinc,a,x);
return integral;
}
// Factorial Function
double fact(int index)
{  double ans;
if (index<0)
{cout<<"\n\nINVALID Factorial Index";
return -9.999e10;
}
if (index==0)
{ return ans=1;
}else
{ans=1;
for (int i=1; i<=index; i++)
{ans=ans*i;
```

```
}
return ans;
}
}
#undef ACC
#undef BIGNO
#undef BIGNI
```

Appendix B

Comparison of Simulation Results From Transmission Line Model, Ensemble MoM, and IE3D MoM

B.1 Microstrip Patch Analyzed In The Comparison

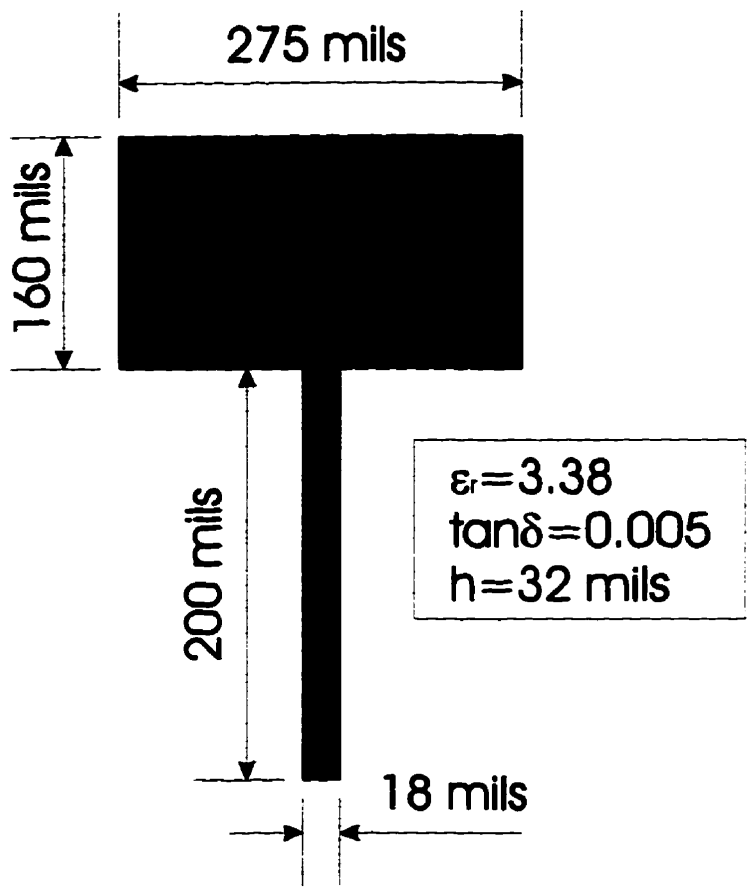

Figure B.1 Microstrip patch parameters used in the comparison

B.2 Transmission Line Model Results

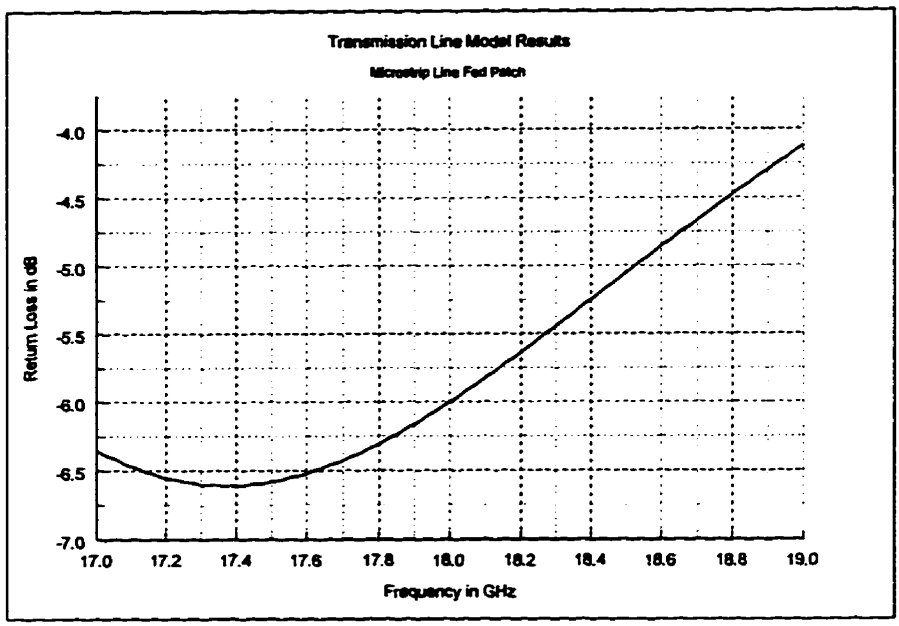

Figure B.2 Transmission line model return loss prediction

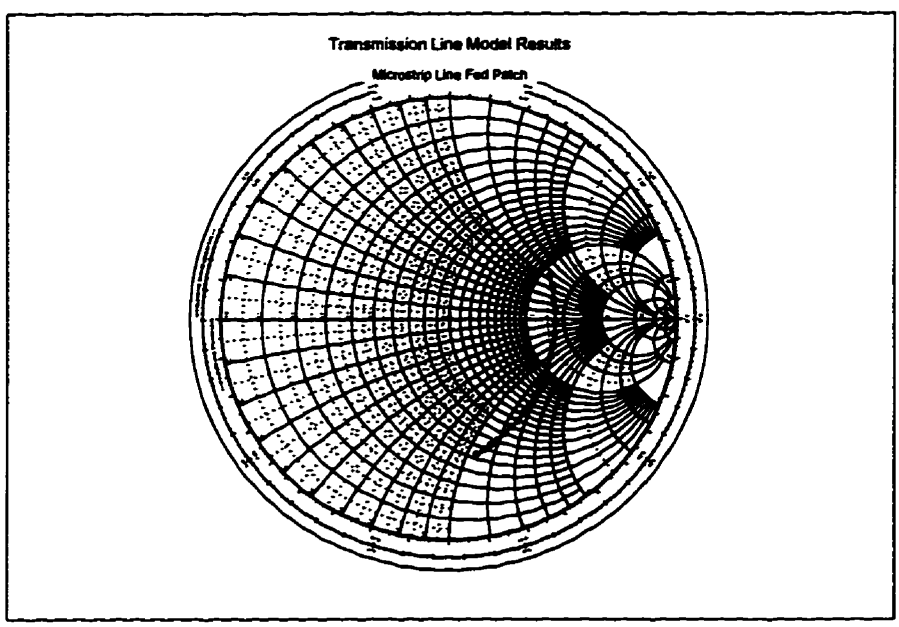

Figure B.3 Transmission line model input impedance prediction

B.3 Ensemble Simulation Results

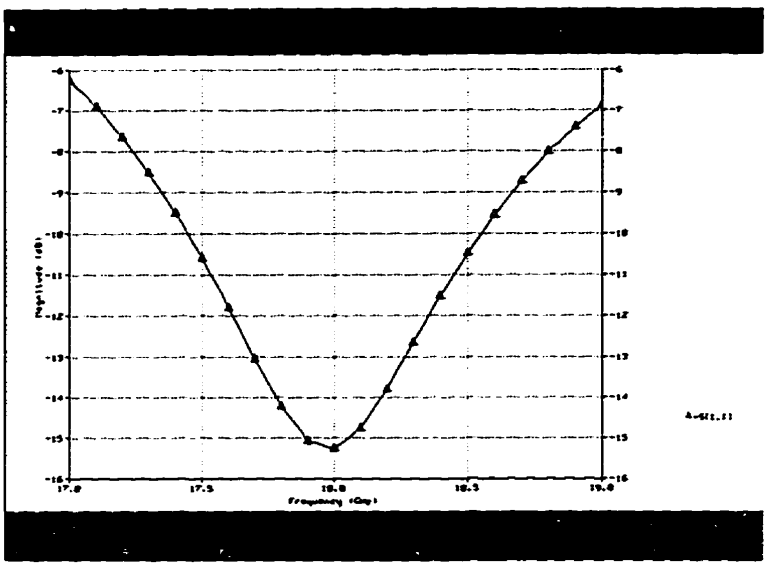

Figure B.4 Ensemble simulated results for return loss

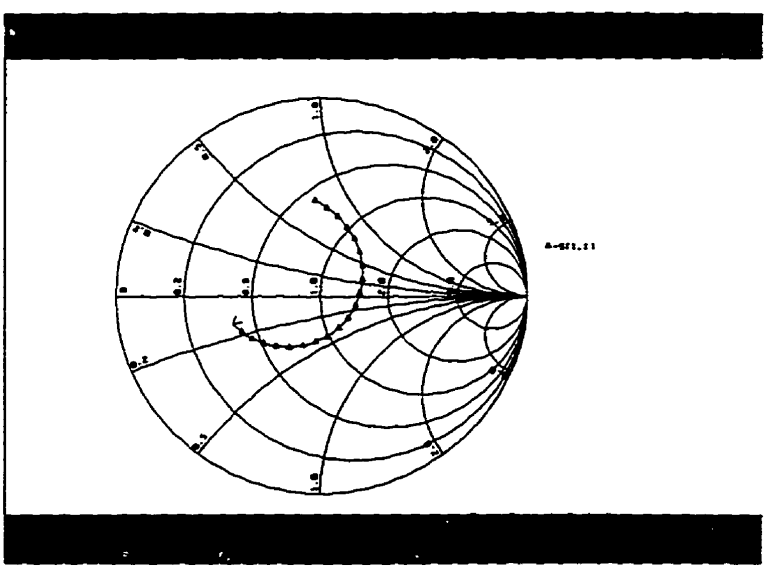

Figure B.5 Ensemble simulated input impedance

B.4 IE3D Simulation Results

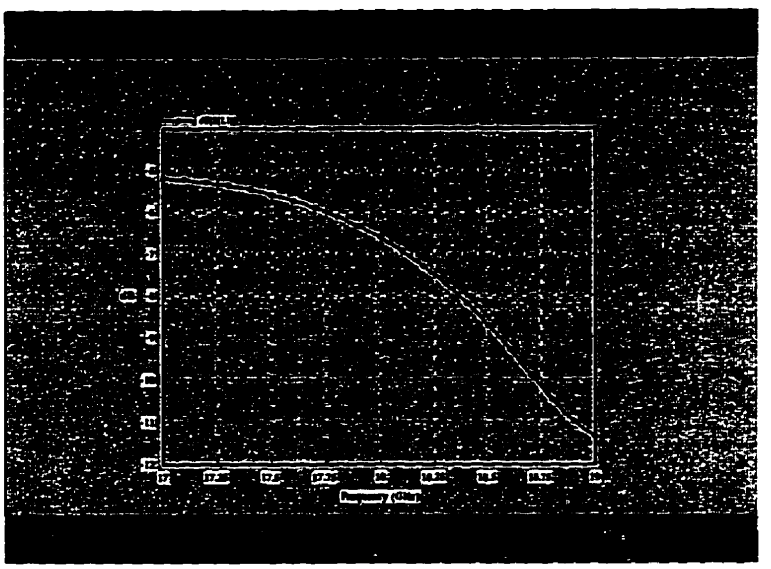

Figure B.6 IE3D simulated results for return loss

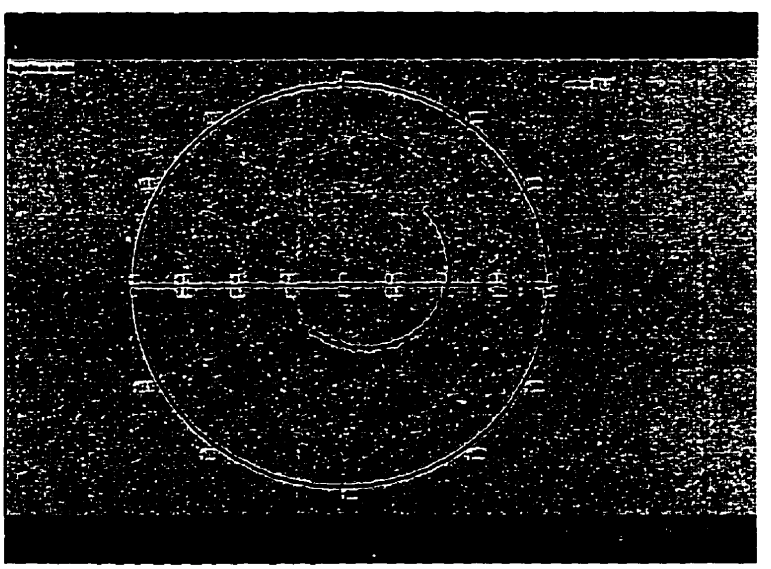

Figure B.7 IE3D simulated results for input impedance

Appendix C

C++ Computer Programs
for
Radiation Pattern Prediction
of
Microstrip Patch Antenna
and Antenna Arrays

C.1 Main Program for Radiation Pattern Prediction

```
// INCLUDED HEADER FILES
#include<iostream.h>
#include<fstream.h>
#include<math.h>
#include <io.h>
#include <stdio.h>
#include <stdlib.h>
#include "overload.h"

//#####GLOBAL CONSTANTS#####
const double PI=acos(-1);
const double EO=1e-9/(36*PI);
const double UO=4*PI*1e-7;
const double CO=1/sqrt(EO*UO);
const double NO=sqrt(UO/EO);
const double Ce=0.577216;
const double TINY=1e-10;
const int  MAXPATH=128;
const double pi=PI;

//#####GLOBAL VARIABLES#####
double k,w,h,l,freq,Weff,Leff;
double THETAmin, THETAmax;
double PHImax,PHImin;
static double THETAsav,PHIsav;
static double (*nearfunc)(double,double);
double Er=3.38;

//#####FUNCTION BLOCK#####
double testfunc(double,double);
double Etheta(double,double);
double Ephi(double ,double );
double Etotal(double ,double );
double SlotsAF(double , double );
double ElementPAT(double ,double );
double qgauss(double (*gauss_func)(double), double,double);
double quad2d(double (*func)(double,double),double x1, double x2);
double f1(double);
double f2(double);
double yy1(double);
double yy2(double);

double plane(double x,double y);
double UniformAF(int N, double x,double y);
double nonUniAF(int N, double x,double y);

// MAIN PROGRAM
int main()
{ofstream RAD_DATA("E4-uni.txt");
RAD_DATA.clear();
```

```
RAD_DATA.precision(6);
RAD_DATA.width(8);
double Prad;
double Dmax=0.0,THETAtest,PHItest,Dtest,Do;
int numTHETA=45,numPHI=4,i,j;
freq=17e9;
k=2*PI*freq/CO;      //sqrt(Er)*
h=203.6e-6;
w=7.0e-3;
l=3.9e-3;
Leff=l+h;
Weff=w+h;
THETAmin=0.0;
THETAmax=PI/2.0;  // Microstrip Radiates in Upper Half Space
PHImax=2*PI;
PHImin=0.0;
Prad=quad2d(testfunc,THETAmin,THETAmax);
for (j=0; j<=numPHI; j++)
PHItest=j*PHImax/numPHI;
for (i=0; i<=numTHETA; i++)
{THETAtest=i*THETAmax/numTHETA;
Dtest=4.0*PI*Etotal(THETAtest,PHItest)/Prad;
if(Dtest>=Dmax)
{Dmax=Dtest;
}
RAD_DATA<<THETAtest*180/PI<<"\t\t"
      <<PHItest*180/PI<<"\t\t"<<fabs(Dtest)<<'\n';
}
}
Do=Dmax;
cout << "\n\nPrad=" << Prad;
cout << "   Dmax=" << Dmax;
cout << "   Do=" << Do;
cout << "   Do(dB)=" << 10*log10(fabs(Do));
RAD_DATA.close();
return 0;
}
double testfunc(double b, double c)
{return sin(b)*Etotal(b,c);//sin(b) included spherical integration
}
double Etheta(double x,double y)
{double ans,YY,ZZ,a,b;
YY=0.5*k*Weff*sin(x)*sin(y);
ZZ=0.5*k*h*cos(x);
a=Weff*sinc(YY);
b=h*sinc(ZZ);
return ans=cos(y)*a*b;
}
double Ephi(double x,double y)
{double ans,YY,ZZ,a,b;
YY=0.5*k*Weff*sin(x)*sin(y);
ZZ=0.5*k*h*cos(x);
a=Weff*sinc(YY);
b=h*sinc(ZZ);
```

```
return ans=cos(x)*sin(y)*a*b;
}
/*
double Etotal(double x,double y)
{double ans;
return ans=ElementPAT(x,y);
}
*/
/*
double Etotal(double x,double y)
{double ans;
return ans=ElementPAT(x,y)*sqr(nonUniAF(4,x,y));
}
*/
double Etotal(double x,double y)
{double ans;
return ans=ElementPAT(x,y)*sqr(UniformAF(4,x,y));
}
double SlotsAF(double x,double y)
{double ans;
ans=2*cos(0.5*k*Leff*sin(x)*cos(y));//Along X-axis
return ans;
}
double ElementPAT(double x,double y)
{double ans;
ans=(sqr(Etheta(x,y))+sqr(Ephi(x,y)))*sqr(SlotsAF(x,y));
return ans;
}
/*
double plane(double x,double y)
{double ans,d;
d=12e-3;
ans=k*d*sin(x)*sin(y);// Y-Axis (AZIMUTH)
return ans;
}
*/
double plane(double x,double y)
{double ans,d;
d=12e-3;
ans=k*d*sin(x)*cos(y);// X-Axis (ELEVATION)
return ans;
}
double UniformAF(int N, double x,double y)
{double NN,ans;
NN=0.5*plane(x,y);
ans=sinc(N*NN);
return ans;
}
/*
double nonUniAF(int N, double x,double y)
{double AMP[]={0.0,1.0,0.636393,0.388034};
//int rem=N%2;
int j;
double NN,ans;
```

```
//if (rem==0)          //EVEN number of elements
//{
ans=0.0;
for (j=1; j<=N/2; j++)
{NN=((2.0*j-1.0)/2.0)*plane(x,y);
ans+=(AMP[j]*cos(NN));
}
return ans;
// }
}
*/
double nonUniAF(int N, double x,double y)
{double AMP[]={0.0,1.0,0.42678};
//int rem=N%2;
int j;
double NN,ans;
//  if (rem==0)          //EVEN number of elements
//{
ans=0.0;
for (j=1; j<=N/2; j++)
{NN=((2.0*j-1.0)/2.0)*plane(x,y);
ans+=(AMP[j]*cos(NN));
}
return ans;
//}
}
double quad2d(double (*func)(double,double),double x1, double x2)
{nearfunc=func;
return qgauss(f1,x1,x2);
}
double f1(double x)
{THETAsav=x;
return qgauss(f2,yy1(x),yy2(x));
}
double f2(double y)
{return (*nearfunc)(THETAsav,y);
}
// GAUSSIAN QUADRATURE (20-POINT)
double qgauss(double (*nearfunc)(double), double a, double b)
{int j;
double xr,xm,dx,s;
static float  x[]={0.0,0.076526521133497333755,0.22778585114164507808,
0.37370608871541956067,0.51086700195082709800,
0.63605368072651502545,0.74633190646015079261,
0.83911697182221882339,0.91223442825132590586,
0.96397192727791379126,0.99312859918509492478};
static float  w[]={0.0,0.15275338713072585069,0.14917298647260374678,
0.14209610931838205132,0.13168863844917662689,
0.11819453196151841731,0.10193011981724043503,
0.08327674157670474872,0.06267204833410906357,
0.04060142980038694133,0.01761400713915211831};
xm=0.5*(b+a);
xr=0.5*(b-a);
s=0.0;
```

```
for (j=1;j<=10;j++)
{dx=xr*x[j];
s += w[j]*((*nearfunc)(xm+dx)+(*nearfunc)(xm-dx));
return s *= xr;
// USER DEFINED INTEGRATION LIMITS
double yy1(double x)
{return PHImin;}
double yy2(double x)
{return PHImax;}
```

Appendix D

C++ Computer Programs
for the
Calculation of Linear Array
Taylor Line Source
Amplitude Weightings

D.1 Program for Taylor Line Source Amplitude Weightings

```
// INCLUDED HEADER FILES
#include<iostream.h>
#include<fstream.h>
#include<math.h>
#include <io.h>
#include <stdio.h>
#include <stdlib.h>
#include "overload.h"

//#####GLOBAL CONSTANTS#####
const double    PI=acos(-1);
const double    EO=1e-9/(36*PI);
const double    UO=4*PI*1e-7;
const double    CO=1/sqrt(EO*UO);
const double    NO=sqrt(UO/EO);

// MAIN PROGRAM
int main()
{ofstream AMP_DATA("amp_data.txt");
AMP_DATA.clear();
AMP_DATA.precision(6);
AMP_DATA.width(8);
int n;
double SLL=-25;//SLL in dB
double R=pow(10,(fabs(SLL)/20));// Side Lobe Voltage Ratio
int nTaylor=4;
int numberElem=6;
double dx=12e-3;
double LL=dx*(numberElem-1.0);
double Zorig=-LL/2;
double maxCurrent;
double *loc = new double[numberElem];
double *current = new double[numberElem];
double *normCurrent = new double[numberElem];
double freq=17e9;
double lambda=CO/freq;
cout<<"\n\t"<<freq<<"\t"<<lambda<<"\n";
double A=acosh(R)/PI;
double scale=nTaylor/sqrt(sqr(A)+sqr(nTaylor-0.5));
double *Un = new double[nTaylor];
double *Vn = new double[nTaylor];
double *NULLangles = new double[nTaylor];
double HPPbw=2*asin(((scale*lambda)/(LL*PI))
        *sqrt(sqr(acosh(R))-sqr(acosh(R/sqrt(2)))));
cout<<"\t"<<R<<"\t"<<SLL<<"\t"<<A<<"\t"<<scale<<"\t"<<(180/PI)*HPPbw<<"\n\n";
for (n=1; n<nTaylor; n++)
{Un[n]=PI*scale*sqrt(sqr(A)+sqr(n-0.5));
Vn[n]=Un[n]/PI;
cout<<"\t"<<n<<"\t"<<Vn[n]<<"\t\t"<<NULLangles[n]<<"\n";
}
```

```
double *SF= new double[nTaylor];
double summed;
double front,prod;
int p,m,pts,j;
cout<<"\n\n";
for (p=1; p<=nTaylor-1; p++)
{front=sqr(fact(nTaylor-1))/(fact(nTaylor-1+p)*fact(nTaylor-1-p));
prod=1.0;
for (m=1; m<=nTaylor-1; m++)
{prod=prod*(1-sqr(p/Vn[m]));
}
SF[p]=front*prod;
//cout<<"\t"<<front<<"\t"<<SF[p]<<"\n";
}
cout<<"\n\n";
for (pts=0;pts<numberElem;pts++)
{loc[pts]=Zorig+pts*dx;
summed=0;
for (j=1; j<=nTaylor-1; j++)
{summed=summed+SF[j]*cos(2*PI*j*loc[pts]/LL);
}
current[pts]=1+2*summed;
if (current[pts]>maxCurrent)
{maxCurrent=current[pts];
}
AMP_DATA<<loc[pts]<<"\t\t"<<current[pts]<<"\n";
}
AMP_DATA<<"\n\n\n\n";
for (pts=0;pts<numberElem;pts++)
{normCurrent[pts]=current[pts]/maxCurrent;
AMP_DATA<<loc[pts]<<"\t\t"<<normCurrent[pts]<<"\n";
cout<<loc[pts]<<"\t\t"<<normCurrent[pts]<<"\n";
}
AMP_DATA.close();
return 0;
}
```

Appendix E

Ensemble Simulation Results For The Microstrip Antenna Element Used In The Microstrip Array

E.1 Ensemble Simulated Antenna Element Results

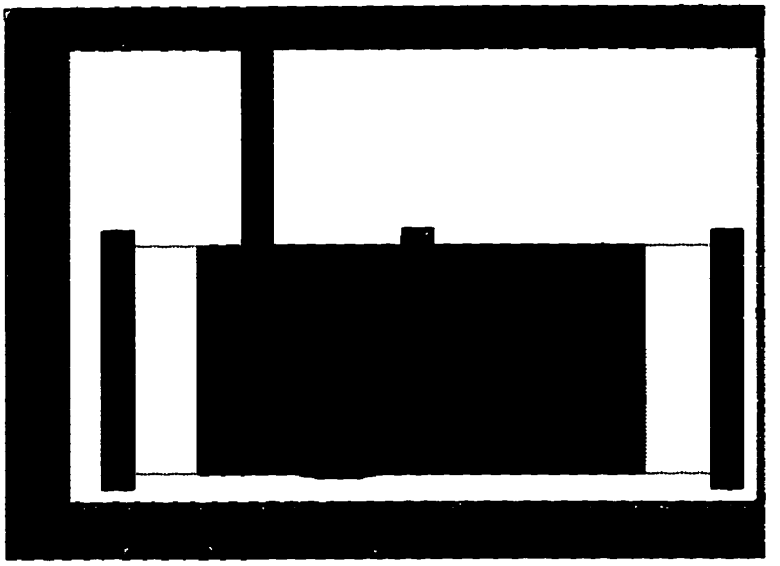

Figure E.1 Picture of the Ensemble simulated radiating element

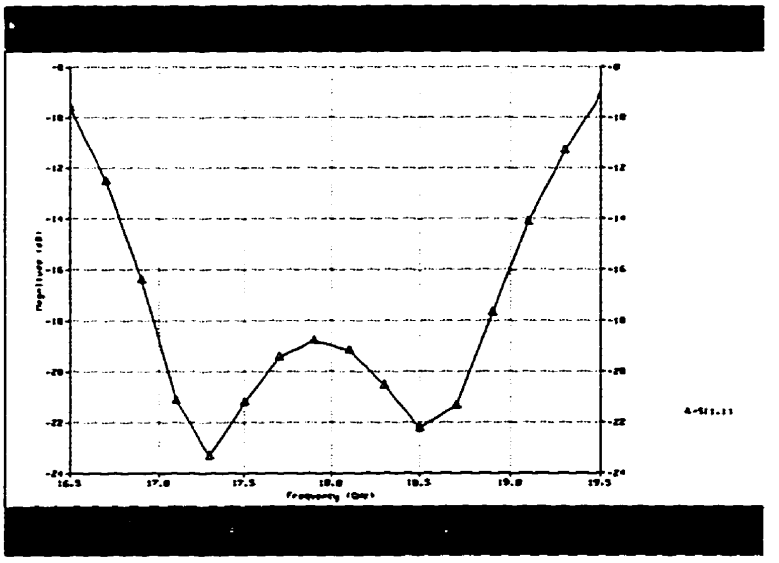

Figure E.2 Ensemble simulated element return loss

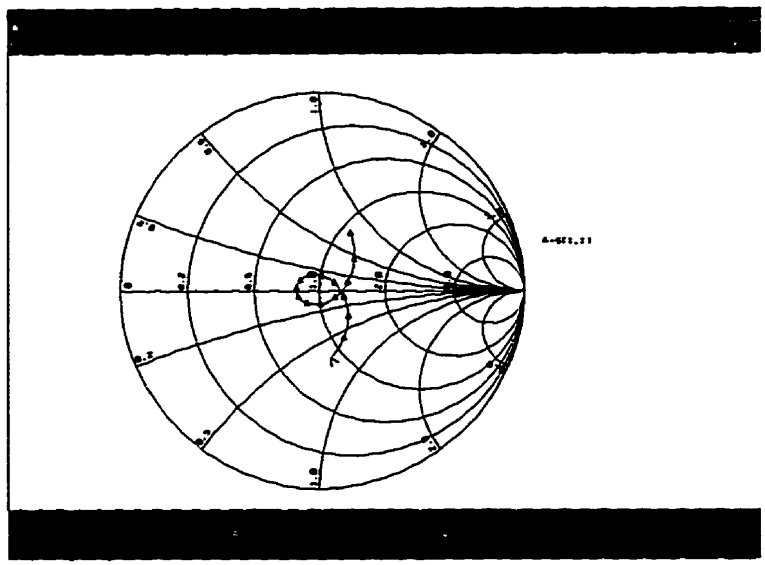

Figure E.3 Ensemble simulated element input impedance

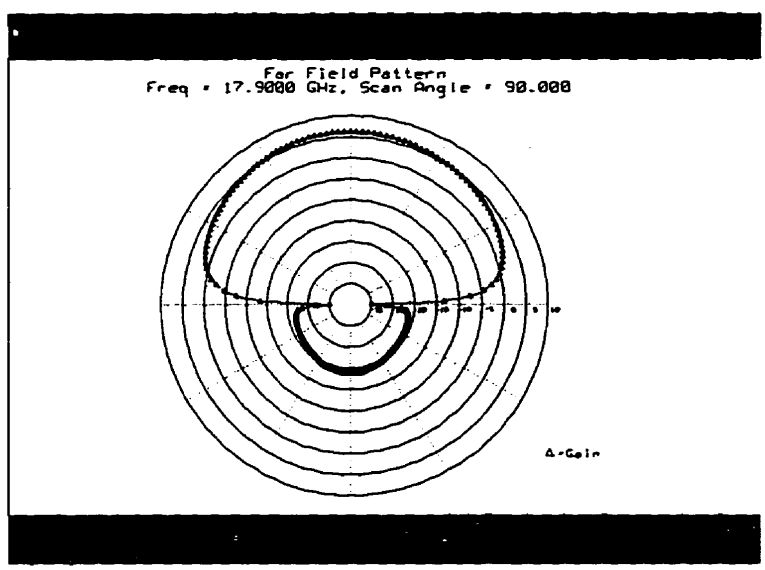

Figure E.4 Ensemble simulated element E-Plane radiation pattern

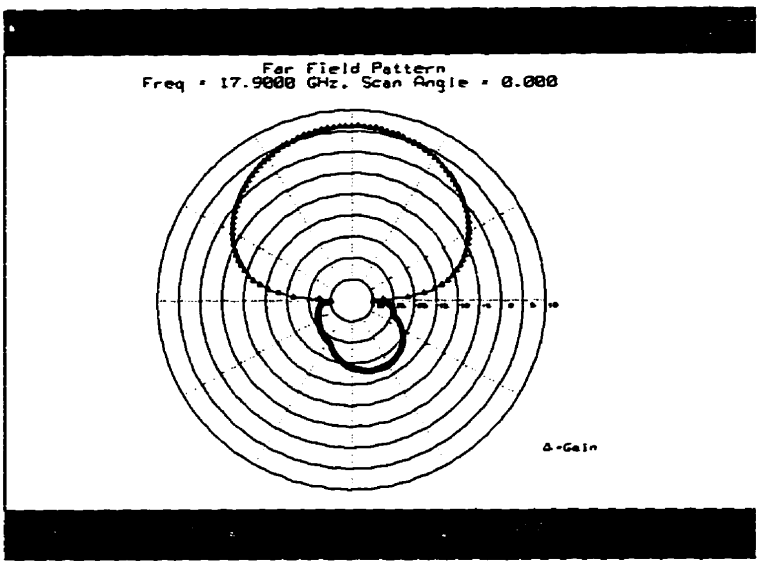

Figure E.5 Ensemble simulated element H-Plane radiation pattern

Appendix F

Mathcad Program
Used To Determine
The
Array Feed Network

F.1 Design of The 4-Element Sub-Array Feed Network

Ku-Band Sub-Array Feed Network Design

Index:

$$i = 1..4$$

Taylor Line Source Amplitude Weightings for 4-Element Sub-Array:

$$Magnitude_i =$$

0.185
0.43
0.43
1.0

Sub-Array Power Distribution:

$$Total\_Power = \sum_i Magnitud$$

$$Total\_Power = 2.045$$

$$Percent\_Total_i = \frac{Magnitude_i}{Total\_Power} \cdot 100$$

Percent_Tota

9.0465
21.0269
21.0269
48.8998

AB and CD Splitter:

Input Impedance;

$$Zabcd\_in = 50$$

Selected Branch Impedances

$$Zabcd\_hp = 35$$

Calculated Low-Side Impedances

$$Ratio\_ab = \frac{\sum_{j=1}^{2} Percent\_Total_j}{\sum_{j=1}^{4} Percent\_Total_j} \cdot 100$$

$$Ratio\_cd = \frac{\sum_{j=3}^{4} Percent\_Total_j}{\sum_{j=1}^{4} Percent\_Total_j} \cdot 100$$

$$Ratio\_ab = 30.0733$$

$$Ratio\_cd = 69.9267$$

$$Ratio\_ab\_to\_cd = \frac{Ratio\_a}{Ratio\_c}$$

$$Ratio\_ab\_to\_cd = 0.4301$$

$$Zabcd\_lp = \frac{Zabcd\_hp}{Ratio\_ab\_to\_c}$$

$$Zabcd\_lp = 81.3821$$

Calculated Junction Impedance:

$$Zjunc\_ABCD = \frac{1}{\left(\frac{1}{Zabcd\_hp} - \frac{1}{Zabcd\_lp}\right)}$$

$$Zjunc\_ABCD = 24.4743$$

Transformer Impedance Impedance:

$$Ztx\_ABCD = \sqrt{(Zjunc\_ABCD Zabcd\_in)}$$

$$Ztx\_ABCD = 34.9817$$

Power Into AB Arm:

$$AB\_dB = 10 \cdot \log\left(\frac{Ratio\_ab}{100}\right)$$

$$AB\_dB = -5.2182$$

Power Into CD Arm:

$$CD\_dB = 10 \cdot \log\left(\frac{Ratio\_cd}{100}\right)$$

$$CD\_dB = -1.5536$$

A and B Splitter:

Input Impedance;

$$Zab\_in = Zabcd\_l$$

$$Zab\_in = 81.3821$$

Selected Branch Impedances

$$Zab\_hp = 35$$

Calculated Low Power Side Impedance

$$Ratio\_a = \frac{Percent\_Total_1}{\sum_{j=1}^{2} Percent\_Total_j} \cdot 100$$

$$Ratio\_b = \frac{Percent\_Total_2}{\sum_{j=1}^{2} Percent\_Total_j} \cdot 100$$

$$Ratio\_a = 30.0813$$

$$Ratio\_b = 69.9187$$

$$Ratio\_a\_to\_b = \frac{Ratio\_}{Ratio\_}$$

$$Ratio\_a\_to\_b = 0.4302$$

$$Zab\_lp = \frac{Zab\_hp}{Ratio\_a\_to\_}$$

$$Zab\_lp = 81.3514$$

Calculated Junction Impedance:

$$Zjunc\_AB = \frac{1}{\left(\frac{1}{Zab\_hp} + \frac{1}{Zab\_lp}\right)}$$

$$Zjunc\_AB = 24.4715$$

Transformer Impedance Impedance:

$$Ztx\_AB = \sqrt{(Zjunc\_ABZab\_in)}$$

$$Ztx\_AB = 44.6267$$

Power Into A Arm:

$$A\_dB = 10 \cdot \log\left(\frac{Ratio\_a}{100}\right)$$

$$A\_dB = -5.217$$

Power Into B Arm:

$$B\_dB = 10 \cdot \log\left(\frac{Ratio\_b}{100}\right)$$

$$B\_dB = -1.5541$$

Output Transformer for A Arm:

$$ZA\_tx = \sqrt{(Zab\_lp \cdot 50)}$$

$$ZA\_tx = 63.7775$$

Output Transformer for B Arm:

$$ZB\_tx = \sqrt{(Zab\_hp \cdot 50)}$$

$$ZB\_tx = 41.833$$

C and D Splitter:

Input Impedance;

$$Zcd\_in = Zabcd\_hp$$

$$Zcd\_in = 35$$

Selected High-Side Impedances

$$Zcd\_hp = 35$$

Calculated Low Power Side Impedance

$$Ratio\_c = \frac{Percent\_Total_3}{\sum_{j=3}^{4} Percent\_Total_j} \cdot 100$$

$$Ratio\_d = \frac{Percent\_Total_4}{\sum_{j=3}^{4} Percent\_Total_j} \cdot 100$$

$$Ratio\_c = 30.0699$$

$$Ratio\_d = 69.9301$$

$$Ratio\_c\_to\_d = \frac{Ratio\_}{Ratio\_}$$

$$Ratio\_c\_to\_d = 0.43$$

$$Zcd\_lp = \frac{Zab\_hp}{Ratio\_c\_to\_}$$

$$Zcd\_lp = 81.3953$$

Calculated Junction Impedance:

$$Zjunc\_CD = \frac{1}{\left(\frac{1}{Zcd\_hp} + \frac{1}{Zcd\_lp}\right)}$$

$$Zjunc\_CD = 24.4755$$

Transformer Impedance Impedance:

$$Ztx\_CD = \sqrt{(Zjunc\_CD \cdot Zcd\_in)}$$

$$Ztx\_CD = 29.2685$$

Power Into A Arm:

$$C\_dB = 10 \cdot \log\left(\frac{Ratio\_c}{100}\right)$$

$$C\_dB = -5.2187$$

Power Into B Arm:

$$D\_dB = 10 \cdot \log\left(\frac{Ratio\_d}{100}\right)$$

$$D\_dB = -1.5534$$

Output Transformer for C Arm:

$$ZC\_tx = \sqrt{(Zcd\_lp \cdot 50)}$$

$$ZC\_tx = 63.7947$$

Output Transformer for D Arm:

$$ZD\_tx = \sqrt{(Zcd\_hp \cdot 50)}$$

$$ZD\_tx = 41.833$$

Summary Of Sub-Array Feed Network

Splitter ABCD:

Zabcd_hp = 35

AB_dB = -5.2182

Zabcd_lp = 81.3821

CD_dB = -1.5536

Ztx_ABCD = 34.9817

Zabcd_in = 50

Splitter AB:

Zab_hp = 35

A_dB = -5.217

Zab_lp = 81.3514

B_dB = -1.5541

ZA_tx = 63.7775

ZB_tx = 41.833

Ztx_AB = 44.6267

Zab_in = 81.3821

Splitter CD:

Zcd_hp = 35

C_dB = -5.2187

Zcd_lp = 81.3953

D_dB = -1.5534

Ztx_CD = 29.2685

ZC_tx = 63.7947

ZD_tx = 41.833

Zcd_in = 35

F.2 Mathcad Predicted Lossless Feed Network Port Power Levels

Expected Feed Network Output Port Power Levels (*lossless approximation*):

4-Element Sub-Array Power Levels:

$$j := 1 .. 16$$

$$Port1 := A\_dB + AB\_d$$

$$Port2 := B\_dB + AB\_d$$

$$Port5 := C\_dB + CD\_dB$$

$$Port6 := D\_dB + CD\_dB$$

$$Port1 = -10.4352$$

$$Port2 = -6.7722$$

$$Port5 = -6.7722$$

$$Port6 = -3.1069$$

Full Array Power Levels:

$$j := 1 .. 16$$

$$Port_1 := A\_dB + AB\_dB - 6$$

$$Port_3 := B\_dB + AB\_dB - 6$$

$$Port_5 := C\_dB + CD\_dB - 6$$

$$Port_7 := D\_dB + CD\_dB - 6$$

$$Port_9 := C\_dB + CD\_dB - 6$$

$$Port_{11} := D\_dB + CD\_dB - 6$$

$$Port_{13} := A\_dB + AB\_dB - 6$$

$$Port_{15} := B\_dB + AB\_dB - 6$$

$$Port_2 := B\_dB + AB\_dB - 6$$

$$Port_4 := A\_dB + AB\_dB - 6$$

$$Port_6 := D\_dB + CD\_dB - 6$$

$$Port_8 = C\_dB - CD\_dB - 6$$

$$Port_{10} = D\_dB - CD\_dB - 6$$

$$Port_{12} = C\_dB - CD\_dB - 6$$

$$Port_{14} = B\_dB - AB\_dB - 6$$

$$Port_{16} = A\_dB - AB\_dB - 6$$

$$Port_1 = -16.4352$$

$$Port_2 = -12.7722$$

$$Port_3 = -12.7722$$

$$Port_4 = -16.4352$$

$$Port_5 = -12.7722$$

$$Port_6 = -9.1069$$

$$Port_7 = -9.1069$$

$$Port_8 = -12.7722$$

$$Port_9 = -12.7722$$

$$Port_{10} = -9.1069$$

$$Port_{11} = -9.1069$$

$$Port_{12} = -12.7722$$

$$Port_{13} = -16.4352$$

$$Port_{14} = -12.7722$$

$$Port_{15} = -12.7722$$

$$Port_{16} = -16.4352$$

j
1
2
3
4
5
6
7
8
9
10
11
12
13
14
15
16

$Port_j$
-16.4352
-12.7722
-12.7722
-16.4352
-12.7722
-9.1069
-9.1069
-12.7722
-12.7722
-9.1069
-9.1069
-12.7722
-16.4352
-12.7722
-12.7722
-16.4352

Verification That Power Level Definitions are Correct:

$$Verify\_Total\_Power = \sum_{j=1}^{16} 10^{\frac{Port_j}{10}}$$

Verify_Total_Power= 1.0048

F.3 Mathcad Predicted Lossy Feed Network Port Power Levels

Expected Feed Network Output Port Power Levels (*lossy approximation*):

Power Splitter Efficiency:

$$eff = 0.95$$

Splitter Losses Using Efficiency Approximation:

$$eff4 = eff$$

$$eff\_dB4 = 10 \cdot \log(eff4)$$

$$eff4 = 0.9025$$

$$eff\_dB4 = -0.4455$$

4-Element Sub-Array Power Levels:

$$j = 1 .. 16$$

$$Lossy_1 = Port1 + eff\_dB$$

$$Lossy_2 = Port2 + eff\_dB$$

$$Lossy_5 = Port5 + eff\_dB$$

$$Lossy_6 = Port6 + eff\_dB$$

$$Lossy_1 = -10.8807$$

$$Lossy_2 = -7.2178$$

$$Lossy_5 = -7.2178$$

$$Lossy_6 = -3.5525$$

Splitter Losses Using Efficiency Approximation:

$$eff16 = eff$$

$$eff\_dB16 = 10 \cdot \log(eff16)$$

$$eff16 = 0.8145$$

$$eff\_dB16 = -0.8911$$

Full Array Power Levels:

$$LPort_1 = Port_1 + eff\_dB1$$

$$LPort_3 = Port_3 + eff\_dB1$$

$$LPort_5 = Port_5 - eff\_dBl$$

$$LPort_7 = Port_7 - eff\_dBl$$

$$LPort_9 = Port_9 - eff\_dBl$$

$$LPort_{11} = Port_{11} - eff\_dBl$$

$$LPort_{13} = Port_{13} - eff\_dBl$$

$$LPort_{15} = Port_{15} - eff\_dBl$$

$$LPort_2 = Port_2 - eff\_dBl$$

$$LPort_4 = Port_4 - eff\_dBl$$

$$LPort_6 = Port_6 - eff\_dBl$$

$$LPort_8 = Port_8 - eff\_dBl$$

$$LPort_{10} = Port_{10} - eff\_dBl$$

$$LPort_{12} = Port_{12} - eff\_dBl$$

$$LPort_{14} = Port_{14} - eff\_dBl$$

$$LPort_{16} = Port_{16} - eff\_dBl$$

$$LPort_1 = -17.3263$$

$$LPort_2 = -13.6633$$

$$LPort_3 = -13.6633$$

$$LPort_4 = -17.3263$$

$$LPort_5 = -13.6633$$

$$LPort_6 = -9.998$$

$$LPort_7 = -9.998$$

$$LPort_8 = -13.6633$$

$$LPort_9 = -13.6633$$

$$LPort_{10} = -9.998$$

$$LPort_{11} = -9.998$$

$$LPort_{12} = -13.6633$$

$$LPort_{13} = -17.3263$$

$$LPort_{14} = -13.6633$$

$$LPort_{15} = -13.6633$$

$$LPort_{16} = -17.3263$$

Appendix G

IE3D Simulation Results
for The
Full 16-Element Array Feed Network

G.1 IE3D Design of the Full Array Feed Network

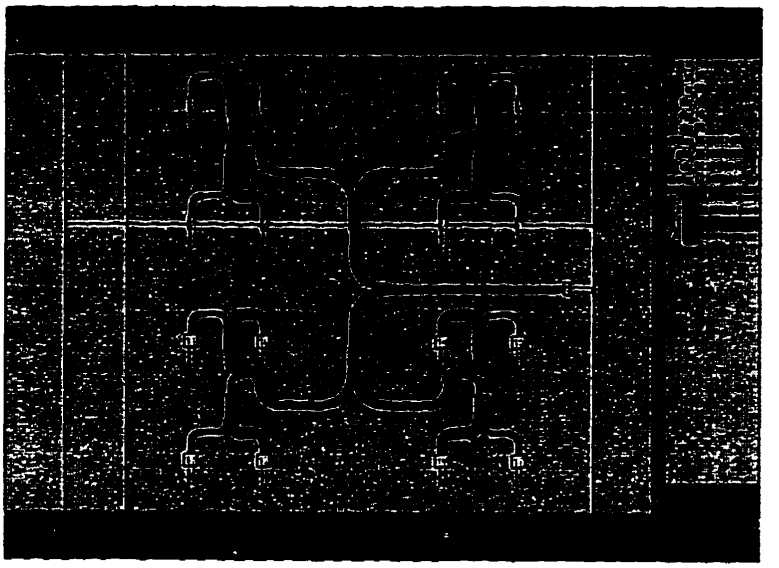

Figure G.1 IE3D simulated full 16-element array feed network

G.2 IE3D Simulation Input Port Results

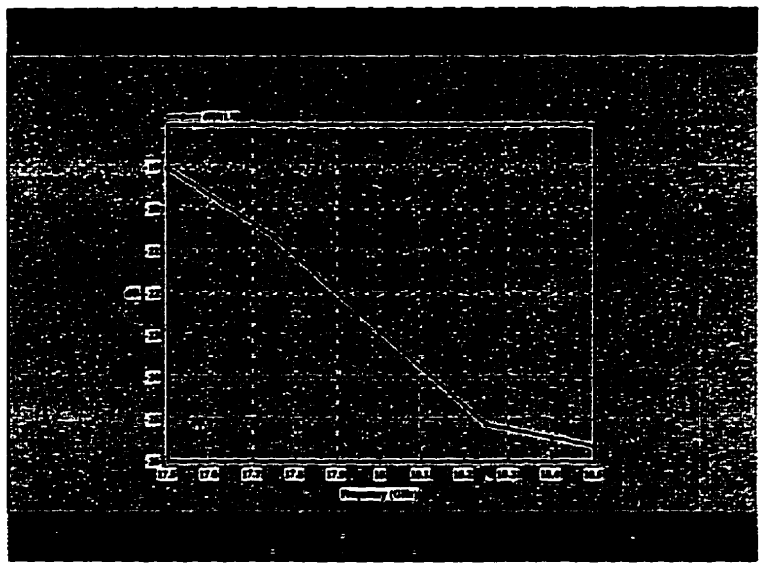

Figure G.2 IE3D simulated array feed network return loss

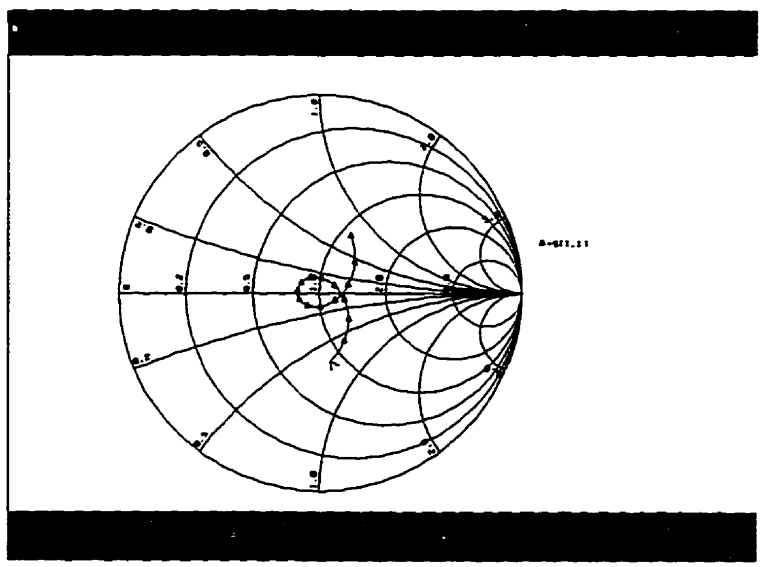

Figure G.3 IE3D simulated array feed network input impedance

G.3 IE3D Simulation Power Levels in Each Feed Network Sub-Array

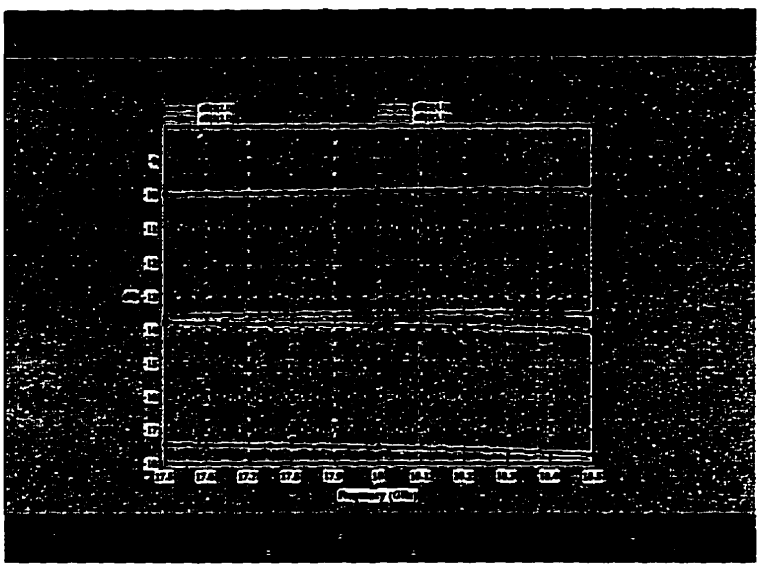

Figure G.4 IE3D simulated array feed network power at ports 2 to 5

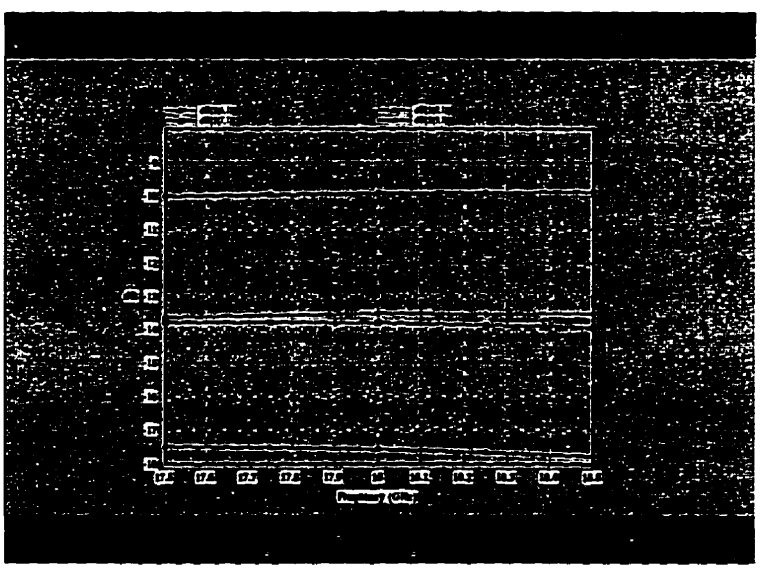

Figure G.5 IE3D simulated array feed network power at ports 6 to 9

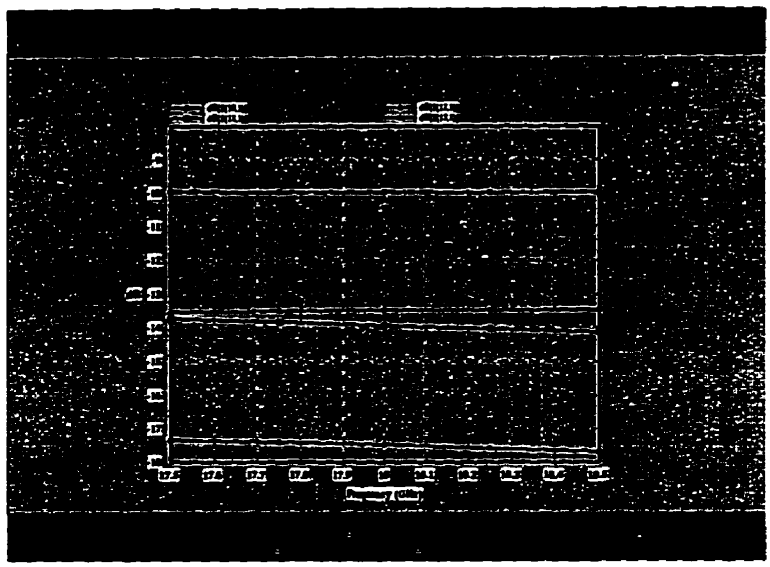

Figure G.6 IE3D simulated array feed network power at ports 10 to 13

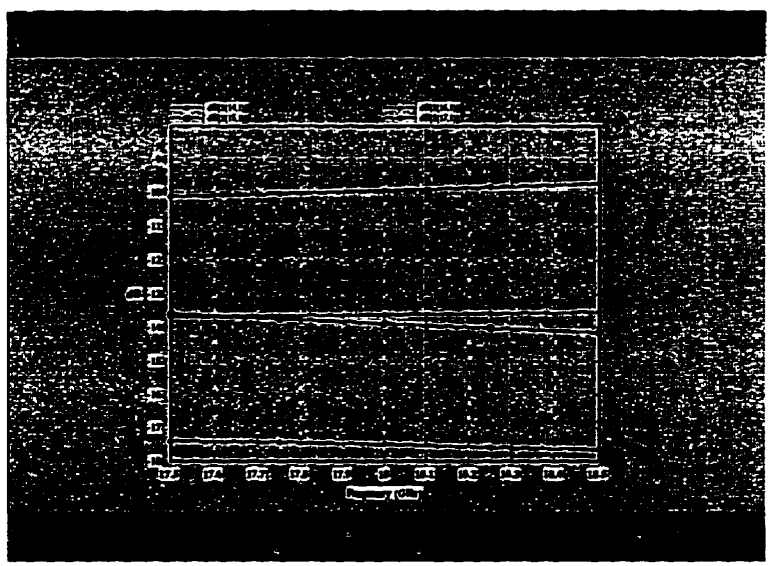

Figure G.7 IE3D simulated array feed network power at ports 14 to 17

G.4 IE3D Simulation Phase Balance in Each Feed Network Sub-Array

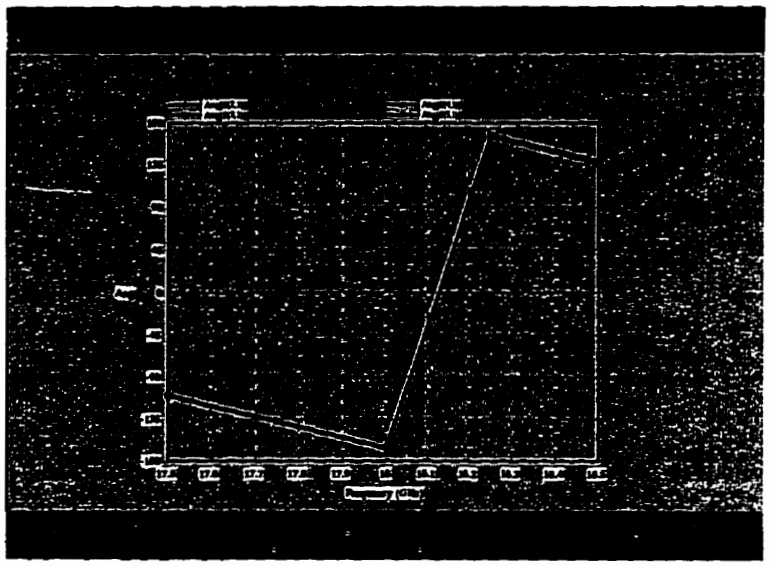

Figure G.8 IE3D simulated array feed network phasings at ports 2 to 5

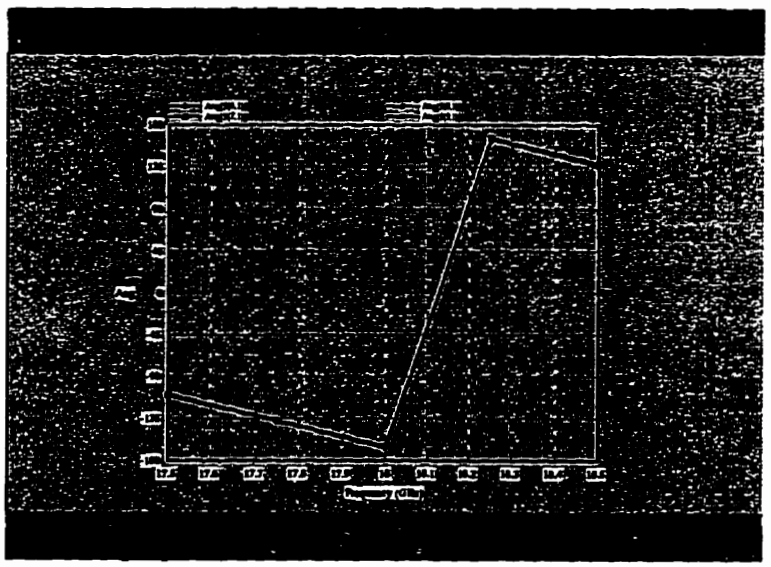

Figure G.9 IE3D simulated array feed network phasings at ports 6 to 9

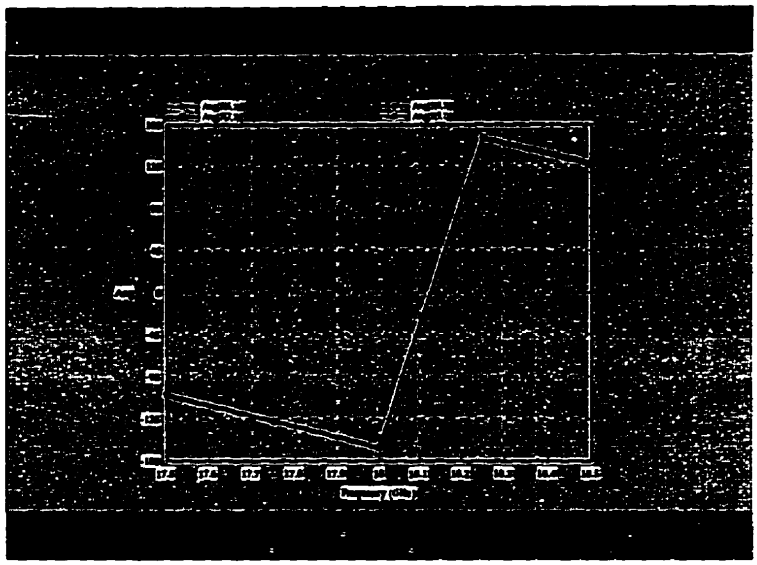

Figure G.10 IE3D simulated array feed network phasings at ports 10 to 13

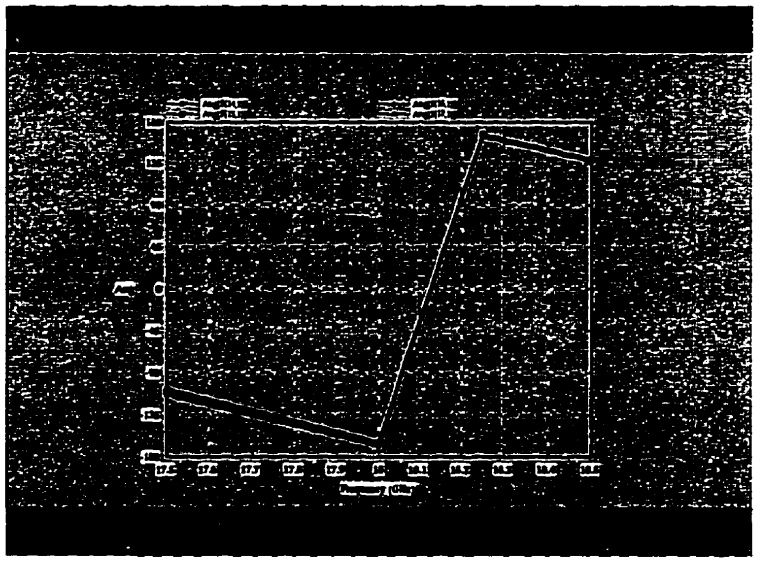

Figure G.11 IE3D simulated array feed network phasings at ports 14 to 17

Appendix H

Antenna Array Dimensions

H.1 Antenna Array Dimensions

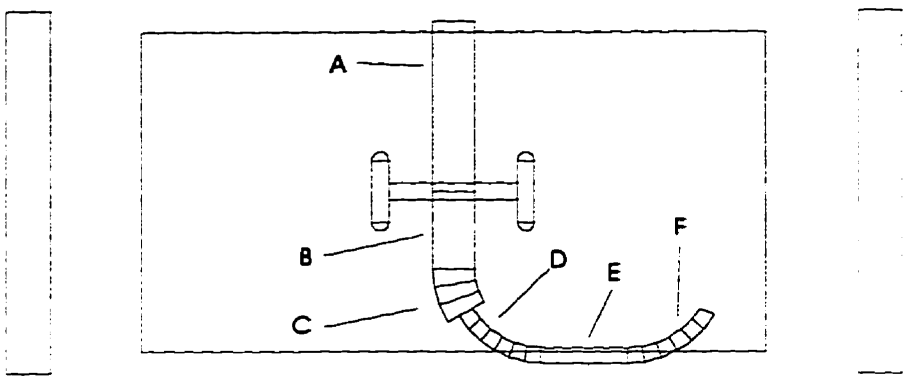

Feedline:	Aperture:	Patches:
A: w=0.47 mm l=1.975 mm	w_{ap}=0.2 mm l_{ap}=1.85 mm h_{ap}=0.925 mm	W_{main}=7.0 mm L_{main}=3.7 mm $W_{parasitic}$=0.5 mm $L_{parasitic}$=4.2 mm Gap=1.04 mm
B: w=0.47 mm l=0.9 mm		
C: w=0.47 mm r=2.0 mm ang=30		
D: w=0.175 mm r=2.0 mm ang=60		
E: w=0.175 mm l=1.0 mm		
F: w=0.175 mm r=2.0 mm ang=60		

Figure H.1 Array element dimensions

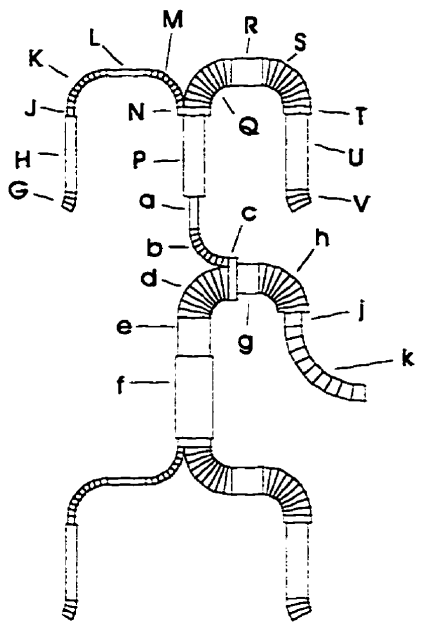

G: w=0.31 mm
r=2.0 mm
ang=30

H: w=0.31 mm
l=2.25 mm

J: w=0.195 mm
l=0.2575 mm

K: w=0.195 mm
r=1.0 mm
ang=90

L: w=0.195 mm
l=1.1027 mm

M: w=0.195 mm
r=1.0 mm
ang=90

N: w=0.99 mm
l=0.25 mm

P: w=0.632 mm
l=2.4 mm

Q: w=0.795 mm
r=1.0 mm
ang=90

R: w=0.795 mm
l=0.9028 mm

S: w=0.795 mm
r=1.0 mm
ang=90

T: w=0.795 mm
l=0.2236 mm

U: w=0.62 mm
l=2.25 mm

V: w=0.62 mm
r=2.0 mm
ang=30

a: w=0.263 mm
l=0.9445 mm

b: w=0.263 mm
r=1.0 mm
ang=90

c: w=1.237 mm
l=0.25 mm

d: w=0.974 mm
r=1.0 mm
ang=90

e: w=0.974 mm
l=1.137 mm

f: w=1.12 mm
l=2.4 mm

g: w=0.88 mm
l=0.63 mm

h: w=0.88 mm
r=1.0 mm
ang=90

j: w=0.47 mm
l=0.405 mm

k: w=0.47 mm
r=2.0 mm
ang=90

Figure H.2 Dimensions of 4-element subarray feed network

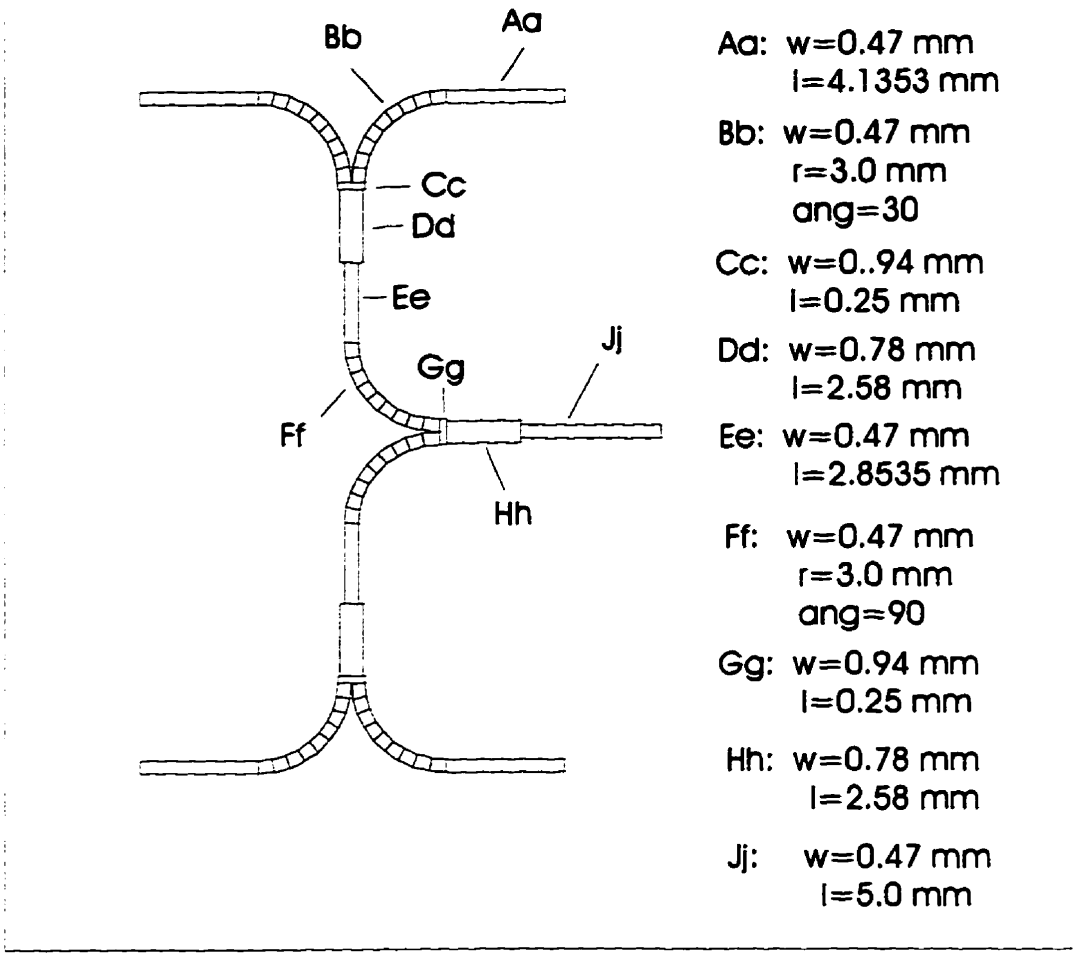

Figure H.3 Feed network used to form full array from subarrays